UNIVERSITÁ DI PISA
DOTTORATO DI RICERCA IN INGEGNERIA DELL'INFORMAZIONE

NOVEL OPTICAL IMAGING SOLUTIONS FOR THE CHARACTERIZATION OF BIOLOGICAL TISSUES AND THE IMPROVEMENT OF ACTUAL INTRAVASCULAR OPTICAL COHERENCE TOMOGRAPHY SYSTEMS

DOCTORAL THESIS

Author
Francesco di Bartolo

Tutors
Prof. Luigi Landini
Eng. Simona Celi
Prof. Nicola Vanello

Reviewers
Prof. Diana Massai
Prof. Dirk Faber

The Coordinator of the PhD Program
Prof. Fulvio Gini

Pisa, October 2020

XXXIII Cycle

This thesis is dedicated to my family

Ringraziamenti

VORREI ringraziare di cuore i miei tutor (prof. Luigi Landini e Prof. Simona Celi) e il mio team di lavoro di Massa (Emanuele V., Emanuele G., Marco F. e Katia C.) per avermi guidato in questo cammino di tre anni che è stato per me molto formativo. Inoltre vorrei anche ringraziare il mio "tutor fiduciario" Antonio Malacarne per avermi trasmesso una quantità enorme di conoscenza in ambiti scientifici in cui io all'inizio del dottorato ero totalmente inesperto. Poi un ringraziamento speciale va sicuramente ai miei amici di Pisa e non, ormai amici di vita con cui ho condiviso belle e brutte esperienze e che mi hanno sempre dato forza. Un ringraziamento speciale va anche a Luisa, la mia amata donna, che ha sempre creduto in me e mi ha sostenuto e sopportato (e continua a sostenermi e sopportarmi) in questi anni. Ma il ringraziamento più profondo va alla mia famiglia (mio padre, mia madre e mia sorella) senza i quali non sarei sicuramente arrivato a tanto. A loro devo tutto. Infine, un affettuoso pensiero va ai miei nonni e le mie nonne che mi hanno trasmesso tanti preziosi valori e che sarebbero felicissimi e orgogliosi del traguardo che ho raggiunto.

Summary

The main purpose of this thesis is to find novel solutions for the characterization of biological soft tissues by menas of optical imaging methods, with a focus on the imaging of cardiovascular system. This aim has been achieved through *i)* development, validation and first experimentation of a novel setup based on small angle light scattering technique (SALS) for the *in-vitro* characterization of the fibrous microstructure of biological tissues; *ii)* implementation of novel methods for the improvement of the performance of actual intravascular optical coherence tomography (IVOCT) systems in terms of light penetration through the blood and signal acquisition speed. For each single activity a deep study of the state of art of the technology has been carried out.

Regarding the first activity, the development of the SALS system has been preceded by an accurate study of the light propagation in fibrous media through the performance of numerical simulations exploiting statistic Monte Carlo method. Such simulations have been a powerful tool to verify the feasibility of the working process of the conceived experimental setup that, soon after, has been designed, assembled, validated through measurements on 3D-printed fibrous samples, and finally integrated into a biaxial testing machine for the performance of real-time *in-vitro* opto-mechanical tests on healthy and diseased aorta samples (affected of ascendic aortic thoracic aneurysm). Through these tests, the system has been demonstrated to be able to characterize the gross fibre dispersion and orientation of the investigated sample together with its mechanical properties in real-time during biaxial testing.

As regarding to the second activity, it is based on previous works revealing that the use of Orbital Angular Momentum technology applied to optical beams increases the beam penetration capacity in turbid media (e.g. biological fluids/tissues) at a wavelength range of 633 nm. This has been demonstrated by performing transmission measurements. The aim of this activity is to demonstrated such effect at a wavelength range of 1300 nm (typical of IVOCT systems) in human blood. To do so, two experimental setups have been developed (wavelength range of 1300 nm) to perform both transmission and reflection tests on fluid biological-mimicking samples and blood respectively. It has been demonstrated that the use of OAM technology could allow a deeper pene-

tration, also at a wavelength range of 1300 nm, in turbid media and human blood, than the use of gaussian beams (conventionally used in IVOCT commercial systems) Hence, the adoption of OAM in IVOCT systems could give the possibility of unprecedented diagnosis of cardiovascular diseases. Last but not least, a specific axial scan system based on the real-time optical spectrum Fourier transformation for IVOCT application (working wavelength range of 1300 nm) has been developed and optimized. First, the system has been experimentally assembled and tested in three different parameter configurations in order to test its performance primarily in terms of acquisition speed and then also in terms of depth range. Since signal distortions have been found to affect the resolution of the systems using some parameter configurations, the system has been simulated and characterized on VPIPhotonics (a dedicated software for electrical and optical circuit design and characterization). Then, a calibration of the system's components has been performed and the optimal parameters of each electrical and optical circuit component have been retrieved in order to find a good compromise between spatial resolution, high frame rate, depth range. Through this work, it has been finally demonstrated that this novel system applied to IVOCT could be able to increase the signal acquisition speed of the axial scan system up to 1 MHz (the typical acquisition speed of commercial systems is maximum 100 kHz).
These research activities have been carried out at BioCardioLab (BCL) of Heart Hospital (Massa - MC) with the collaboration of TeCip (Institute of Communication, Information and Perception Technologies) of Sant'Anna School of advanced studies (SSSUP), in the context of the DIVINE (*High speed 3D imaging of blood vessels based on optical signal processing*) project (funded project of SSSUP and FTGM - Fondazione Toscana Gabriele Monasterio).

Sommario

Lo scopo principale di questo lavoro di tesi è di trovare soluzioni inedite ed efficaci per la caratterizzazione di tessuti biologici soffici attraverso metodi ottici di imaging, con particolare attenzione all'imaging del sistema cardiovascolare. Questo scopo è stato raggiungo attraverso *i)* sviluppo, validazione e prima sperimentazione di un nuovo setup ottico basato sulla tecnica di *Small Angle Light Scattering* (SALS) per la caratterizzazione *in-vitro* della microstruttura fibrosa di tessuti biologici; *ii)* implementazione di metodi emergenti per il miglioramento delle performance degli attuali sistemi di tomografia a coerenza ottica per applicazioni intravasculari (IVOCT) in termini di penetrazione del fascio ottico attraverso il sangue e velocità di acquisizione dei segnali. Per ogni attività un primo attento studio dello stato dell'arte è stato effettuato.

Per quanto riguarda la prima attività, lo sviluppo del sistema SALS è stato preceduto da un accurato studio della propagazione della luce in mezzi fibrosi attraverso l'implementazione di simulazioni numeriche basate sul metodo statistico Monte Carlo. Queste simulazioni sono state uno strumento potente per verificare la fattibilità del funzionamento del setup sperimentale ideato che, subito dopo, è stato progettato, assemblato, validato attraverso delle misure su campioni fibrosi stampati in 3D, e, infine, integrato in una macchina biassiale per l'esecuzione di test ottico-meccanici in real-time *in-vitro* su campioni di aorta sani e malati (affetti da aneurisma toracico aortico ascendente). Attraverso questi test, è stato dimostrato che il sistema è in grado di caratterizzare la dispersione e l'orientamento spaziale delle fibre interne al campione sotto esame, insieme alle sue proprietà meccaniche, in real-time durante test biassiali.

Per quanto riguarda la seconda attività svolta, è basata su un precedente lavoro in cui viene dimostrato che sfruttando la tecnologia dei cosiddetti momenti orbitali angolari (OAM), un fascio di luce alla lunghezza d'onda di 633 nm riesce a penetrare più in profondità in un mezzo torbido. In particolare, è stato sviluppato un setup sperimentale per dimostrare questo fenomeno alla lunghezza d'onda di 1300 nm (tipica dei sistemi IVOCT) effettuando misure sia in trasmissione che in riflessione, rispettivamente su sospensioni di particelle atte a simulare fluidi biologici e su campioni di sangue umano. E' stato dimostrato che l'uso della tecnologia OAM permette una più profonda

penetrazione attraverso il sangue rispetto all'uso di fasci ottici gaussiani (convenzionalmente adottati nei sistemi commerciali IVOCT), con la possibilità di migliorare la dignosi delle malattie cardiovascolari. Ultimo, ma non per questo meno importante, uno specifico sistema di scan assiale basato sulla cosiddetta *real-time optical spectrum Fourier transformation* è stato sviluppato. Per prima cosa, il sistema è stato sviluppato sperimentalmente e testato in diverse configurazione di parametri sia in termini di velocità di acquisizione , che in termini di profondità di acquisizione del segnale. Dato che, in alcune configurazioni sono state riscontrate delle distorsioni nel segnale di uscita responsabili del degradamento della risoluzione del sistema, il circuito è stato simulato in VPIPhotonics (un software per la progettazione e caratterizzazione di circuiti elettrici ed ottici). Poi, è stata effettuata una calibrazione dei vari componenti ottici ed elettrici del circuito e i parametri ottimi relativi a ogni componente sono stati trovati al fine di far funzionare correttamente il sistema ed eliminare, quindi, eventuali distorsioni nei segnali di uscita che potessero degradare la risoluzione, mantenendo nello stesso tempo una elevata velocità di acquisizione e un'accettabile range spaziale. Attraverso questa attività, è stato infine dimostrato che questo nuovo circuito può essere in grado di aumentare drasticamente la velocità di acquisizione dei sistemi di scansione assiale IVOCT fino a 1 MHz (la velocità di acquisizione tipica dei sistemi attualmente in commercio è 100 kHz).
Queste attività di ricerca sono state effettuate presso il BioCardioLab (BCL) dell'Ospedale del Cuore di Massa (MC) con la collaborazione dell'istituto TeCip (Istituto delle tecnologie di comunicazione, informazione e percezione) della Scuola Superiore Sant'Anna di Pisa (SSSUP), nel contesto del progetto DIVINE (*High speed 3D imaging of blood vessels based on optical signal processing*) finanziato dalla Scuola Superiore Sant'Anna e dalla Fondazione Toscana Gabriele Monasterio.

List of publications

International Journals

1. di Bartolo, F., Malik, M. N., Scaffardi, M., Bogoni, A., Celi, S., Ghelfi, P., and Malacarne, A. (2020, June). Penetration capability of near infrared Laguerre-Gaussian vortex beams through highly scattering media. *Optics Letters*. (Vol. 45, pp. 11).

2. Vignali, E., di Bartolo, F., Gasparotti, E., Malacarne, A., Concistrè, G., Chiaramonti, F., Murzi, M., Positano, V., Landini, L., and Celi (2020, December). Correlation between micro and macrostructural biaxial behavior of aTAA: a novel experimental technique. *Medical Engineering and Physics*. (Vol. 86, pp 78–85).

International Conferences/Workshops with Peer Review

1. di Bartolo, F., Vignali, E., Malacarne, A., Gasparotti, E., Positano, V., Landini, L., and Celi, S. (2019, July). Optomechanical characterization of soft biological tissues: an integration of biaxial test and SALS technique. *20th Congress of the European Society of Biomechanics*.

2. Vignali, E., Poli, F., di Bartolo, F., Gasparotti, E., Malacarne, A., Positano, V., Landini, L., and Celi, S. (2019, September). Biaxial and optomechanical characterization of soft tissues: a novel setup and experimental tests. *ESB-ITA Meeting 2019*.

3. F., di Bartolo, F., Malik, M. N., Scaffardi, M., Bogoni, A., Celi, S., and Malacarne, A. (2020, May). Penetration capability of near infrared Laguerre-Gaussian vortex beams through highly scattering media. *CLEO*.

Others

1. Vignali, E., Martini, N., Losi, P., Capellini, K., Della Latta, D., di Bartolo, F., Landini, L., Positano, V., and Celi, S. (2018, June). Towards non-invasive assessment of human aortic tissue microstructure: Diffusion Tensor Imaging for collagen fibre detection. *6th National Congress of Bioengineering*.

2. Cafarelli, A., Chanel L. A., F., di Bartolo, F., Locteau, H., Tognarelli, S., Dumont, E., and Menciassi, A. (2018, July). Ultrasound Acoustic Radiation Force Impulse Imaging for High Intensity Focused Ultrasound Focal Spot Localization. *40th Annual International Conference of the IEEE Engineering in Medicine and Biology Society*.

Contents

CHAPTER 1

Introduction

Medical imaging is the set of all the techniques and processes of creating visual representation of not only the interior of a body for clinical analysis and medical intervention, but also the morphology and the function of organs and tissues for their characterization. Since the second half of the last century, the field of medical imaging has been growing up in both clinical and research fields with the final purpose of improving the quality of life of people through more accurate and advanced diagnosis of diseases. In the last years, medical imaging has been having a big impact in surgery as well. Indeed, the development of dedicated catheter-based imaging modalities for the *in-vivo* visualization of organs and tissues in real-time is becoming critical in the field of robotic surgery and surgical interventions involving internal organs [1–3]. Last but not least, the development of imaging techniques for the *in-vitro* characterization of both healthy and diseased biological tissues is becoming very important for a better understanding of the internal structure of healthy and diseased tissues. The main purpose, in this research field, is to better characterize the development of various pathologies and their progression, investigating how they can affect the surrounding tissue structures in early and advanced stages. The final aim is to find the main features that could bring to advanced and early diagnosis through *in-vivo* imaging investigations.
With the development of catheter-based modalities, *in-vivo* imaging of the cardiovascular system is becoming crucial for both the diagnosis of various cardiovascular pathologies and the real-time guidance in cardiosurgical interventions. In particular, in the last decades, interventional cardiology has been becoming an effective alternative to invasive surgery for numerous congenital and acquired diseases, giving a big importance to the development of powerful imaging modalities able to provide solutions not only for diagnosis, but also prognosis, risk stratification and anatomical and functional assessments [4]. In this scenario, the *in-vitro* characterization of soft tissue structures (e.g.

aorta wall, cardiac valves) in both healthy and diseased state through various imaging technologies is acquiring an important role in clinical research and applications. Indeed, studying the connection between the disease stages and the corresponding morphological changes in the surrounding tissue structures could allow an improvement of disease diagnosis and so, the possibility of early interventions and treatments.
To give some examples, an important research field is based on the atherosclerotic plaque characterization. Atherosclerotic plaques are basically arterial occlusions characterized by a core of extracellular lipid covered by a fibrous collagen cap. They can cause local stenosis and the rupture of the fibrous core can arouse the formation of a thrombus which can result in acute coronary syndromes and myocardial infarction. Therefore, it is important to distinguish vulnerable atherosclerotic plaques and predict which one may rupture. This can be done with the help of advanced imaging techniques. To date, imaging modalities capable of characterizing the structure of atherosclerotic lesions are under development and deploy in order to better understand the natural pathological history and finally detect the lesions with higher risk of rupture in a more accurate way. This can be possible by involving different imaging modalities, each one able to detect at least one of the three principle determinants of plaque's vulnerability to rupture: thickness of the plaque's fibrous cap, size and composition of the plaque's lipid core and eventual local inflammations [5]. Another important research field is the characterization of aneurysm. Aneurysm is a cardiovascular pathology consisting in the abnormal dilatation of a blood vessel. It can affect the abdominal aorta (i.e. Abdominal Aorta Aneurysm-AAA), the ascending thoracic aorta (i.e. ascending Thoracic Aorta Aneurysm-aTAA) or the arteries that supply the brain (i.e. cerebral aneurysm). Aneurysms can be the complication of other cardiovascular pathologies and need to be extirpate before the occurring of coronary rupture and dissection for saving the life of the affected patients [6]. To do so, the characterization of aneurysm for early diagnosis is of crucial matter and several imaging modalities are currently involved in this clinical research scenario. In particular, since several studies revealed that the progression of aneurysm involving the enlargement of the artery lumen affects the artery wall by changing its structure, and consequently its mechanical properties [7, 8], many imaging techniques able to accurately investigate the artery morphology and tissue microstructure are being exploiting [9, 10].
Most of the imaging techniques for the *in-vivo* visualization of the cardiovascular system are invasive because are catheter-based. One of the first catheter-based real-time imaging techniques in cardiovascular field was developed by Bom et al. in 1971. While a system for enabling transducer placement within coronary arteries was developed by Yock et al. in 1988. These first systems are based on Ultrasound. This is why intravascular ultrasound imaging (IVUS) has been the pioneer technology in intravascular catheter-based imaging modalities and since then, it has been developed ever more. To date, IVUS devices are capable of imaging the interior of artery with a spatial resolution of 100 μm. In the last years, novel catheter-based imaging modalities based on other physical principles rather than ultrasounds have been spreading out in both clinical field, for *in-vivo* imaging, and research field, for *in-vitro* characterization of tissues [11].
For instance, intravascular magnetic resonance imaging (intravascular MRI) has been recently developed for artery lumen and wall visualization [12], and atherosclerotic

plaque characterization [13, 14]. However, it is currently limited to the visualization of large or superficial arteries. This is because as the distance of the external coil from the artery increases the resolution progressively reduces due to a significant fall-off of the signal to noise ratio [13]. Moreover, its long acquisition time represents a big limitation for *in-vivo* patient evaluation [15]. Intravascular MRI has a resolution which ranges from 300 to 160 μm which is still worse than the one of IVUS technique [11, 13, 15]. Cardiac computed tomography (CT) is another technology which is rapidly emerging in cardiovascular imaging with the technological advances in multi-slice CT making possible the imaging of vessels and bypass grafts non-invasively. The only big issue remains the signal artifacts due to heart motion [16,17]. Multi-slice CT is capable of detecting heart function with an higher accuracy compared to MRI [18, 19]. On the other hand, many novel imaging techniques based on optical sources are spreading out for clinical diagnosis and some of them are being revolutionary and competitive for both *in-vivo* and *in-vitro* visualization of cardiovascular tissues for their accuracy. Indeed, intravascular optical coherence tomography (IVOCT) is currently emerging as one of the leading techniques for the diagnosis of coronary diseases, such as atherosclerotic plaques, for its spatial resolution (i.e. 10 μm) which is ten times higher in comparison of IVUS [5, 15, 20]. Several optical imaging techniques are also emerging for *in-vitro* characterization of tissue structure for their wide range of scales, resolutions and sources of contrast, making them versatile for many applications [21].
This work focuses on optical techniques for the imaging of the cardiovascular system. In particular, the main objectives are the investigation and validation of novel optical technologies in order to better improve IVOCT performance and the development of a novel optical setup for the *in-vitro* investigation of the microstructure of soft cardiovascular tissues in both healthy and diseased states. The thesis is structured according to the different chapters hereafter summarized:

- Chapter 2: within this chapter, a deep analysis of the state of art of the main optical techniques for both *in-vivo* imaging for clinical use and *in-vitro* imaging for the characterization of soft biological tissues is done. Among all the discussed techniques, the ones involved and elaborated within the thesis are presented, i.e. Small Angle Light Scattering (SALS) and OCT.

- Chapter 3: within this chapter, the development of a novel optical system based on SALS imaging technique for the characterization of the fibrous soft tissue structure is presented. In the first paragraphs, physical principles and working process of SALS technique are explained together with the state of art of the technology. Then, an *in-silico* analysis based on Monte Carlo (MC) simulations of the propagation of light in fibrous media is presented. The aim of these simulations is a better understand of the physical phenomena laying behind SALS and the feasibility of the conceived optical system. The *in-silico* analysis part is followed by the second part of the chapter consisting in the development of the SALS system. Here, all the system components are explained in detail and the first validation test on 3D-printed fibrous samples is presented. The results from the validation tests are then shown and compared with the corresponding *in-silico* simulations. Finally, the first *in-vitro* tests on ex-vivo soft tissue samples are reported and discussed.

- Chapter 4: within this chapter, the first ever performance of reflection and transmission tests in mimicking-tissue samples and blood samples with the employ of both conventional Gaussian (G) and Laguerre-Gaussian (LG) beams based on orbital angular momentum (OAM) technology in the near-infrared region (i.e. wavelength of 1300 nm) is presented. The main objective is to demonstrate that, with the use of OAM technology, the light transmission through highly scattering media (i.e. blood) increases and so, it could be potentially exploited for the improvement of IVOCT technology in terms of signal penetration depth along the arteries. In the first part of the chapter, the theory behind LG beams and OAM technology is treated and the state of art of the technology is presented together with theoretical basis on light propagation in highly scattering turbid media. Afterwards, the transmission and reflection tests that have been performed are respectively reported from the development of the experimental setup to performance of the measurements, and finally discussed.
- Chapter 5: within this last chapter, the development of a novel setup emulating an IVOCT axial scan (A-scan) based on photonic technologies is presented. The main objective is that the proposed A-scan setup allows the simultaneous data scan and acquisition at unprecedented high speed (i.e. frame rates between 500 kHz and 1 MHz) in the optical domain without post-processing of the system output signal. It is possible by the exploitation of the real-time optical spectrum Fourier transformation (RT-OSFT). This novel technology for IVOCT A-scan allows a rapid imaging of the tissue under investigation and consequently a bigger amount of analysed data in short time intervals and the decreases of image artifacts due to the movement of the investigated tissues. First, the state of art of OCT technology is presented together with a brief explanation of the actual OCT modalities and the theory behind RT-OSFT. Then, the experimental development of the system followed by its calibration and parameter optimization done through a dedicated software (i.e. VPIPhotonics) is presented.

The thesis concludes with a chapter dedicated to a brief recap of the performed activities highlighting their potentials and implications in both clinical and research fields, and discussing about further related future works.

CHAPTER 2

State of the art of optical techniques for the imaging of the cardiovascular system

2.1 State of the art of traditional techniques largely adopted in clinical scenarios

Biomedical imaging techniques based on optical sources are being revolutionary in clinical fields and are expected to have an unprecedented impact on prevention and diagnosis of diseases. The main advantages of adopting optical solutions in medical imaging are the following ones [22]:

- capability of giving both functional and structural information of tissue changes with high spatial resolution and sensitivity;
- use of non-ionizing energy sources;
- employment of portable and low-cost equipment;
- capability of working in real-time;
- adaptability to microscopes and endoscopes for the acquisition of macroscopic and microscopic information which make optical imaging devices versatile to almost all biomedical fields;
- capability of providing quantitative information.

All the above mentioned factors make optical imaging techniques potential means for the improvement of cardiovascular diseases diagnosis through *in-vivo* intravascular imaging. So far, numerous catheter-based techniques based on optical sources have been investigated and developed for intravascular imaging. Each technique possesses

its own advantages and limitations.
Up to date, one of the technologies which has been mostly used in intravascular imaging together with IVUS, is angioscopy. It allows the visualization of the surface colour and superficial morphology of artery wall with the capability of identifying eventual anomalies. Most of the angioscopic techniques are based on a light source which emits white light (i.e. spectral window ranging from 400 nm to 780 nm) at high intensity to illuminate the target objects through a fibre-optic catheter. Sometimes near-infrared (NIR) optical sources are used, for example in modalities based on fluorescence (e.g. NIR fluorescence angioscopy). The imaging catheter is flexible and contains a fibre bundle with thousands of pixels. Then, a micro-CCD camera allows the construction of coloured images of the investigated artery lumen [11]. For instance, the latest generation catheter currently in clinical use for angioscopy is characterized by a bundle of 6000 fibres, an outer diameter of 0.75 mm and a microlens with focused depth ranging from 1 to 5 mm and providing a 70 degrees field of view [20].
From coloured angioscopic images, normal artery are glistening white. Changes or blurs of this colour mean the presence of anomalies. Recent studies have proved that intracoronary angioscopy is an accurate means for not only *in-vivo* localization of atherosclerotic plaques, but also characterization of plaque vulnerability and eventual presence of thrombus or endoluminal irregularities such as fissures, tears and ulcerations. This is possible thanks to its high spatial resolution (i.e. 10 to 50 μm) images acquired through fibre optics [11, 15, 23]. For instance, clinical studies revealed that a thrombus can appear as a white granular material if it is platelet-rich, while as a protruding red irregular structure if it is fibrin/erythrocyte-rich [24]. Furthermore, the more vulnerable atherosclerotic plaques appear yellow and the increased of the yellow intensity has been demonstrated to be connected to an increase of likelihood of subsequent coronary events (i.e. plaque rupture, thrombosis) [25–27]. Some clinical investigations reported the successful use of angioscopy also for the macroscopic evaluation of both neointimal coverage and local thrombus formation over stent struts [28–30]. Last but not least, the fluorescence principle has been successfully applied in angioscopy (i.e. NIR fluorescence angioscopy) for the guidance of surgical re-vascularization therapies by exploiting the optical properties of a cyanine dye with absorbance and fluorescence peak in the NIR region at about 800 nm (i.e. indocyanine green). The working principle of NIR fluorescence angioscopy consists of i) the intravascular injection of cyanine dye in the area under investigation, ii) the subsequent fluorescent excitation through an infrared laser source, and iii) the acquisition of the indocyanine fluoresced light. This process allows the real-time data acquisition and visualization of the investigated vasculature [11]. Although this particular technique has been demonstrated to be effective in bypass implantation procedures, a recent clinical study confirmed that farther investigations are needed to improve the accuracy in visualizing eventual graft problems in patients who underwent bypass implantation [31].
To date, intracoronary angioscopy has been demonstrated to be crucial for gaining insights into the pathophysiology of coronary lesions. Indeed, it is a clinical well-established diagnostic technology for *in-vivo* intravascular imaging because of its high sensitivity to detect thrombus and evaluate plaque pathological state. However, the subjectivity of colour image interpretation has been largely criticized because it does not give quantitative information and only relies on the doctor's experience. Therefore,

techniques based on colorimetry able to provide quantitative information are under investigation in order to better improve their accuracy and reliability [32]. Moreover, the ability of visualizing only the luminal surface could not be sufficiently sensitive. Indeed, the limited spatial resolution does not allow the visualization of the artery wall microstructure which could be determinant for a better understanding and diagnosis of early pathological states. This last limitation has been even confirmed by a study performing a comparison with IVUS imaging which is the competitive *in-vivo* intravascular modality widely used in clinical scenarios for cardiovascular disease diagnosis together with angioscopy [20, 33]. But, the biggest limitation which is typical of angioscopy and generally interests every intravascular catheter-based imaging modality for *in-vivo* diagnosis employing optical sources, is the need to create a blood-free field in the proximity of the region under investigation to assure the proper operation of the device. In fact, the presence of blood would obscure the acquired images because of its high absorption. The generation of a localized blood-free field in a vessel is currently achieved in two ways: i) by temporarily applying a proximal occluding balloon during the acquisition time or ii) the use of a smaller catheter to continually flush saline in front of the imaging probe to transiently displace blood. The first modality, if not well-managed, could create serious complications such as coronary rupture, thrombosis, dissection, or arrhythmia. The second modality is safer, but requires removal of the guidewire before the acquisition of each angioscopic image [20]. Since this procedure concerning the blood displacement in proximity of the catheter tip is necessary to perform intravascular imaging through optical devices, it is a big issue which cannot be completely solved. But at least, the probability of devastating complication arise which could be caused by this procedure (i.e. coronary rupture, thrombosis, dissection, arrhythmia), can be considerably decreased by faster image acquisition speed and, thus, smaller acquisition time. An optical technique which has been recently developed and can overcome the issue of complication arise following blood displacement is intravascular OCT (IVOCT) thanks to its acquisition system which allows faster image acquisition compared to other technologies largely adopted in clinical scenarios (i.e. IVUS, angiography) [34].

IVOCT can be thought as the optics-based counterpart of IVUS. Indeed, it is an optical imaging technique which is based on the measurement of reflected echoes coming from the investigated tissues. The difference is the nature of these echoes, i.e. light waves for IVOCT, while acoustic waves for IVUS. The acquired backscattered light is characterized by the optical echoes of the infrared light sent into the tissue through a dedicated optical source and coming back to the photodetector. Therefore, the working principles is analogous to the IVUS one, with the main difference consisting of the different signal nature. IVOCT systems are characterized by a superluminescent diode as optical source of low coherent infrared light (i.e. wavelength of 1300 nm) and employ interferometric techniques (i.e. Michelson interferometer) to determine the depth of the reflector which is the target tissue (i.e. A-scan). The IVOCT catheter can rotate in order to provide cross-sectional images of the vessel's lumen (i.e. B-scan). The catheter rotation is guaranteed by a stationary outer sheath and a rotating mirror in the inner core. This design facilitates a pull-back of the imaging core [11, 20, 35]. Thanks to its high resolution which ranges from 2 to 10 μm, OCT has been demonstrated to be a very promising technique for an accurate visualization and superior characterization

of artery wall anomalies (i.e. atherosclerotic plaques) compared to the other intravascular imaging techniques largely diffuse in clinical use (i.e. IVUS and angioscopy). Indeed, some *ex-vivo* studies have demonstrated that IVOCT technique is capable of classifying atherosclerotic plaques more accurately [36–38], with high sensitivity and specificity respectively of 92% and 94% for lipid-rich plaques, 95% and 100% for fibrocalcific plaques, and 87% and 90% for fibrous plaques [39]. In clinical scenarios, the safety and feasibility of IVOCT image wire systems has been demonstrated in patient affected by acute coronary syndromes as well as myocardial infarction [40]. Indeed, it has been able to successfully characterize culprit lesion morphology through *in-vivo* investigations and assess restenosis after stenting [41, 42]. Furthermore, new imaging modalities integrated to IVOCT imaging systems such as polarization imaging, spectroscopy, Doppler imaging and elastography, could be able to provide more detailed information not only about the macrostructure and composition of artery wall anomalies (e.g. atherosclerotic plaques) but also about the biochemical and biomechanical properties of the plaque core and the near-surrounding tissue [43, 44].

2.1.1 Intravascular optical coherence tomography and its ultrasound counterpart

Although IVOCT is a relatively novel imaging modality, it has been quickly spread out in clinical intravascular imaging scenarios at expenses of its acoustic-based counterpart (i.e. IVUS) thanks to its superior performance. As it can be seen from Table 2.1 [34],

Table 2.1: *Comparison between physical and technical characteristics of IVOCT and IVUS*

	IVOCT	IVUS
Energy source	Near-infrared light	Ultrasound
Wavelength (micrometer)	1.3	35-80
Axial resolution (micrometer)	from 15-20 to <1	100-200
Lateral resolution (micrometer)	from 20-40 to <2	200-300
Frame rate (frames/s)	from 15-20 to >100	30
Pull-back rate (mm/s)	from 1-3 to >20	0.5-1
Max. scan diameter (mm)	7	15
Tissue penetration (mm)	1-2.5	10

traditional IVOCT systems offer a spatial resolution which is much higher compared to that of IVUS systems. This characteristic is very critical and makes IVOCT a powerful mean for more accurate and reliable diagnosis of intravascular diseases. As described in Table 2.1, the spatial resolution, the frame rate and the pull-back rate lies respectively within large ranges of values. Indeed, depending on the applied modality these parameters can be drastically improved. The first OCT systems were based on the Time-Domain technique which is characterized by axial and lateral resolution values of 15-20 μm and 20-40 μm and frame-rate and pull-back values of 15-20 frames/s and 1-3 mm/s. With the advent of the OCT systems based on the Fourier-Domain technique the frame-rate and pull-back parameters have been improved to values >100

frames/s and >20 mm/s respectively. This is the main reason why, nowadays, all the commercial OCT systems used in intravascular imaging are based on Fourier-Domain technique. This spectral OCT modality enables the fast 3D imaging of long coronary tracts, with just a brief saline purge. Therefore, in this way, the necessity of using occluding balloons can be overcome and the danger of the consequently arise of acute coronary problems can be highly limited [45]. Additionally, a novelty system which has been developed thanks to the use of newer laser and an extended focus depth by means of an axicon-type optical element, is μOCT. It can achieve very high axial and lateral resolutions (i.e. <1 μm and <2 μm respectively) resulting a powerful modality for the imaging of cellular and subcellular structures, and for the study of inflammatory processes at subcellular levels [46, 47]. However, a considerable limitation of OCT compared with IVUS is its poor penetration depth caused by the high scattering that light experiences penetrating biological tissues, in particular blood. This can bring to shadowing effects which can obscure deeper tissue regions and decrease contrast due to light attenuation [21].
In summary, each modality possesses unique advantages that can compensate limitations of other techniques. For instance, a potential synergism exists between IVOCT and IVUS as their advantages are complementary. Indeed, the former one provides higher resolution, while the latter one higher penetration depth. This is also the case of specific modalities which can be adopted in both IVOCT and IVUS. Namely, spectroscopy can give biochemical information, while elastography biomechanical information. To date, the optimal imaging modality for *in-vivo* intravascular imaging remains undefined.

2.2 State of the art of emerging techniques for soft tissue structure characterization

It is well established that the structure of soft tissues plays a crucial role in tissue functions and behaviour in both healthy and diseased state. The development of accurate techniques allowing biological tissue structure investigation is therefore necessary to improve the observation and quantitative analysis of the physiological state and functional behaviour of tissues for the development of more complete computational models and a significant improvement of diagnostic capabilities. Optical techniques are ideal for the analysis of tissue structure because they are versatile for several applications thanks to their wide range of scales and resolutions. Furthermore, they are able to make quantitative measurements by offering degrees of freedom beyond spatial variation, allowing a quantitative characterization of various metrics (e.g. molecular composition, fibre alignment and mechanical properties) through polarization-, wavelength- and time-dependent measurements [21]. Hereafter, a discussion on various optical techniques for the characterization of tissue structure is presented based on the specific types of investigation.

2.2.1 Imaging for investigations of bulk constituent tissue structure

The most widespread optical imaging technique for *in-vitro* investigation of soft tissue structure, which is considered one of the traditional standard together with other non-optical techniques (i.e. MRI, CT and ultrasound imaging), is histology. It has been

adopted for years and, to date, is largely used in the laboratories as a powerful tool for understanding biological organisms. Histology is based on optical microscopy and exploits a particular technique called bright-field microscopy. The working principle consists in transmitting a light beam by means of a dedicated optical source to the investigated sample, which is typically positioned in a slide, and creating a "shadow" of the image through the contrast provided by the light attenuation through the tissue sample. Since this method relies on the intrinsic absorption experienced by the light beam traversing the sample, it often results in low contrast. Therefore, several methods of contrast enhancement have been developed in order to make this technique more effective. For instance, methods such as phase contrast and differential interference contrast have been investigated and finally demonstrated to be capable of imaging tissue structure more accurately by using different source of contrast [48]. Although bright-field microscopy is able to identify different structures and chemical components within tissues through the exploiting of several contrast mechanisms, the investigated tissue sample needs to be fixed and physically sectioned in very thin slices. This is a big limitation because leads to low scales for use, destruction of the native tissue and inability to perform functional imaging [21].
A solution for the performance of large scale, non-destructive functional imaging is the use of non-optical technique. However, they present much lower resolution and levels of contrasts, and lack of tissue differentiation at microscale. Nowadays, many optical imaging techniques are under development in clinical research field scenarios in order to overcome the above mentioned limitations. Each of these novel techniques are characterized by specific advantages which make them suitable for specific applications.
Some novel optical imaging techniques which are suitable for the investigation of bulk constituent tissue structure and thus most closely mimic traditional histology, are confocal microscopy, non-linear techniques, and OCT. This last technique has already been presented in the previous paragraph, with a focus on intravascular applications, as a technique increasingly adopted in commercial systems for clinical use. But, it is still under investigation and improvement in research scenarios as a potential mean for highly accurate characterization of tissue structure at micrometre and even submicrometre scale with the advent of μOCT. These three optical techniques are characterized by higher resolutions with respect to traditional histology and the main sources of contrast are the interfaces between tissues. Indeed, tissue interfaces are characterized by a mismatch of refractive index which produces an increase of light scattering. The scattered light is then acquired by the optical device and the image of the tissue is built through a dedicated elaboration of the acquired backscattered optical signals. Even if they are mostly used for *in-vitro* investigations, they are quickly emerging also for *in-vivo* imaging in many clinical scenarios.
In particular, confocal microscopy is based on the confocal principle which is a method that allows the acquisition of the reflected light exclusively coming from the focal plane. It is used for a wide range of applications from imaging of dynamic processes in living cells to accurate morphological analyses of tissues to co-localization of protein expression patterns [49–51]. The main benefits of this technique are the high axial resolution which is of the order of 0.5-5 μm, and the capability of using intrinsic contrast coming from both changes in refractive index and absorption within the investigated tissues. Moreover, this technique can be paired with fluorescent-mode imaging, resulting in a

powerful tool for the investigation of both tissue and cell structures [52–55].
The main drawbacks are the small penetration depth, which is typically some hundreds of microns (e.g. 200-300 μm in human skin) and depends on the applied wavelength (i.e. typically infrared and visible regions), and the long acquisition time due to the point scan. Recently, faster scanning based on line scanning, rather than point scanning, have been investigated in order to improve the acquisition time, but at some costs of the image resolution [21, 56, 57].
On the other hand, non-linear microscopy is a set of techniques (i.e. two-photon microscopy, second harmonic generation) which have several advantages over linear reflectance (i.e. confocal microscopy). The most important advantage is the capability of achieving deeper penetration depth into the biological tissues (i.e. up to 1 mm) while maintaining sub-micrometre resolution [58]. Furthermore, such techniques require much less illumination power leading to less photobleaching to the sample and the excitation wavelength is easily distinguished by the emission wavelengths leading to an improvement of contrast [59, 60]. Typical drawbacks of non-linear microscopy are some eventual loss in resolution while working in the near-infrared region due to unexpected light diffraction phenomena occurring inside the tissue, limited imaging depth for the imaging of deep structures (i.e. deeper than 1 mm from the surface) without physical sectioning of sample and long acquisition time for large 3D data collection [61, 62].
Finally, the technique that has been demonstrated to have better capabilities in terms of resolution and contrast with respect to confocal reflectance and non-linear techniques, is OCT. Indeed, as it has already been discussed in the previous paragraph, it allows the imaging of tissue structure with micrometre resolution as well as the imaging of the cellular microstructure with unprecedented sub-micrometre resolution and without the need of sectioning thanks to the development of μOCT.

2.2.2 Imaging for investigations of molecular tissue constituents

Recently, optical techniques have been also employed in the field of molecular imaging. Indeed, novel optical imaging techniques able to investigate the molecular composition of biological tissues have been starting developing by means of spectroscopy which is based on the acquisition of spectral signals directly coming from the investigated tissue. Depending on the optical properties which is measured (i.e. absorption, fluorescence, scattering) several spectroscopic modalities can be distinguished. The employed optical source type varies depending on the physical phenomena to be measured [11, 22]. Within the set of spectroscopic techniques, different imaging modalities have been emerging.
Among them, diffuse reflectance/NIR spectroscopy is a technique which uses a broad spectrum of wavelengths (i.e. from 700 to 2500 nm) as light source and measures the bulk scattering and absorption of different tissue regions. The acquired spectrum has a distinct trend of diffuse reflectance from the tissue across the broad wavelength spectrum, allowing the visualization of the specific absorption and scattering properties of the tissue and thus the identification of the sample constituents [22, 63].
In a similar way, NIR fluorescence spectroscopy uses a laser source to send luminescent emission and identify the properties of the illuminated tissue from the acquired fluorescent spectrum. Basically, luminescent emission consists in photons which excite the

tissue molecules to a higher energy level and the subsequent decay releases part of the energy difference in the form of light. Through the acquired spectrum, the tissue can be accurately characterized and its constituents can be differentiated, similarly to confocal fluorescent microscopy but across a larger and more highly resolved spectrum [21, 64].
Raman scattering spectroscopy is another emerging spectroscopic technique which exploits a narrow-band light source for monitoring the shift in wavelength (i.e. inelastic scattering) occurring when the incident photons interact with the tissue and lose/gain energy. The acquired spectra are weak but a highly reliable identification of tissue constituents can be done because individual molecules induce very specific trends in the Raman scattering spectra [65].
These spectroscopic techniques are very suitable for the investigation of bulk local tissue characteristics. They can achieve a lateral resolution on the order of 100 μm, while the axial resolution results in an average of reflectance and fluorescence across the sample depth. The depth which can be achieved, depends on the probe design [21]. In the cardiovascular field, the adaptation of such techniques to endoscopes for intravascular imaging is nowadays under clinical evaluation for commercial use. For instance, some studies revealed that NIR spectroscopy is a potential modality for the characterization of atherosclerotic plaque composition thanks to an adequate signal-to-noise ratio through the blood. However, the main limitation of NIR spectroscopy is that it does not provide structural plaque information [11, 66–68]
Regarding Raman spectroscopy, several studies regarding the characterization of artery wall and atherosclerotic plaques have been performed. It has been demonstrated that it is possible to retrieve clinically useful information about plaque composition with the manipulation of the acquired spectra through dedicated spectrum modelling algorithms [69, 70]. However, its adaptation to intravascular investigations is technically more challenging than NIR spectroscopy because of the low intensity of the light scattered by the artery wall and blood interference. To date, some studies have been performed in order to overcome these issues [71].
A relatively young spectroscopic imaging technique which is very robust for tissue differentiation in highly heterogeneous regions, is spatial frequency domain imaging (SFDI). This technique includes a wide range of modalities which can employ a single wavelength or a broadband source to structurally illuminate an entire planar field and then reveal quantitative information about the scattering and absorption properties of the investigated sample through proper demodulation techniques applied to the acquired spectra [72–74].

2.2.3 Imaging for investigations of fibrous soft tissue structure

Together with imaging of bulk tissue constituents and molecular composition of tissues, another important set of optical imaging techniques is currently under development in clinical research scenarios with the aim of characterizing the fibre alignment in soft tissue structure. These techniques are often used together with specific biomechanical tissue analysis which include the application of controlled mechanical stresses and strains (i.e. axial/biaxial testing). In this context, the main developed techniques are polarization imaging (PI) and small angle light scattering (SALS). Both techniques exploit visible lights for their investigations.
Regarding PI, it is a technique which exploits the orientation of the electromagnetic

field propagating into the sample. This is possible because soft tissues contain cylindric structures (i.e. fibres) which are birefringent and cause anisotropic scattering. This phenomenon depends on the polarization of the incident light which influences the amount of light that maintains its initial polarization while penetrating into the tissue. The comparison between initial light polarization state and polarization of the amount of light reflected/transmitted from the tissue, leads to a quantification of the structural anisotropy and so, the fibre orientation within the investigated tissue [75, 76]. Even if PI can be used as a stand-alone imaging technique, in many studies it has been incorporated to other imaging modalities such as OCT, spectroscopy or SFDI [77–79].
On the other hand, SALS uses an unpolarized and low-power laser beam as light source. Light traversing the tissue sample is both scattered and transmitted. Typically, the scattered photons outside the sample characterize the SALS pattern which can be either acquired by a photosensor (i.e. CCD camera) or a dedicated projection screen. The spatial distribution of scattered light is an average of all the structured information within the light beam envelope. From the acquired pattern the angular distribution of the constitutive tissue fibres and therefore a quantification of the tissue structure anisotropy can be obtained [80]. The lateral spatial resolution of this technique depends on the raster step if a lateral scanning is applied to the sample, and the diameter of the beam which travels through the depth of the sample. Axial resolution cannot be resolved. Chemical clearing or histological sectioning could be sometimes needed if the sample is not adequately translucent. Therefore, SALS technique fits well when damage to the sample is a nonissue. SALS has been demonstrated to be a powerful tool in *in-vitro* analysis for the development of constitutive tissue models and an effective complement to mechanical testing of soft tissue with the building of their microstructure maps [21].

2.3 Summary

Optical imaging techniques are being successfully adopted in both clinical scenarios for *in-vivo* imaging and research fields for a deep characterization of tissues aimed to give information about their structure at micro- and macro- scale and molecular composition. In particular, in the field of *in-vivo* cardiovascular imaging, angioscopy represents the traditional optical imaging standard together with IVOCT which is younger but, it has been spreading out quickly for its high resolution and slowly substituting its Ultrasound counterpart (i.e. IVUS) in several applications where a micrometer resolution is required. In addition to angiography and IVOCT, several optical techniques are being developing in research scenarios for deeper tissue characterization. Some of them have also been adapting to endoscopes and are currently under clinical evaluation for *in-vivo* intravascular investigations (i.e. NIR and Raman spectroscopy). The most important aspects which need to be taken into account in order to evaluate if a technique is suitable for a certain application, are:

- non-destructiveness: ability not to affect the sample in any way;
- resolution;
- scale: connected to the the quality of the resulting image;
- type of measurement: if it is quantitative or only qualitative;

- the capability of performing functional imaging through fast data acquisition (i.e. video rate).

There still does not exist a technique which excels in all the above listed factors. Each technique has its own advantages and drawbacks, and each one is best suitable for a specific range of applications. In Figure 2.1, an overview of the principal optical tech-

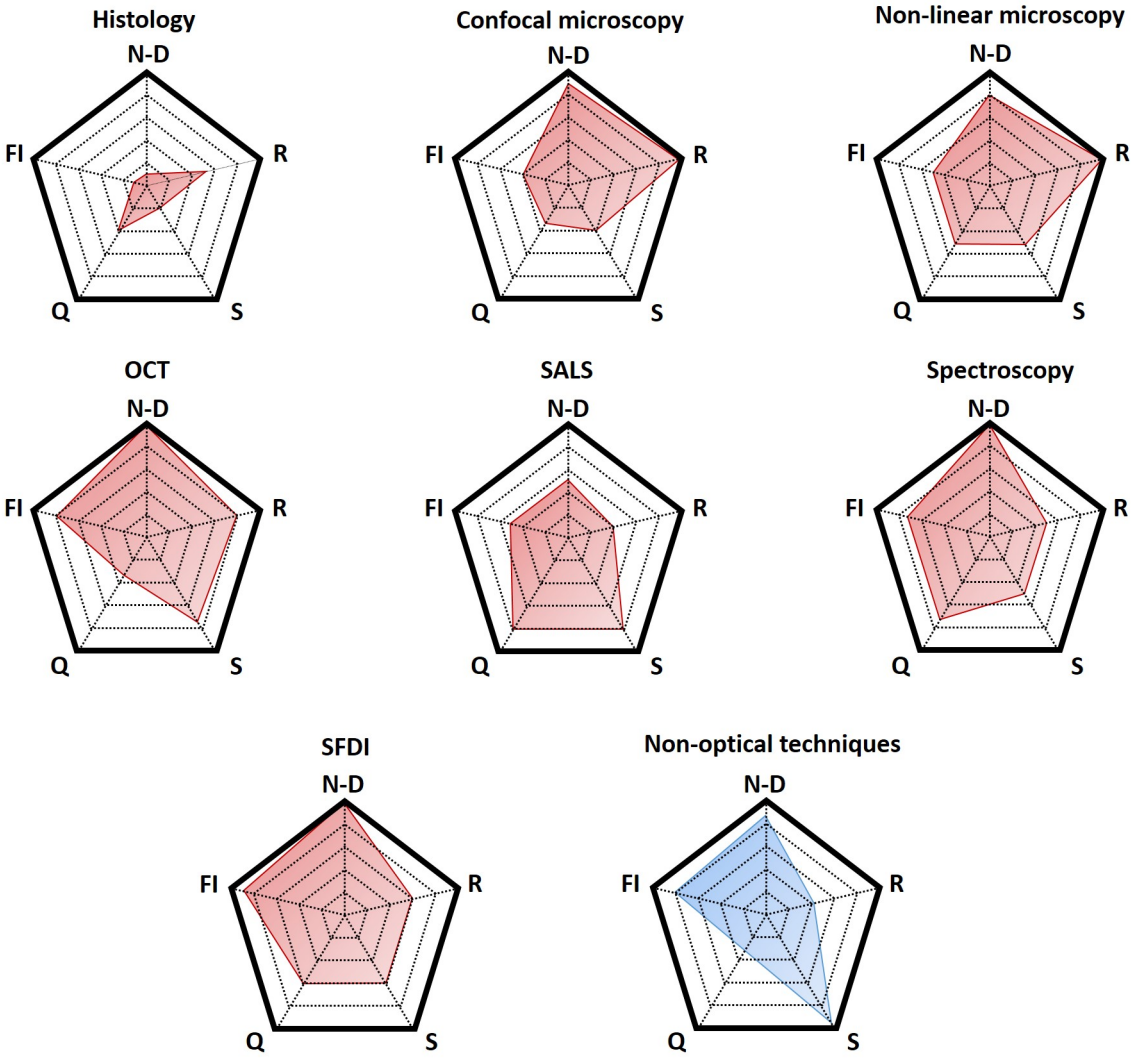

Figure 2.1: *Diagrams showing a comparison among non-optical and most common optical techniques in terms of observing and characterizing biological tissues (**N-D**: non-destructiveness, **R**: resolution, **S**: image scale, **FI**: functional imaging, **Q**: quantitative).*

niques commonly used for tissue characterization based on their performance and compared with non-optical techniques is shown [21]. From an analysis of the diagrams, the set of optical techniques includes much more modalities in comparison to non-optical techniques. This implies a better flexibility of the optical techniques in terms of fields of application. Indeed, for each application, ranging from *in-vivo* imaging to *in-vitro* analysis of tissues, it can be found a corresponding suitable optical technique. For *in-vivo* imaging applications, the most suitable techniques need to be totally non-destructive,

therefore, the most eligible ones are OCT and spectroscopy. The former one, already diffused in clinical use, combines non-destructiveness with high capability of functional imaging and high quality images together with a good adaptation to catheter-based analysis for endoscopic/intravascular applications. The latter one is characterized by lower resolutions and image scale with respect to OCT, but it is more suitable for quantitative analysis. Its applicability to catheter-based application is still under study and development. The integration of SFDI analysis to both OCT and spectroscopy can finally bring to higher acquisition speeds and so higher functional imaging capabilities.
On the other hand, the rest of the techniques shown in the Figure 2.1 are best suitable for tissue structure visualization. As already said, histology is the traditional standard commonly used in laboratories. However, the sample needed to be sectioned for being analyzed, making histology accurate as much as destructive. That is why, in many application where the sample sectioning and damaging is an issue, other more suitable techniques can be used. For example, SALS does not require sample sectioning and provide accurate quantitative analysis and maps and non-linear microscopy is to date considered the most powerful technique in term of resolutions.
Finally, it can be said that each technique has its own characteristics which makes it suitable for certain tissue investigations. Therefore, there is not an optimal technique able to solve all the issues related to the imaging of tissue in the same time. For this reason, recently, it has been proposed to use multi-modal techniques in order to overcome problems related to tissue attenuation which is the main limitation affecting optical techniques, such as the combination of ultrasound with optical signals typically used for the measurements of mechanical properties of tissues (i.e. Photoacoustic tomography, Brillouin microscopy) [21].

CHAPTER 3

Development of a novel optical setup based on small angle light scattering for the characterization of soft biological tissue structure

3.1 Introduction

Fibrous structure plays an important role in the function and behavior of both healthy and diseased biological tissues. For instance, structural changes in collagen and elastin fibers are particularly important in biomechanical remodelling of many dense connective tissues which are composed of a dense extracellullar network of collagen and elastin fibers embedded in a ground matrix. Thus, the quantification of fiber architecture is an important step in developing an understanding of the mechanics of planar tissues in healthy and diseased state.
So far, numerous techniques have been developed for the investigation of the fibrous structure of soft tissues. For instance, among the optical techniques dedicated to tissue structure characterization, SALS allows the determination of collagen alignment in thin slices of tissue such as heart valves, intestinal submucosa and engineered heart valve tissue [81–83]. Other developed techniques able to investigate collagen fibre structures include small angle X-ray scattering [84], elastic scattering spectroscopy [85] and microscopic elliptical polarimetry [86]. With these methods, an orientation fiber distribution can be found, which represents the contribution of all collagen fibers embedded in the tissue. More detailed techniques to obtain information on the collagen organization include some optical modalities whose principles have already been explained in the previous chapter. They are confocal reflection laser scanning microscopy [87,88], autofluorescence and second harmonic generation using multi-photon microscopy [89,90]. Among these techniques, SALS offers a relatively simple and inexpensive way to pro-

vide semi-quantitative structural information about the localized arrangement of tissue fibers on a macroscopic scale [91]. SALS working process consists on an incident light beam which traverses a tissue sample interacting with some type of dielectric inhomogeneities. At each inhomogeneity border, part of the incident radiation is transmitted, another part is reflected and depending on the type of analyzed tissue a portion of radiation is absorbed. From a physical point of view, the incident laser light causes oscillating dipoles, which in turn emit light at the same wavelength (λ) of the incident beam in all directions. So, at different points in space for each scattered wave, fictitious light sources are created and interfere between each other. Finally, the portion of light transmitted to the opposite surface of the sample is scattered outside the tissue and the corresponding spot is acquired through a camera and analyzed. The objective of SALS theory is to correlate the intensity of the scattered light measured at various angles relative to the incident light to some physically meaningful quantity able to give information about the structure and the isotropic or anisotropic nature of fibrous samples. The low or high grade of anisotropy in a fibrous sample depends on the density and characteristics of the embedded fibres. Traditional SALS techniques are only capable of detecting structures that have dimensions within the order of the wavelength of the incident light beam (i.e. $\lambda = 633\ nm$). Typically, the eccentricity and orientation of the scattered light spot which is related to the amount of radiation that traverses the tissue and is scattered outside in the opposite surface of the sample, gives information on the dispersion and orientation of the embedded fibers. SALS imaging is best used when a tissue-wide microstructure investigation is required and damage to the sample is a non-issue. To date, SALS has been applied on soft tissues following uniaxial mechanical testing or fixation under load to study the microstructure-derived mechanical properties and characterize healthy or diseased tissues. In constitutive model development, SALS is a powerful experimental complement to mechanical testing of soft tissues with the direct inclusion of these microstructure maps. Several research groups have been using SALS to map the gross fiber orientation of soft membrane connective tissue. However, the device and analysis methods used in their studies require extensive manual intervention and are unsuitable for large-scale fiber architectural mapping investigations.
In this work, an improved optical device based on SALS technique has been developed. It allows for rapid data acquisition, automated high spatial resolution specimen positioning, and new analysis methods suitable for real-time large-scale mapping studies during mechanical biaxial test. The implementation of dedicated numerical simulations and extensive validation experiments revealed that the optical device can accurately measure fiber orientation for sample thicknesses higher than 1 mm to an angular resolution of about 1 degree. To demonstrate and validate the new device's capabilities, structural validation measurements from 3D printed fibrous samples are presented. Furthermore, customized *in-silico* simulations based on a Finite Element Monte Carlo (FE-MC) algorithm have been implemented in order to better understand the physical phenomena laying behind the propagation of light in fibrous media and so, the working process of our novel optical system. Monte Carlo (MC) is a stochastic modeling technique earlier used for radiation transport, which has been introduced for light propagation. MC method for photon transport (e.g. light transmission) is used for simulating how photons are scattered and absorbed within a certain medium. Indeed, it describes the "random walk" of photons in a turbid medium (e.g. biological

tissue) [92]. The MC method has been used to simulate light propagation in tissues for a variety of biomedical applications such as near-infrared spectroscopy, diffuse optical imaging, photoacoustic tomography and light-based therapies [93].
Finally, the SALS setup has been integrated in a customized biaxial testing machine, already existing at our laboratory, in order to perform real-time tissue microstructure characterization during biaxial test. In particular, a sample of porcine aorta and a sample of human aorta affected by ascendic thoracic aorta aneurysm (aTAA) have been tested.

3.2 Theoretical background

3.2.1 Basics on light propagation in fibrous tissues

The interaction of light with a certain medium depends on its optical properties which are a quantification of the physical phenomena occurring when the medium is traversed by a light wave (i.e. absorption, reflection and scattering). For all those phenomena each medium shows different behaviors depending on both its intrinsic optical properties and the wavelength of the incident radiation. The most relevant optical property that causes light scattering is the refractive index (*n*). Indeed, light scattering can be described as scattering by structures that have different refractive index from the surrounding medium, or as scattering by a medium with a continuous but fluctuating refractive index. Two types of scattering can exist. The Mie scattering which occurs when the structure or refractive index fluctuations are bigger compared to the wavelength of the incident light beam and, the Rayleigh scattering which, on the contrary, occurs when the structure or refractive index fluctuations are smaller compared to the wavelength. In case of soft biological fibrous tissues, light scattering is due to the different refractive index of the embedded fibers, especially the collagen ones, with respect to the surrounding isotropic environment (i.e. extracellular matrix). Since the dimensions of collagen fibers (50-150 μm) are much bigger than the incident wavelength (typically 500-1300 nm in biomedical applications), Mie scattering occurs when light traverses biological tissues. An important role is played also by the shape of the embedded fibers which can be approximated to arrays of cylinders.
Besides the refractive index, the optical properties of a generic biological tissue sample are described in terms of absorption coefficient, μ_a (mm^{-1}), scattering coefficient, μ_s (mm^{-1}), and scattering function, *p(θ,ψ)* (sr^{-1}), where θ is the deflection angle of scatter and ψ is the azimuthal angle of scatter. In general, the definition of the scattering function is appropriate when describing light scattering in thin tissue samples. In case of light scattering in a thick tissue sample, the scattering function is simplified to an average coefficient called anisotropy coefficient ($g = \langle \cos\theta \rangle$). This is because in a thick sample where the embedded fibers are randomly oriented and multiple scattering occurs, the ψ angle dependence of scattering is averaged and hence ignored, and the multiple scattering averages the angle θ such that it can be described by *g* [94]. With the purposes of characterizing biological tissues, their scattering properties can be defined in terms of reduced scattering coefficient which depends on the scattering coefficient (μ_s) and the anisotropy factor (g) through the following formula:

$$\mu_s' = \mu_s(1 - g) \tag{3.1}$$

The reduced scattering coefficient also depends on the wavelength of the radiation travelling into the medium, such dependence is described by the following equation:

$$\mu_s' = a * \left[\frac{\lambda}{(500(nm)}\right]^{-b} \tag{3.2}$$

or alternatively,

$$\mu_s' = a * \left[f_{Ray}\left(\frac{\lambda}{(500(nm)}\right)^{-4} + (f_{Mie}) * \left(\frac{\lambda}{(500(nm)}\right)^{-b_{Mie}}\right] \tag{3.3}$$

where b is adimentional and is called "scattering power", a is equal to μ_s at a wavelength of 500 nm and scales the wavelength-dependent term in both (3.2) and (3.3), f_{Ray} and f_{Mie} are dimensionless values connected to Rayleigh and Mie scattering respectively (i.e. $f_{Mie} = 1 - f_{Ray}$). Thus, in (3.2) and (3.3) both the Rayleigh and Mie scattering contributions are taken into account for the calculation of the reduced scattering coefficient. Based on the physical characteristics of the medium where light diffuses, one component can dominate over the other one or vice versa, or also they can simultaneously exist with similar contributions [94].
Given a light beam of a certain wavelength traversing a biological fibrous tissue sample and then getting scattered outside, the shape of the corresponding scattered spot depends on the wavelength and the characteristics of the sample such as the orientation and dispersion of the embedded collagen fibres. In particular, the eccentricity of the spot can give a quantification of the isotropic or anisotropic grade of the sample based on the circular or elliptical shape respectively. In case of anisotropy, the main orientation angle of the fibers is calculated with respect to the major axis of the scattered ellipsoid spot. Given a red light beam (λ=633 nm, typical of SALS technique) traversing a fibrous biological tissue, two cases can be distinguished based on the sample thickness. If the thickness is smaller than 700 μm the dominant visible phenomenon occurring within the sample can be approximated to Fraunhofer diffraction from an array of cylinders [80]. In this case, the major axis of the scattered ellipse is perpendicular to the preferential fiber direction so that a fiber with an angular orientation of ϕ, scatters light intensity to an angular orientation of $\phi + \frac{\pi}{2}$ (Figure 3.1a). On the contrary, if the sample thickness is higher than 700 μm, scattering of light by multiple layers of fibrous structures occurs and the phenomenon of Multiscattering of light, layer by layer, occurs (Figure 3.1b). In this latter case, the major axis of the scattered ellipse is parallel to the preferential fiber direction and the resulting scattered ellipse is larger due to the longer optical path traversed by the light beam inside the tissue sample [95].
In this work, through the implemented *in-silico* FE-MC simulations and the results provided by the validation test on 3D printed fibrous samples, it has been demonstrated that the new optical system based on SALS technology developed in this work provides an accurate and reliable method for real-time quantification of the gross fiber structure of samples having thickness higher than 700 μm. Its suitability for the opto-mechanical characterization of thick fibrous biological tissues has been further assessed and proved with *in-vitro* experimental measurements on healthy and aTAA aorta samples.

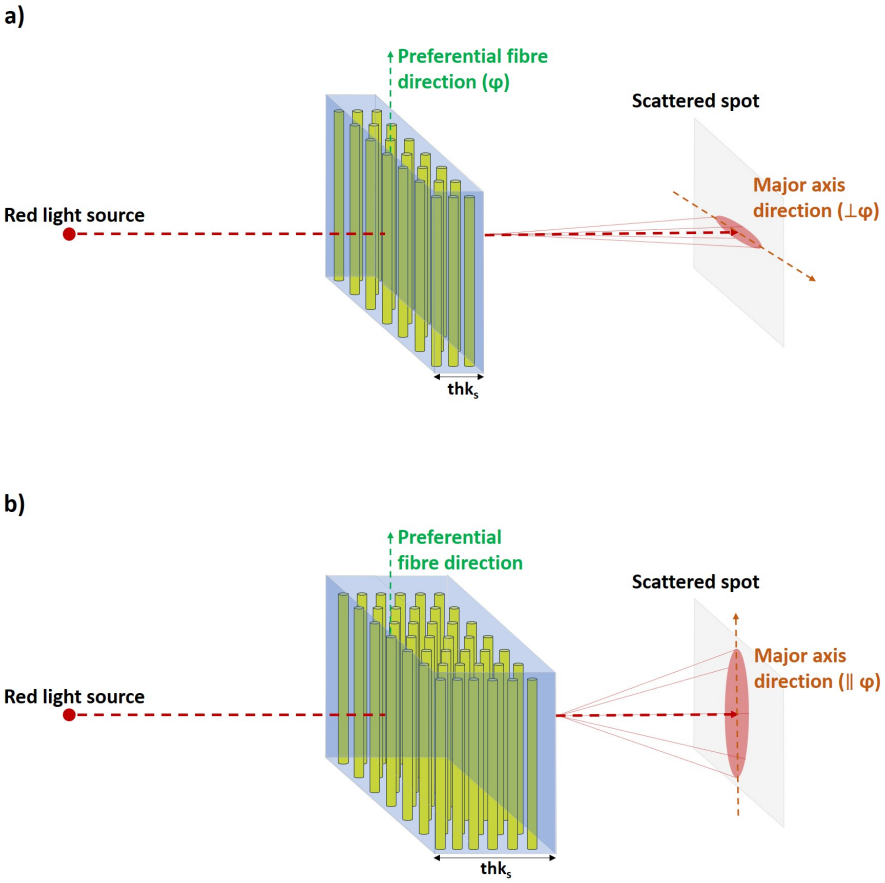

Figure 3.1: *Schematic of a) Fraunhofer diffraction and b) Multiscattering physical principles (**thk$_s$**: sample thickness).*

3.2.2 Theory behind simulations of light propagation in biological tissues

According to several studies based on the implementation of simulations of light propagation in anisotropic media (e.g. fibrous biological tissues), the working flow can either follows a deterministic or a probabilistic approach. Both approaches are explained in detail in the following dedicated sections.

Isotropic and anisotropic diffusion theory

The deterministic approach to light propagation theory is based on the solutions of the light diffusion equations which calculate the reflectance or the transmittance from a multilayered and laterally infinitely extended slab having a certain thickness (l_z). The equations can either be expressed in space or time domain. The formulation describing

the light flux in time domain is the following [96–98]:

$$U(x,y,t) = \frac{1}{2}(D_x D_y D_z)^{-0.5}(4\pi c)^{-\frac{3}{2}} t^{-\frac{5}{2}} exp\left(-\frac{x^2}{4D_x ct} - \frac{y^2}{4D_y ct} - \mu_a ct\right) \times \sum_{n=-\infty}^{\infty}\left((u - z_{1n})exp\left(-\frac{(u-z_{1n})^2}{4D_z ct}\right) - (u - z_{2n})exp\left(-\frac{(u-z_{2n})^2}{4D_z ct}\right)\right) \tag{3.4}$$

Knowing the light flux and by exploiting the Fick's law of radiative transfer [99], the light reflectance and transmittance can be retrieved from equation (3.4). The definition of the transmittance or the reflectance in (3.4) depends on the parameter *u* which is a spatial coordinate along z-direction. Supposing that the height of the medium (along z) is l_z, by setting $u = 0$ the relation $R(x,y,t) = -U(x,y,t)$ defines the reflectance, while, by setting $u = l_z$, the relation $T(x,y,t) = U(x,y,t)$ defines the transmittance. Regarding the other parameters of equation (3.4), *c* is the light speed in the investigated medium which depends on the refractive index (*n*) of the medium itself, D_x, D_y and D_z are the diffusion tensors which depends respectively on the effective scattering coefficients along the three spatial directions (μ'_{sx},μ'_{sy} and μ'_{sz}) as following:

$$D_x = \frac{1}{\mu'_{sx}} \tag{3.5}$$

$$D_y = \frac{1}{\mu'_{sy}} \tag{3.6}$$

$$D_z = \frac{1}{\mu'_{sz}} \tag{3.7}$$

Finally, the parameters z_{1n} and z_{2n} are given by the following relationships:

$$z_{1n} = 2nl_z + 4nz_b + z_0 \tag{3.8}$$

$$z_{1n} = 2nl_z + (4n-2)z_b - z_0 \tag{3.9}$$

$$z_0 = \frac{1}{\mu'_{sz}} \tag{3.10}$$

$$z_b = \frac{2(1+R_{eff})}{3\mu'_{sz}(1-R_{eff})} \tag{3.11}$$

where R_{eff} is the fraction of photons which is internally diffusely reflected at the boundary [99].
In spatial domain, the reflectance (*R(x,y)*) and the transmittance (*T(x,y)*) are solved by

using the following formula [96]:

$$U(x,y) = \frac{1}{4\pi\sqrt{D_x D_y D_z}} \sum_{n=-\infty}^{\infty} \left((u - z_{1n}) \left(\left(\frac{x^2}{D_x} + \frac{y^2}{D_y} + \frac{(u-z_{1n})^2}{D_z} \right)^{-0.5} + \sqrt{\mu_a} \right) \right.$$
$$\times \frac{exp\left(-\sqrt{\mu_a} \sqrt{\frac{x^2}{D_x} + \frac{y^2}{D_y} + \frac{(u-z_{1n})^2}{D_z}} \right)}{\frac{x^2}{D_x} + \frac{y^2}{D_y} + \frac{(u-z_{1n})^2}{D_z}}$$
$$-(u - z_{2n}) \left(\left(\frac{x^2}{D_x} + \frac{y^2}{D_y} + \frac{(u-z_{2n})^2}{D_z} \right)^{-0.5} + \sqrt{\mu_a} \right)$$
$$\left. \times \frac{exp\left(-\sqrt{\mu_a} \sqrt{\frac{x^2}{D_x} + \frac{y^2}{D_y} + \frac{(u-z_{2n})^2}{D_z}} \right)}{\frac{x^2}{D_x} + \frac{y^2}{D_y} + \frac{(u-z_{2n})^2}{D_z}} \right) \tag{3.12}$$

where, again as in the previous case, the reflectance is given by $R(x,y) = -U(x,y)$, setting $u = 0$ in equation (3.4), and the transmittance by $T(x,y) = U(x,y)$, setting $u = l_z$.
From both spatial domain and time domain representations (i.e. (3.4) and (3.12)), light diffusion is isotropic if $D_x = D_y = D_z$, otherwise is anisotropic. Therefore, from this relationship, since the diffusion tensor depends on the effective scattering coefficient , media where this coefficient is constant along all the spatial directions, are defined as isotropic. But, this cannot be always true. Indeed, a medium is considered isotropic also when its density and so, its optical properties (e.g. refractive index, scattering coefficient) randomly varies. This random spatial variation implies a density statistics of the properties of the medium which are independent on the direction of observation. On the other hand, media characterized by optical properties which are not spatially constant or whose variation is not random but depends on the observation point, are anisotropic. Biological tissues can belong to both category (anisotropic or isotropic media), because the refractive index and consequently the scattering properties can change randomly or not with respect to a 3D spatial coordinates. This depends on the type of tissue.

Monte Carlo method applied to light transport in media

The probabilistic approach to light propagation theory is based on the application of MC algorithm. It is a category of computational methods which uses random number generation for the propagation of photons in a stochastic manner. Due to its versatility, this method has been applied in different fields and for more than two decades it has been largely used for simulating light transport in biological tissues [100, 101]. MC method is assumed as the gold standard to model light transport in tissues because it has been demonstrated to be a flexible and rigorous solution to the problem of light transport in highly scattering media possessing complex structures (e.g. biological tissues). Indeed, many studies have highlighted the higher accuracy of MC method with respect to the deterministic application of diffusion theory, in modeling light transmission and reflection in fibrous-mimicking media [96, 97, 102].

MC method is based on the initialization of a package constituted by a certain number of photons (i.e. usually around 10^6) which propagates through the investigated medium following a trajectory randomly defined step-by-step by a certain step-size and two deflection angles [103, 104]. These three parameters are randomized according to a stochastic parameter *(ξ)*, whose values are within the range $[0, 1]$, that is defined as following [103]:

$$\xi = \int_a^x p(x)dx \tag{3.13}$$

where *p(x)* is a probability density function which defines the distribution of x over a certain interval [a,b] such that:

$$\int_a^b p(x)dx = 1 \tag{3.14}$$

According to equation (3.13), for each step of the algorithm the step-size of a photon (s) is calculated based on the sampling of the probability for the photon's free path [103]:

$$p(s) = \mu_t exp(-\mu_t s), s \in [0, \infty) \tag{3.15}$$

where *(μ_t)* is the transport coefficient which is given by the sum of both absorption and scattering contributions, $\mu_t = \mu_a + \mu_s$. By applying equation (3.13) the value of the step-size, s, is retrieved as function of the random variable *(ξ)* and the mean transport free path length ($\frac{1}{\mu_t}$) as following:

$$s = \frac{-ln(\xi)}{\mu_t} \tag{3.16}$$

The deflection angle*(θ)* and the azimuthal angle *(ψ)* are calculated in a similar way. In particular, for the deflection angle calculation, in case of Mie scattering of light, the probability density function proposed by Henyey and Greenstein is exploited [103]:

$$p(cos(\theta)) = \frac{1 - g^2}{2(1 + g^2 - 2g\cos\theta)^{\frac{3}{2}}}, \theta \in [0, \pi) \tag{3.17}$$

where g is the anisotropy coefficient. It follows that, by applying again equation (3.15), the deflection angle as function of ξ and g is given by the following relationship:

$$\cos\theta = \frac{1}{2g}\left[1 + g^2 - \left(\frac{1 - g^2}{1 - g + 2g\xi}\right)^2\right], g \neq 0 \tag{3.18}$$

$$\cos\theta = 2\xi - 1, g = 0 \tag{3.19}$$

For the azimuthal angle calculation, the probability density function is uniformly distributed within the range $[0, 2\pi]$ and so possesses a constant value equals to $\frac{1}{2\pi}$. By applying equation (3.15), the azimuthal angle is given by the following formula as function of ξ [103]:

$$\psi = 2\pi\xi \tag{3.20}$$

The photons are injected orthogonally into the investigated medium and each one possesses a certain weight that is progressively updated at each step of the algorithm based

on the phenomena which the photons undergo through the tissue, i.e. absorption and/or scattering. So, known the photon weight at the i^{th} step of the process (w_i), at the $(i+1)^{th}$ step, the new weight assigned to the photons is:

$$w_{i+1} = aw_i; a = \frac{\mu_s}{\mu_a + \mu_s} \tag{3.21}$$

where *a* represents the fraction of scattered photons which transmits through the medium, while $1 - a$ the fraction of absorbed photons. In case of refractive index mismatch, the trajectory is updated according to the Snell's law [104]:

$$n_i \sin\theta_i = n_t \sin\theta_t \tag{3.22}$$

where θ_i is the deflection angle which a certain photon hits the boundary with, θ_t is the transmission angle to be updated, while n_i and n_t are the indices of refraction of the incident and transmitted medium respectively. On the other hand, the probability that a photon is internally reflected is determined by the Fresnell reflection coefficient [104]:

$$R(\theta_i) = \frac{1}{2}\left[\frac{\sin(\theta_i - \theta_t)^2}{\sin(\theta_i + \theta_t)^2} + \frac{\tan(\theta_i - \theta_t)^2}{\tan(\theta_i + \theta_t)^2}\right] \tag{3.23}$$

If $R(\theta_i) > \xi$, a photon is internally reflected, otherwise the photon exits the medium [103, 104].

Summary

A deep study of light propagation in soft biological tissues has been conducted and, in particular, the state of art of simulations based on the propagation of light through fibrous media has been deeply investigated. From an accurate analysis of several previous works, the two ways to implement such simulations are: *i)* the implementation of the deterministic approach by using the solution of the radiative transport equations based on classic diffusion theory, and *ii)* the implementation of the stochastic approach based on Monte Carlo methods. Finally, the latter approach has been chosen for the purposes of this work. Indeed, some studies have demonstrated that in case of thin media where the light source is placed very close to the plane of investigation of the light fluence rate, the use of MC methods in the simulation of light propagation brings to much more accurate results than the use of the solution of the diffusive equation [96, 97, 102].

3.3 *In-silico* simulation of light propagation in soft fibrous tissues

The FE-MC *in-silico* simulations implemented in this work, simulate the propagation of light in fibrous media characterized by one or two fiber families. In this latter case, the two fiber families differ in orientation and can have same or different number of fibers (i.e. fiber density).

3.3.1 Matherials & Methods

Finite Element model

The numerical model considered for the simulations is based on a large number of photons (e.g. 10^6) propagating through a fibrous *in-silico* sample. The incident photons

work as a point light source. The codes, written in Matlab and C++, have been customized starting from the work of Leino et al. [93]. Basically, the simulations are set up by imposing a light source penetrating a three-dimensional block domain constituted by an isotropic extracellular matrix (EM) with embedded fibers (EF) (Figure 3.2).

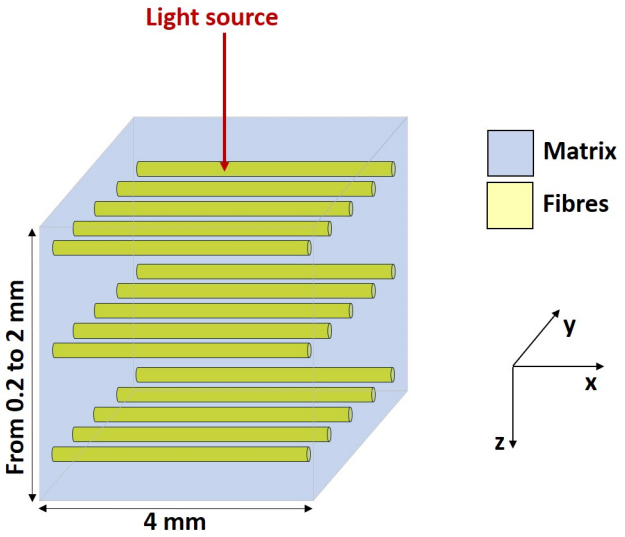

Figure 3.2: *Summary scheme illustrating the geometry of the media simulated in the simulations. The orientation angle ((α)) of the fibers is taking with respect to the x-axis. In case of two fiber families, the families differ for orientation angle. So, in this specific case the medium is characterized by one fiber family with* $\alpha = 0°$.

The block has a square section with a 4 mm side and a thickness (thk) value defined according to the different simulations. The fibers are organized in one or two families identified by a main orientation angle (α_i) in the light-incidence plane, a fiber fractional number (D_i) and an overall fiber fractional density (ρ). The D_i and ρ values are respectively given by

$$D_i = \frac{N_i}{N_{tot}} \times 100 \tag{3.24}$$

and

$$\rho = \frac{V_{EF}}{V_{EM}} \times 100 \tag{3.25}$$

where N_i represents the number of fibers belonging to the i-th family, N_{tot} is the fiber total number, V_{EM} is the total volume of the block taken as the medium to be investigated, and V_{EF} is the volume of the fibres embedded within the medium. The tissue model is defined according to its absorption (μ_a) and scattering coefficients (μ_s), causing the light energy decay. The μ_a and μ_s coefficients are assumed to be equal in the whole domain and their values are set according to the characteristic soft tissue range [94,105] ($\mu_a = 0.01mm^{-1}$ and $\mu_s = 0.28mm^{-1}$) The optical differences between the EF and the EM domain were modeled in terms of their scattering anisotropy (g) and their refractive index (n), which are the main responsible for the modification of the light spot. By assuming that the anisotropy of the specimen is completely given by the fibers, the EF are assumed to be characterized by forward scattering ($g = 0.8$) while the EM domain will produce an isotropic response ($g = 0$) [106]. Concerning the n parameters, the EM

was assumed to contain the majority of water within the tissue ($n_{EM} = n_{water} = 1.36$), while the EF were assumed as the dry component ($n_{EF} = 1.46$) [92]. The domains were discretized by using a dedicated custom algorithm to generate a tetrahedral mesh and customize the fiber D_i and α_i parameters, as exemplified in Figure 3.3.

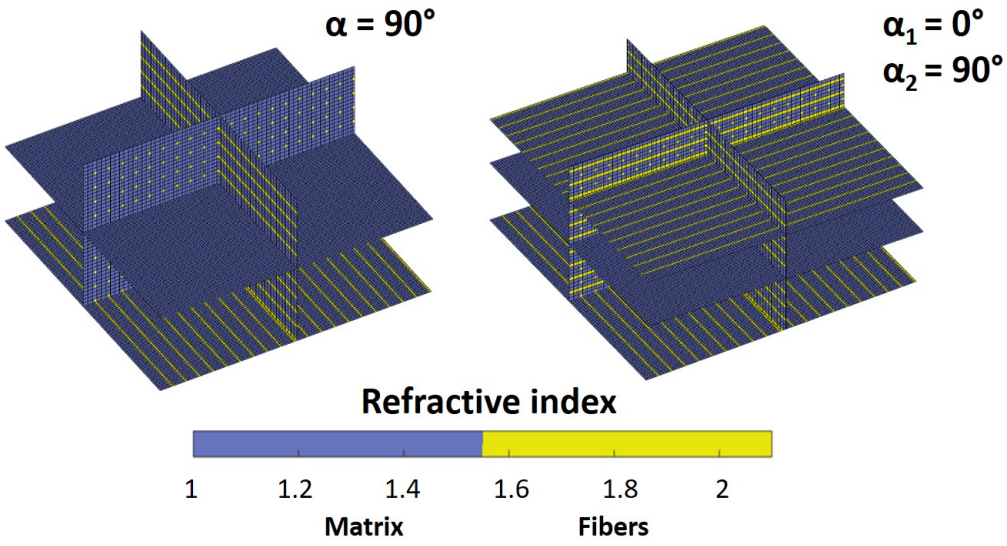

Figure 3.3: *Cross-sections of the 3D refractive index structures referred to two of the in-silico media built and tested through the FE-MC developed program.*

The fibers were modeled as cylindrical structures with a diameter of 50 μm. The light stimulus was modeled as a point source with a photon numerosity of 10^6 particles. For all the simulations, the numerical solution was obtained by adopting a Monte Carlo method for the photon transport and random scattering through a media, by using and customizing a state of art method explained in detail below.

Monte Carlo algorithm

Regarding the implementation of the used stochastic approach to light diffusion, in Figure 3.4 the flowchart of the implemented MC algorithm [93] is shown. At the beginning, it is characterized by the generation of a photon package, which represents the light source, and is placed at the center of the upper face of the sample. The weight assigned to the photon package is an index of the amount of photon and its initial value is unitary (i.e. $w_0 = 1$). After the photon initialization, the program enters in the main loop which ends as soon as the medium has been entirely traversed by the simulated beam along its thickness. Within the loop, a random scattering length is assigned to the photons, that is affected by the total attenuation coefficient (μ_T) and so, by both the absorption and scattering coefficients as expressed in equation (3.15). However, the scattering coefficient taken into account for the simulations is about thirty times higher than the absorption one. That makes the absorption coefficient negligible in the update of the photon package. Therefore, at each step, the weight is reduced by a factor of $exp(-\mu_T s)$ with s given by equation (3.16), and the photons move along a straight line to the interface of the next element or anyway to a next position as long as the current generated scattering length is valid. If the scattering coefficient is not constant along

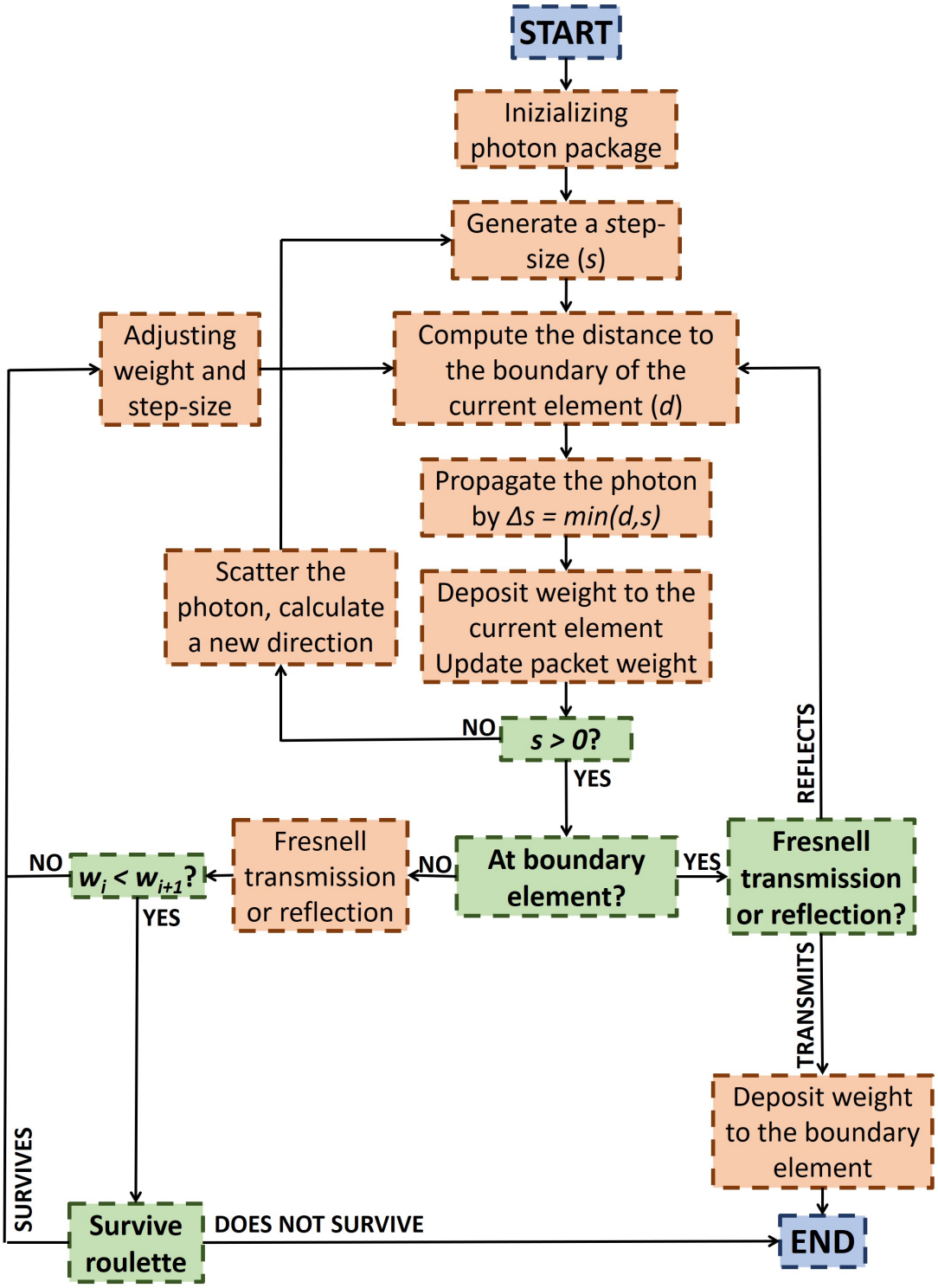

Figure 3.4: *Schematic of the flowchart of the MC algorithm adopted for the simulation of light propagation in fibrous soft tissue.*

the path, the changes are taking into account by properly scaling the remaining length

by a factor of:

$$\mu_{sCurr}/\mu_{sNext} \tag{3.26}$$

where μ_{sCurr} is the scattering coefficient of the element which the photons are propagating through, while μ_{sNext} is the scattering coefficient of the element which the photons are entering. If a change of refractive index occurs along the path, photons undergo Fresnell reflection and are transmitted to the next elements with a properly modified propagation direction. As soon as the photon package propagates the assigned distance, a new scattering event occurs and, thus, a new direction is assigned to the photons according to equations (3.17), (3.18) and (3.19) and a new scattering length is generated. The photon package terminates ((i.e. photon weight typically less than 10^{-3})) at the end of the main loop of the simulation which includes the computation domain and the surviving roulette which randomly influences the weight of the package at the end of each iteration. Such procedure is performed in order to avoid the computation of excessively long paths with a low influence on the final results. The main result of the simulations are 2D and 3D light fluence rate and exitance distribution (respectively Φ and *J*) maps. For each element of the mesh, the fluence rate at a generic element *i* is retrieved through the following formula:

$$\Phi_i = \frac{w_i}{\mu_{a,i} N V_i} \tag{3.27}$$

where w_i is the weight of the photon absorbed into the element *i*, *N* is the number of photons, V_i is the volume of the element *i* and $\mu_{a,i}$ is the absorption coefficient of the element *i*. While, the exitance at a generic element *i* is calculated in the following way:

$$J_i = \frac{w_i}{N A_i} \tag{3.28}$$

where A_i is the area of the element *i*.
The final result of each FE-MC simulation implemented for each structural model is a 3D map of the photon fluence rate. Thus, for each step along the depth of the medium a 2D isocurve map of the photon fluence rate is retrieved and plotted. The shape of the resulting fluence rate isocurves are then analyzed through a dedicated segmentation algorithm in order to retrieve information on the inner sample structure in terms of fiber orientation and dispersion.

Light spot analysis and structural models

By means of the described MC program the isocurve fluence rate maps of the light transmitted through a determined surface at a generic depth *i* of the medium are generated and, by means of an edge-detection segmentation algorithm, the isocurves of the maps are fitted in such a way to generate the corresponding scattered light spot. This can be a circle or an ellipse with a certain eccentricity depending on the structure and the optical properties of the medium. In particular, the eccentricity ($E = \sqrt{1 - \frac{b^2}{a^2}}$, where *a* and *b* denote the elliptical major and minor pattern axes, respectively) and orientation of the resulting spot are calculated. The applied segmentation algorithm allows the study of the variation of the resulting spot eccentricity as function of the thickness and density of the sample, and the resulting spot orientation as index of preferential

Table 3.1: *Geometrical parameters related to the structure of the simulated in-silico samples. α_1 and α_2 are the orientation angles of the first and second fiber family respectively. D_1 and D_2 are the fiber fractional number of the two fiber families respectively*

Model	α_1	α_2	D_1	D_2
1	0º	-	100	-
2	90º	-	100	-
3	0º	90º	50	50
4	0º	-90º	80	20

direction of the embedded fibres which are responsible for refractive index mismatches through the medium.

- A first set of simulations (S_1) was imposed to investigate the influence of fiber distribution on the light diffraction of SALS. In particular, the maps of the light fluence rate of the scattered spot at the bottom surface of each embedded structure listed in Table 3.1 have been computed. To identify both the Fraunhofer diffraction and Multiscattering phenomena, the different α_i combinations were evaluated for both low (0.2 mm) and high thickness (1.3 mm) specimens characterized by a constant value of ρ (i.e. 26%). For each simulation, the results were post processed in order to obtain the isocurve fluence rate maps at the specimen side opposite to the light source. The isocurves were fitted according to an elliptical pattern to evaluate the corresponding ellipses eccentricity (E) and orientation angle (ϕ).

- A second set of simulations (S_2) was imposed to achieve a deeper insight on the influence of specimen thickness on the light scattering. In particular, the thickness of the specimen was varied from a minimum of 0.2 mm to a maximum of 2 mm with a constant step of 0.1 mm. The value of ρ was kept constant at 26%. A single fiber family was included within the domain with $\alpha_i = 0^o$. The E parameter resulting from the fluence pattern analysis was calculated according to the different thickness values.

- A third set of simulations (S_3) was imposed to investigate the combined effect of thickness and fiber density modifications on the fluence pattern in the Multiscattering conditions for SALS. The thickness range was chosen to guarantee the dominance of the Multiscattering phenomena, with a minimum of 1 mm up to a maximum of 2 mm through a constant step of 0.1 mm. The value of ρ was varied between 0.5% up to 26%. A single fiber family was included within the domain with $\alpha_i = 0^o$. The E parameter resulting from the fluence pattern analysis was calculated according to the different thickness and density values. Additionally, the values were averaged along the specimen thickness to isolate the effect of the ρ variations.

- Lastly, a fourth set of simulations (S_4) was imposed to highlight the influence of different densities of the fiber families within the same specimen always remaining

in the Multiscattering regime. To achieve this, the ρ and thickness parameters were kept constant at 26% and 1.3 mm respectively. Two fiber families were included within the domain with $\alpha_{1,2} = 0^o/90^o$ and the density parameters $D_{1,2}$ were varied. In particular, the density balance was modified by starting from the extreme anisotropic case of $D_1 = 100\%$ and $D_2 = 0\%$ to the isotropic $D_1 = 50\%$ and $D_2 = 50\%$, with gradual percentage steps of 7.1%.

The simulation conditions of sets S_1, S_2 and S_3 are all summarized in Table 3.2.

Table 3.2: *Optical properties of the simulated in-silico media.*

Set	α_1	α_2	D_1	D_2	ρ	thk
S_1	0°	-	100%	-	26%	0.2-2 mm
S_2	0°	-	100%	-	0.5%-26%	0.2-2 mm
S_3	0°	90°	100-50%	0%-50%	26%	1.3 mm

3.3.2 Results

The fluence maps resulting from the first set of simulations (S_1) of light propagation through the four embedded fiber structure models listed in Table 3.1, are shown in Figure 3.5. For each model, the fluence map of the Multiscattering phenomenon, which occurs when the thickness of the fibrous sample is higher than 700 μm (i.e. simulated sample thickness of 1.3 mm), is presented together with the Fraunhofer diffraction phenomenon, which occurs when the thickness of the fibrous sample is smaller than 700 μm (i.e. simulated sample thickness of 0.2 mm). The corresponding *E* and ϕ values are reported in Table 3.3. It is possible to highlight that the specimen exhibiting the lowest eccentricity values is from the $\alpha_{1,2} = 0^o/90^o$ case, regardless of the thickness. In this case, the pattern resulted in a quasi-circular light spot (isotropic), consequently the ϕ parameter was considered as meaningless. On the other hand, the maximum of *E* was encountered for specimens with high fiber alignment like the $\alpha_1 = 0^o$ and $\alpha_1 = 90^o$ (i.e. Model 1 and Model 2 in Table 3.1).

Table 3.3: *Table summarizing the E and the ϕ parameters resulting from the S_1 simulations at different fiber distributions and thickness values.*

Case		thk 0.2 mm		thk 1.3 mm	
$\alpha_{1,2}$	$D_{1,2}$	E	ϕ	E	ϕ
0°	100%	0.79	89.4°	0.92	0.7°
90°	100%	0.80	0.3°	0.91	88.9°
0^0/90°	50%-50%	0.31	isotropic	0.27	isotropic
0^0/90°	80%-20%	0.65	89.7°	0.78	0.32°

Regarding the S_2 set, the scattered spot eccentricity variation as a function of sample thickness was successfully evaluated. The results are presented in Figure 3.6a. The eccentricity trend reveals a transition region (0.6 mm < thk < 1 mm) between the Fraunhofer diffraction region and the Multiscattering region, in which the light spot shape

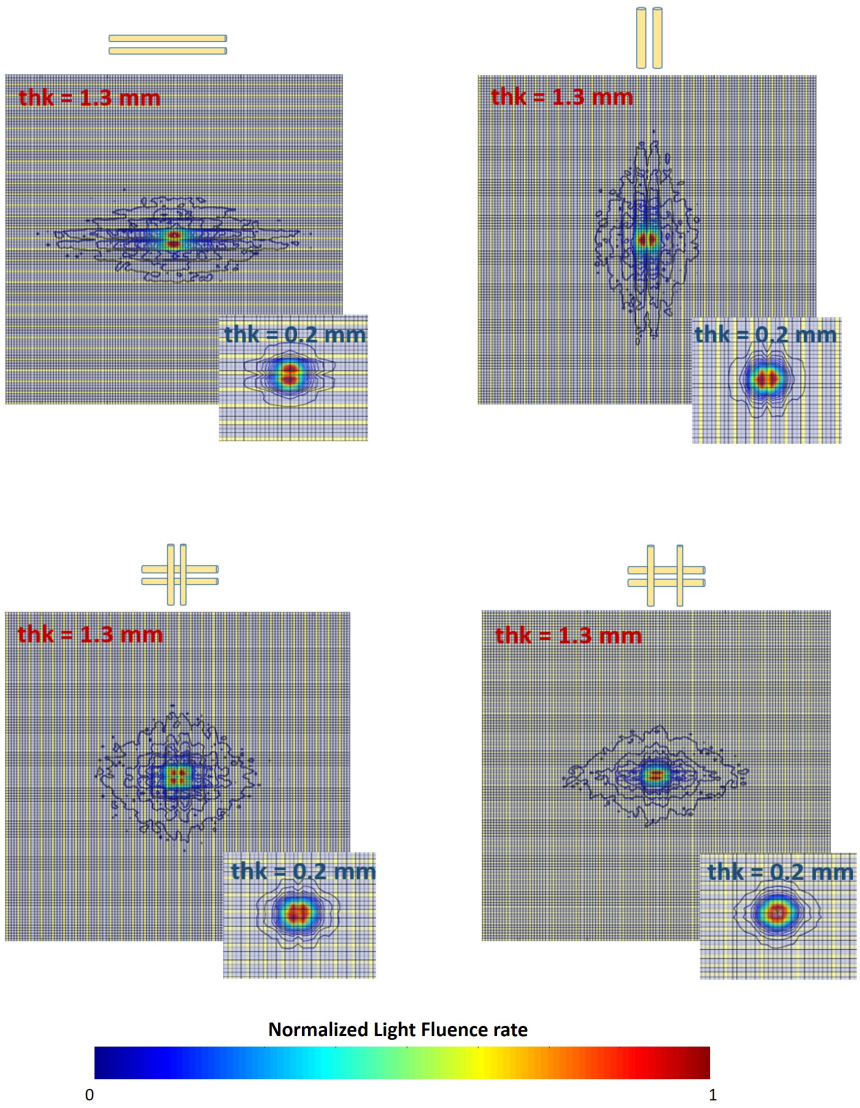

Figure 3.5: *Isocurve fluence maps from simulation set S_1:* $\alpha_1 = 0^o$,$\alpha_1 = 90^o$, $\alpha_{1,2} = 0^o/90^o$ *and* $D_{1,2} = 50\%/50\%$, $\alpha_{1,2} = 0^o/90^o$ *and* $D_{1,2} = 80\%/20\%$.

changes and the two phenomena eventually overlap.
The results from S_3 set, revealing the eccentricity variation as a function of both specimen thickness and fiber density, are shown in Figure 3.6b and Table 3.4. The three-dimensional plot (Figure 3.6b) reveals that wide ranges of E (from a minimum of 0.22 up to a maximum of 0.95) can be reached by varying the thickness and the fiber density of the specimen. The sample which is taken into account is characterized by an internal fiber structure that corresponds to model 1 in Table 3.1 (i.e. one fibre family oriented at 0^o).
Furthermore, from the eccentricity data shown in Figure 3.6b, an analysis based on the first and second order statistics has been done taking into account the data eccentricity arrays varying as function of the fiber density for each considered thickness (i.e. 1, 1.1, 1.2, 1.3, 1.4, 1.5, 1.6, 1.7, 1.8, 1.9 and 2 mm). The mean and the standard deviation

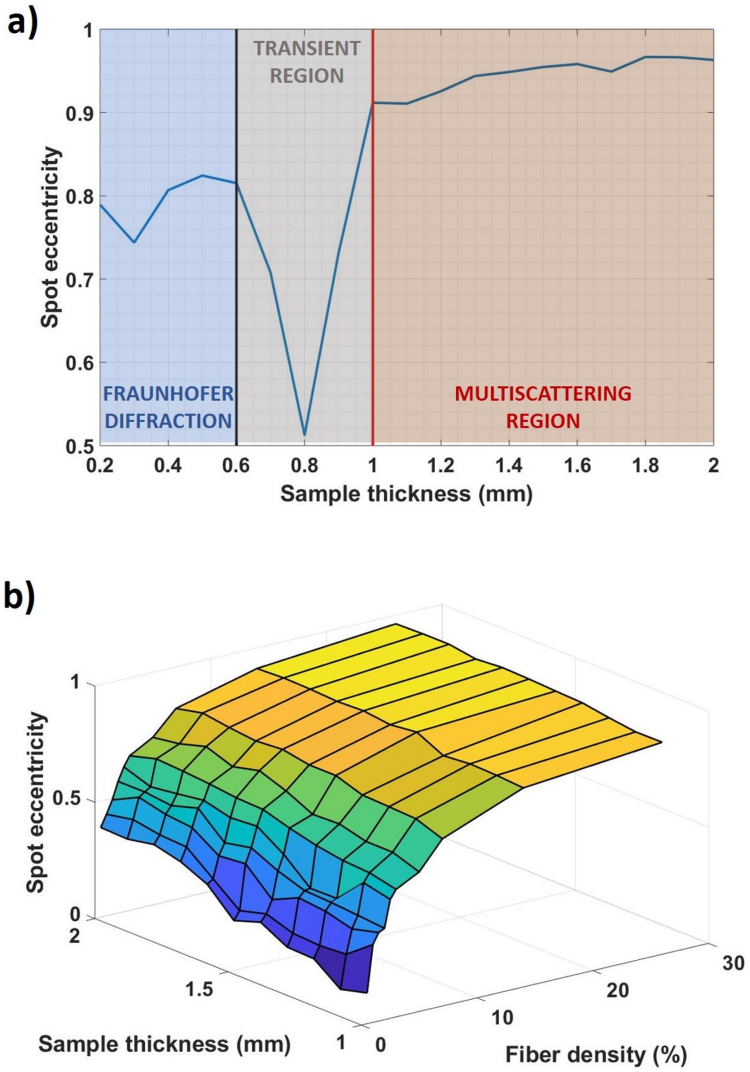

Figure 3.6: *a)Eccentricity (E) resulting from simulation set S_2 as a function of specimen thickness. The three main zones are depicted: Fraunhofer diffraction region, Transient region and Multiscattering region; b) Results from simulation set S_3: 3D plot of spot eccentricity as a function of both specimen thickness and fiber density.*

calculated for each considered array of E data (along the sample thickness), are listed in Table 3.4.

The results from the fourth and last investigation (S_4) are shown in Figure 3.7. The structure initially involved, corresponds to model 1 in Table 3.1. Thus, one fiber family oriented along one direction is embedded in the medium (i.e. one fiber family oriented along 0^o). Then, the number of fibers oriented at 90^o, and so perpendicular to the already existing fiber family, is progressively increased. The increase of fibers along 90^o stops when the density of such fiber family (i.e. oriented at 90^o) equals the density of the other one (i.e. oriented at 0^o). The final structure corresponds to model 3 of Table 3.1, so the final eccentricity value is supposed to be very small (i.e. at least smaller than 0.5). In the plot, the eccentricity values related to the light spot scattered at the

Table 3.4: *Mean and standard deviation related to the eccentricity data arrays calculated for each considered thickness (i.e. 1, 1.1, 1.2, 1.3, 1.4, 1.5, 1.6, 1.7, 1.8, 1.9 and 2 mm) as function of density of fibres aligned along 0°. The symbol* ***std*** *states for standard deviation.*

Fiber density (%)	Eccentricity ($mean \pm std$)
0.5	0.2686 ± 0.1102
1	0.3376 ± 0.0902
1.5	0.4364 ± 0.0736
2	0.4867 ± 0.0744
2.5	0.5474 ± 0.0720
3	0.6362 ± 0.0521
5	0.6962 ± 0.0563
7	0.7981 ± 0.0391
14	0.8926 ± 0.0255
26	0.9453 ± 0.0205

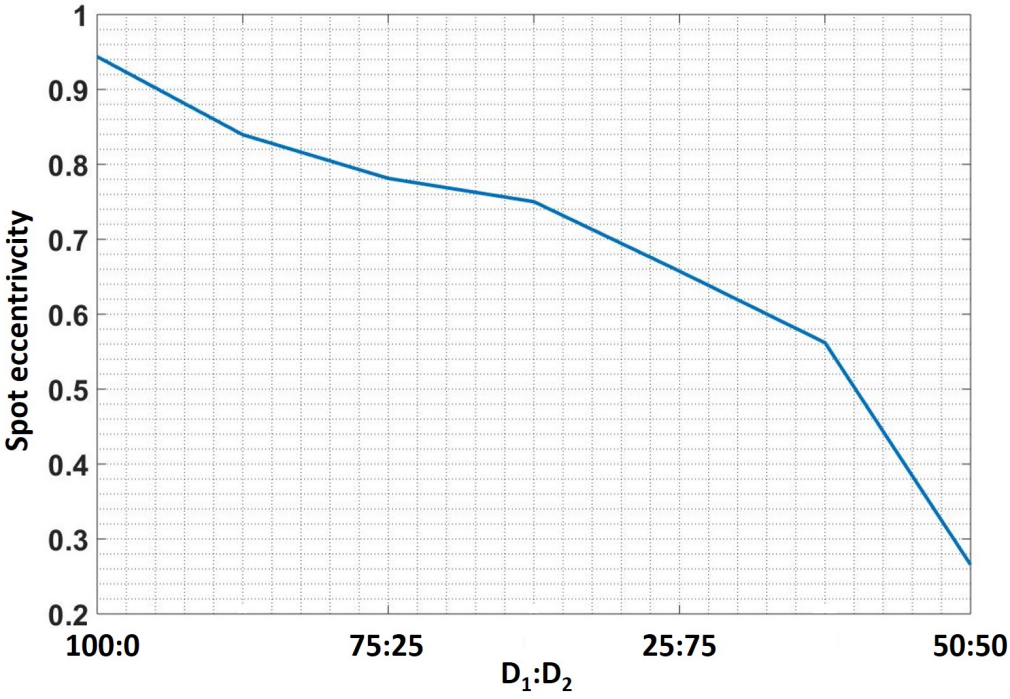

Figure 3.7: *Results from simulation set S_4 in terms of eccentricity variation as a function of different D_1/D_2 values.*

bottom surface of the sample are reported as function of the density ratio D_1/D_2 which is related to the fiber density of each family.

3.3.3 Discussion

Collagen fibers are the main responsible for the anisotropic mechanical behavior of fibrous soft biological tissues such as artery wall. It is through collagen characterization that it is possible to retrieve important tissue properties which bring to a better comprehension of the healthy and pathological states. The results from the *in-silico* simulations implemented in this work and their further manipulations, revealed the effects of light propagation through fibrous media, such as soft biological tissues, and the corresponding influence according to different factors like the specimen thickness, the fiber density and the grade of anisotropy which is given by the amount and dispersion of the embedded fibers, and their spatial orientation. With the sets of simulations implemented in this work, it is demonstrated that the grade of anisotropy can be qualitatively assessed by analyzing the light spot propagating through the entire sample and then scattered outside for different range of thicknesses. The simulations from the S_1 set demonstrated the effect of specimen thickness on the light scattering of specimens with different fiber distributions. Figure 3.5 gives an overview of the light spot shape for the different sample inner structures listed in Table 3.1. It was demonstrated that it was always possible to acquire information concerning the distribution of fibers within the simulated specimen, regardless of the tissue thickness. As already reported in previous studies [82, 107], the light spot obtained from SALS irradiation of specimens at 0.2 mm thickness produces orientation angles perpendicular to the resultant fiber direction and high eccentricity values for the anisotropic cases, according to the Fraunhofer diffraction theory. This phenomenon is for example proved by the 90° specimen with 0.2 mm thickness, revealing E and ϕ equal to 0.80 and 0.3°, respectively (Figure 3.5 and Table 3.3). In opposition with this behavior, the specimen with perpendicular fiber families having the same density (almost isotropic) with 0.2 mm thickness exhibits an eccentricity of 0.31. Concerning the 1.3 mm thickness specimens, the Multiscattering effect is instead predominant for the SALS irradiation. It is interesting to highlight the reported ϕ values, as apparently a relationship with the orientation angles from the Fraunhofer diffraction exists. Indeed, as demonstrated from previous works [95, 108], the calculated orientation angle values are in line with the Multiscattering theory. That is, the ϕ values from the 1.3 mm thickness specimens correspond to the direction parallel to the fiber resultant angle. This trend is confirmed by the shift of about 90° between the ϕ values from the simulations of the 0.2 mm and 1.3 mm thicknesses, as reported in Table 3.3. The numerical values confirm the existence of both the phenomena of Multiscattering and Fraunhofer diffraction and its correct simulation. Moreover, results from simulation set S_2 offered a deeper insight of the effect of specimen thickness. The trend from Figure 3.6a revealed the existence of different zones, as the eccentricity value encountered modifications with the variation of the thickness. For thk below 0.6 mm, Fraunhofer diffraction was dominant, and eccentricity values were high and in line with the anisotropy of the simulated specimen. Between 0.6 mm and 1 mm, there is a transient region where both the Multiscattering and Fraunhofer diffraction phenomena occur. In this transition region, eccentricity values rapidly fall causing a lack of measurement accuracy as it was demonstrated also in some SALS studies from literature [109]. The E values demonstrate that the SALS irradiation for specimens with thicknesses falling within this transition range will produce unreliable patterns. Starting from 1 mm, Multiscattering effect becomes dominant, and the eccentricity encounters

a second rising, allowing again an evaluation of the simulated specimen anisotropy. So, summarizing the findings from the S_2 set of simulations, as a light beam traverses a fibrous medium three main regions can be distinguished based on the medium thickness:

- Fraunhofer diffraction region (i.e. sample thickness smaller than 600 μm): the light spot scattered outside the medium is small, the spot eccentricity is a reliable index for a qualitative measure of the spatial anisotropy. In case of anisotropy, the spot has the major axis perpendicular to the preferential fiber direction, as Fraunhofer diffraction is the predominant phenomenon;

- Transient region (i.e. sample thickness between 600 μm and 1 mm): the light spot becomes larger and the eccentricity values are not reliable in assessing the spatial anisotropy of the medium because the phenomenon of light scattering from multiple layers (i.e. Multiscattering) starts occurring. However, the optical path traversed by the beam through the sample is still too short to allow the light to diffuse predominantly along the preferential fiber direction. The unreliability of the eccentricity values in assessing the anisotropy of the sample is given by the fact that the two physical phenomena overlap.

- Multiscattering region (i.e. sample thickness higher than 1 mm): the light spot becomes much larger because of the longer optical path traversed by the beam, and the spot eccentricity becomes again a reliable index for a qualitative measure of the spatial anisotropy. In case of anisotropy, the spot has the major axis parallel to the preferential fibre direction, as Multiscattering is the predominant phenomenon.

Additionally, the results from simulation set S_3 demonstrate the effect of fiber density on the SALS spot. From Figure 3.6b, it is possible to compare the influence of the ρ parameter against the specimen thk. In Figure 3.8a and Figure 3.8b, the trends are clearly visible. The results showed that the scattered spot eccentricity rises by increasing the fiber density, as expected [110], given the increased contribution of the fibers on the light scattering. It is also worth to highlight the saturation effect occurring beyond 20% (Figure 3.8). It appears clear from an analysis of Table 3.4 and Figure 3.8 that, for sparse fiber distributions at low ρ values, the resulting eccentricity value does not permit a clear evaluation of the specimen status. Indeed, the variation of eccentricity values around a mean values increases as ρ decreases. The simulated trend also demonstrates that, beyond density value of about 20%, the thickness minimally influences the SALS spot eccentricity. This observation confirms that, under the assumption of a dense fiber matrix, the distribution can be individuated through SALS irradiation regardless of the thickness and the Fraunhofer diffraction – Multiscattering phenomena.
An additional confirmation is provided by the results of last simulation set S_4. Figure 3.7 clearly reports the SALS spot behavior as the fibers orientations are redistributed in a thick specimen. The E value falls from a high value (close to 1) to a value of 0.27, corresponding to the correct isotropy assumption given by the 50% - 50% symmetric case.

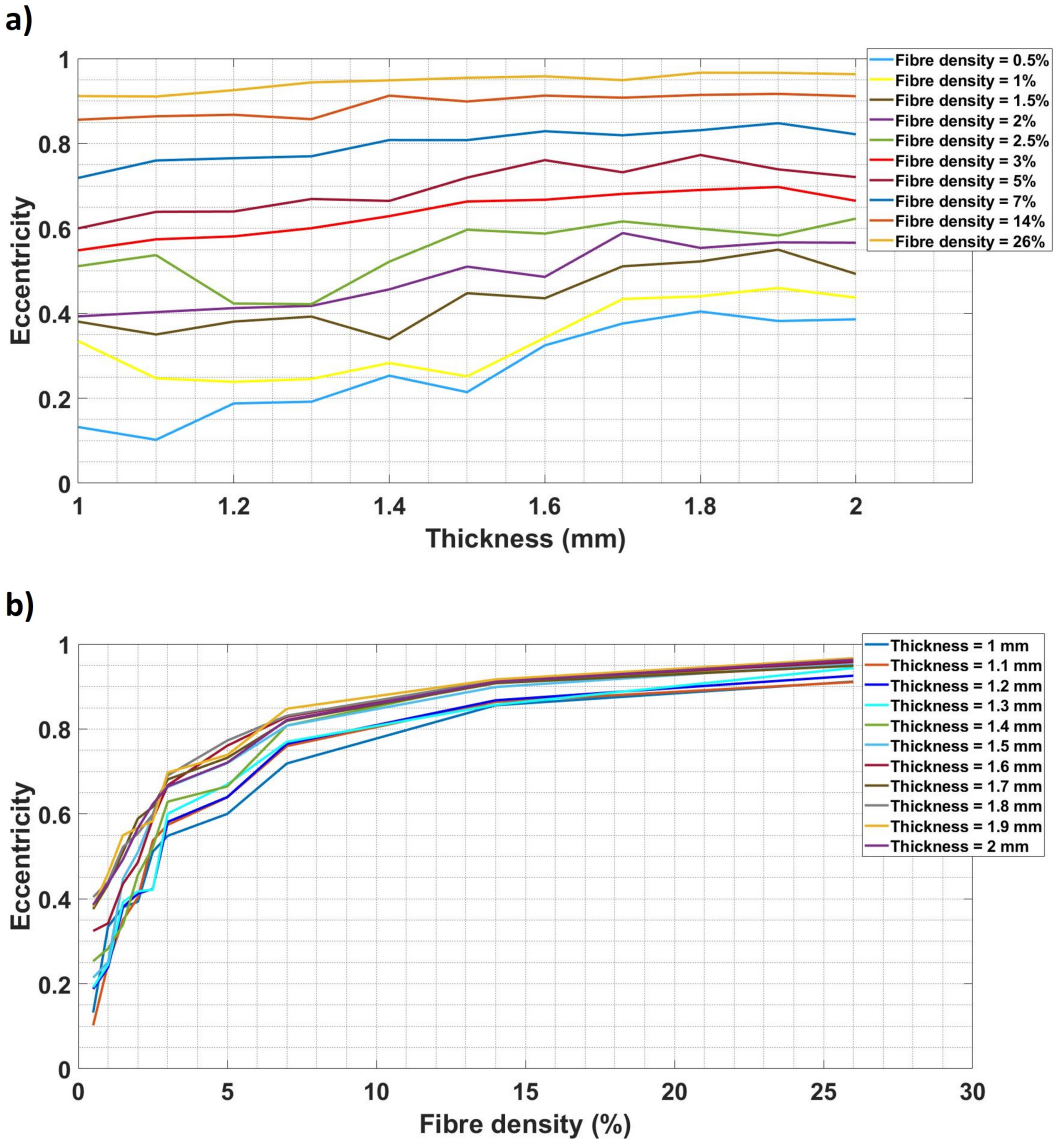

Figure 3.8: *Plots extracted by the 3D plot, presented in Figure 3.6b, showing the scattered spot eccentricity as function of a) thk in the Multiscattering region for different values of ρ; b) ρ for different thk in the Multiscattering region.*

3.4 SALS system

3.4.1 SALS platform development

Hardware and software modules

A specific custom setup based on SALS technique has been developed and integrated into a mechanical machine for uniaxial/biaxial testing previously developed at Biocardiolab. A schematic of the hardware part of the entire opto-machanical setup with a focus on the optical components, is given in Figure 3.10. The SALS system is based on an optical table on which a flexible structure, composed of two vertical rails and an horizontal one, is positioned. The horizontal rail can translate along the vertical

rails fixed on an alluminium breadboard. An HeNe laser source (unpolarized light at λ=633 nm and power=5 mW) is placed on the horizontal rail, while a fourth small rail, which is 30 cm long, is attached at the end of the horizontal one and holds a broadband dielectric mirror and an achromatic doublets (i.e. focusing length = 150 mm and working wavelength between 400 and 700 nm) which is a particular focusing lens having a structure that prevents chromatic dispersion of light within the working wavelength range. The focusing lens and the length of the rails where the optical components are held and can shift along, are disposed in such a way to take into account the final size of the focused light spot at the tissue upper surface, as pointed out in the schematic in Figure 3.9. In particular, the distances between each element and between focusing lens and tissue sample are set in such a way to generate a light spot focused on the sample with a diameter ranging from 90 to 100 μm. This is the traditional spot size used in most of scientific work based on SALS investigations. Distances between the optical

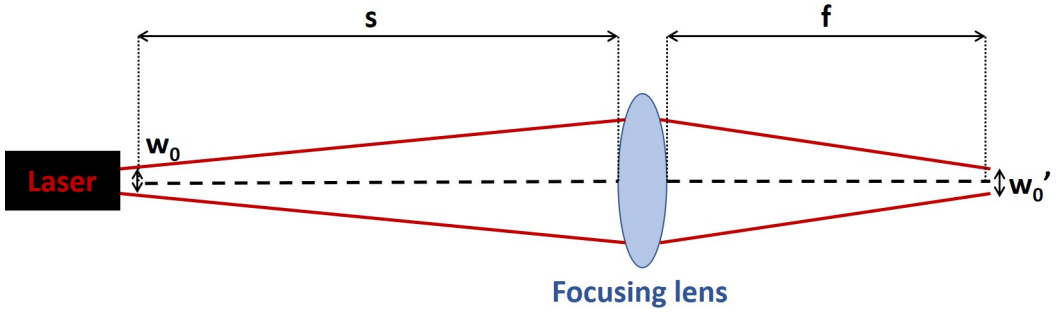

Figure 3.9: *Schematic of the focusing of a spherical Gaussian beam.*

components have been computed by exploiting the following equation which is derived from the theory of the focusing of a spherical Gaussian beam [111]:

$$w_0' = w_0 \frac{f}{\sqrt{(|s| - f)^2 + z_R^2}} \tag{3.29}$$

where w_0' is the focused beam diameter, w_0 is the initial beam waist, s is the distance between laser and focusing lens, f is the focusing length of the lens and z_R is the Rayleigh length which is a value that describes the curvature of the laser beam. For a better understand of the parameters appearing in equation (3.29), in Figure 3.9 a schematic drawing of the focusing of a Gaussian beam is shown.
Finally, a CCD camera module (resolution 0.03mm/pixel) completes the hardware part of the SALS setup. As it is shown in the schematic in Figure 3.10, the sample is placed perpendicular to the direction of the laser beam. In particular, it is usually placed on the holders of the biaxial testing machine which ensure that the sample is rightly perpendicular to the beam. Below the sample, the CCD camera is placed in order to acquire the light spot scattered outside the bottom surface of the sample. The post-processing of the acquired images of the light spot is performed by a dedicated software.
Regarding the software part, it is devoted to acquire in real-time the images of the light spot from the CCD camera and process them. In particular, data acquisition is obtained through a real-time processor (NI cDAQ-9132) and a custom LabView application was developed in order to control it, read the acquired data and through an integrated Mat-

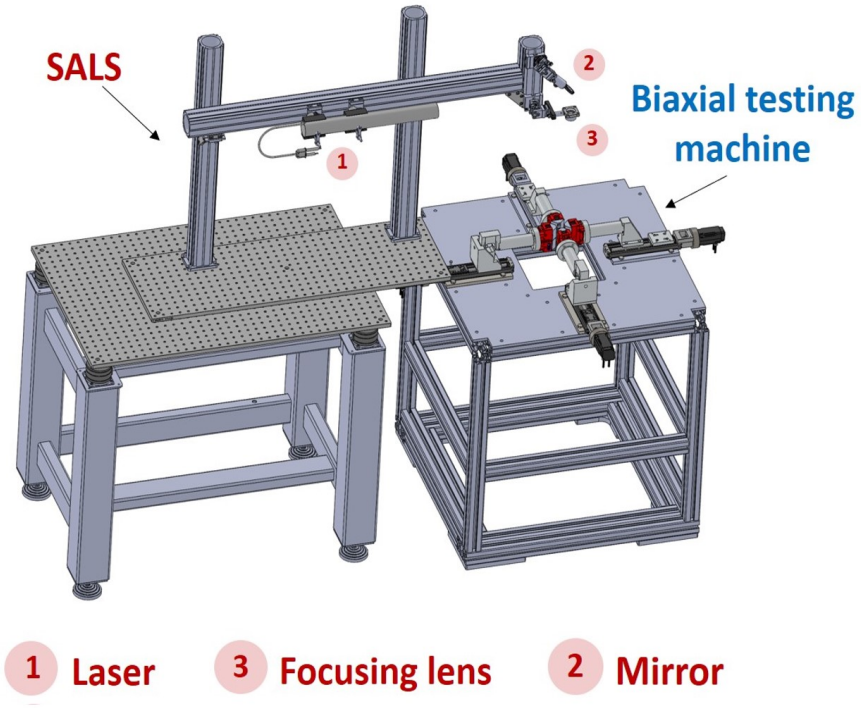

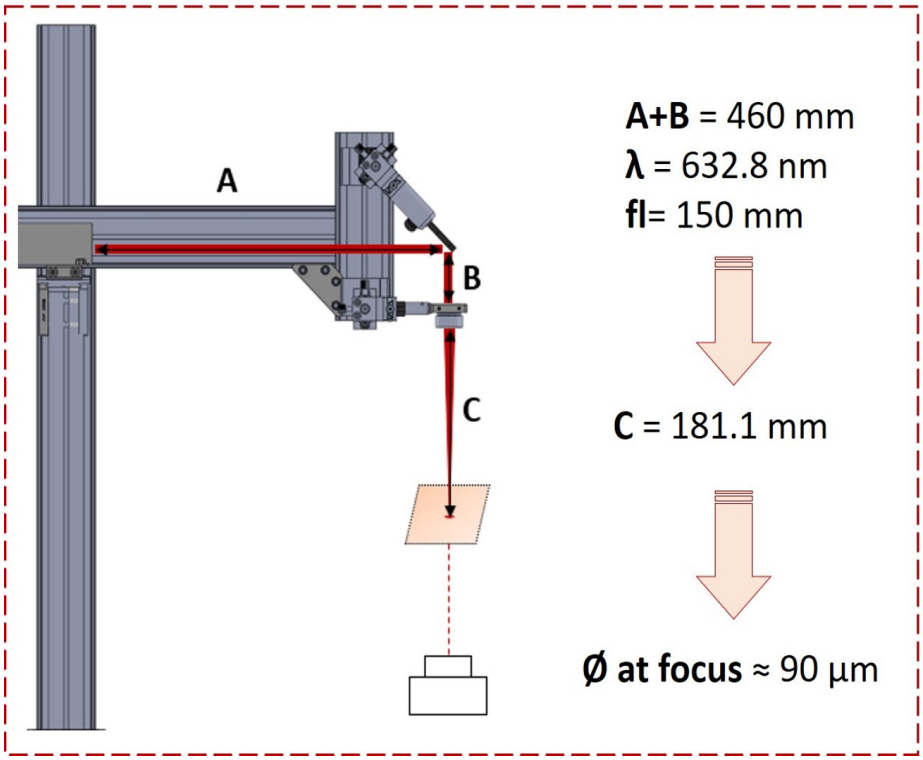

Figure 3.10: *Schematic of the developed SALS setup integrated into the already existing biaxial testing machine aimed to perform opto-mechanical characterization of tissues. On the bottom right of the figure, some specifics of the SALS setup are schematically shown.*

lab code, calculate the main parameters that are needed for SALS investigation of the sample structure. Thus, given an image of a light spot, the software computes in real-time:

- the eccentricity (E) through the formula:
  $E = 2\frac{\sqrt{\left(\frac{Axis_{major}}{2}\right)^2 - \left(\frac{Axis_{minor}}{2}\right)^2}}{Axis_{major}}$
- the orientation angle (α) of the ellipse from which the sample fiber preferential direction can be retrieved. The calculation of α properly changes based on the thickness of the sample under investigation as highlighted in the *in-silico* simulations that have been previously performed.

3.4.2 SALS platform validation

First, the new developed optical system has been validated. The validation of the optical

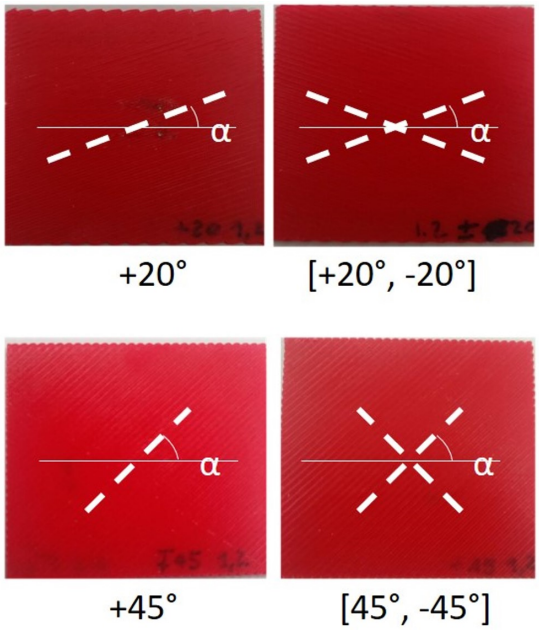

Figure 3.11: *3D printed polymeric specimens with different infill angles (+20°, [+20°,-20°], +45° and [+45°,-45°]) for the validation test on the SALS setup.*

system has been carried out through the analysis of 3D-printed fibrous samples having different inner structure and thickness of 1.3 mm, thus falling within the Multiscattering region. The samples have been designed with CAD and printed using thermoplastic polyurethane (TPU). In Figure 3.11 the four different fibrous structures taken into account for each 3D-printed TPU sample are shown. Regarding the structure having two fibre families, it is important to point out that the families have the same fiber density. The validation test consists on the SALS investigation of each single sample. Typically, the sample is positioned perpendicular to the direction of the laser beam, which is focused on the upper surface. The CCD camera acquires the light spot scattered from the opposite surface and the software part of the system computes the eccentricity of the

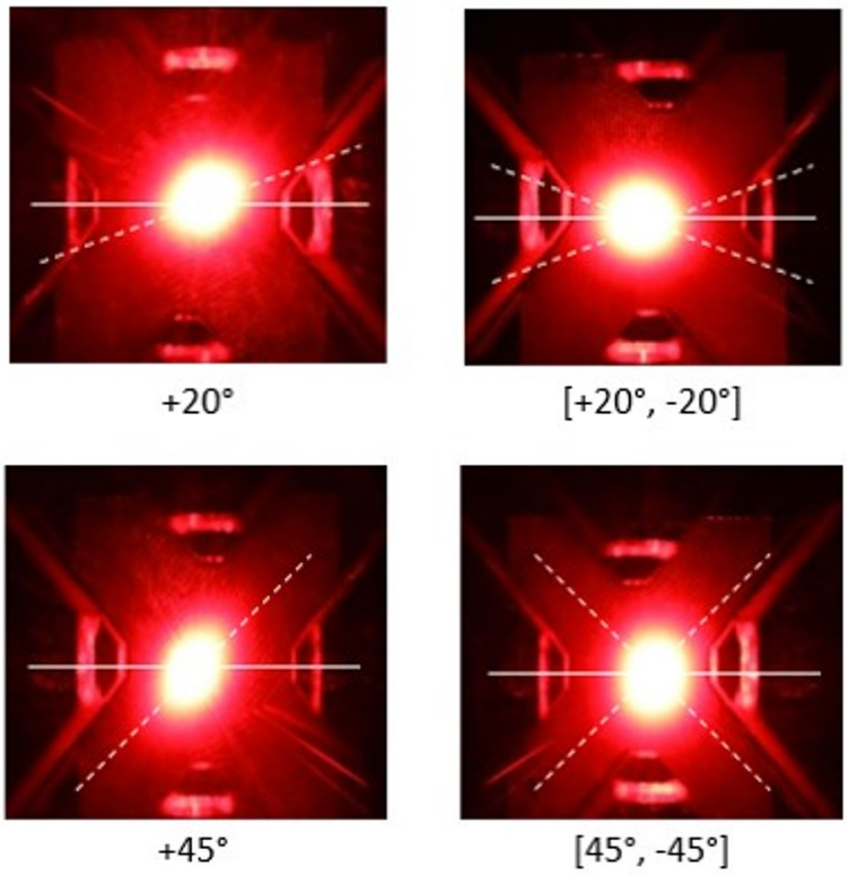

Figure 3.12: *SALS validation test on the four 3D-printed TPU samples.*

Table 3.5: *Eccentricity and orientation angle values resulted from the validation test for each investigated structure.*

Sample	Spot orientation angle (α)	Eccentricity (E)
$+20^{o}$	20.5^{o}	0.72
$\pm 20^{o}$	2^{o}	0.66
$+45^{o}$	44.24^{o}	0.7
$\pm 45^{o}$	isotropic	0.31

spot and its spatial orientation in real-time. In Figure 3.12 the scattered spot resulted from the SALS validation investigation of each polymeric sample is shown and in Table 3.4 the corresponding values of eccentricity and orientation angle are listed. From the results of the validation test, it was demonstrated that the developed optical system is able to retrieve information on the inner structure of fibrous samples in terms of spatial anisotropy and thus, fiber dispersion. Indeed, from the eccentricity values, the samples having one fiber family (i.e. oriented at +20^{o} and +45^{o}) or two fiber families not perpendicular between each other (i.e. [+20^{o}, -20^{o}]) resulted spatially anisotropic

(i.e. eccentricity values higher than 0.5/0.6). While the sample with two fiber families perpendicular between each other results isotropic (i.e. eccentricity values smaller than 0.5), as it was expected. Furthermore, the orientation angle values of the acquired scattered spots computed by the software, have been demonstrated to be reliable, with an accuracy error between 0.5º and 2º. In particular, for the structures with only one fiber family oriented at 20º and 45º the error is respectively 0.5^0 and 0.76º (less than 1º in both cases). For the structure with two fiber families oriented at 20º and -20º, the error is 2º. Indeed, the expected spot orientation angle would have been the average between the two fiber orientation angle, i.e. 0º. Regarding the structure with perpendicular fiber families, it behaves as a spatially isotropic medium, as expected. Indeed, the eccentricity of the corresponding scattered spot is smaller than 0.5 and the spot can be approximated to a perfect circumference which consequently does not have a specific spatial orientation.

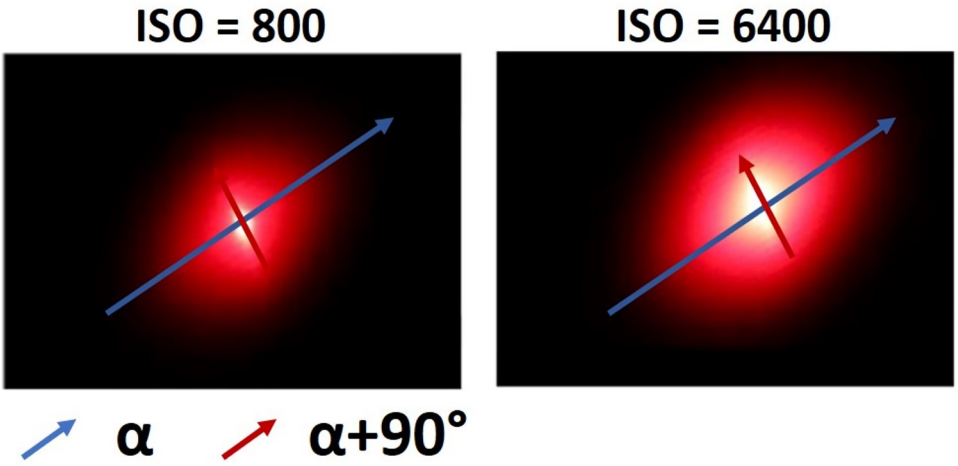

Figure 3.13: *Light fluence through the TPU sample with fibers oriented at 45º captured by varying the ISO filters of the CCD camera.*

Last but not least, by varying the ISO filters (i.e. from 800 to 6400) of the CCD camera devoted to acquire the light spot scattered outside the sample during SALS investigations, it has been observed that light first propagates along a direction which is approximately perpendicular to preferential fiber orientation, and then starts propagating parallel the fiber preferential direction.
This finding confirms the *in-silico* simulations. In Figure 3.13, the 3D printed sample with geometry structure made of one fiber family oriented at $\alpha = 45^{\circ}$ is taken into account. It can be noted that by setting low ISO filter values in the CCD camera, the light propagation in the first layers of the sample can be depicted. Indeed, the light propagates along $\alpha + \frac{\pi}{2}$ through the first layer of the sample (i.e. Fraunhofer diffraction). Then, by setting higher ISO values, the spot tends to grow (i.e. Transient region where the overlapping of Fraunhofer diffraction and Multiscattering occurs), until it starts orienting along α when the light propagates through a sufficient number of fibrous layers (i.e. Multiscattering). Therefore, the light propagation trends predicted by the light fluence maps resulting from the FE-MC simulations (Figure 3.6a) are experimentally

confirmed by the findings obtained from the validation test of the developed optical system.

3.4.3 *In-vitro* test on biological samples

After the validation of the system, opto-mechanical investigations on biological samples have been carried out through the integration of both the hardware and software parts of the optical setup into the biaxial testing machine. A fresh specimens of porcine

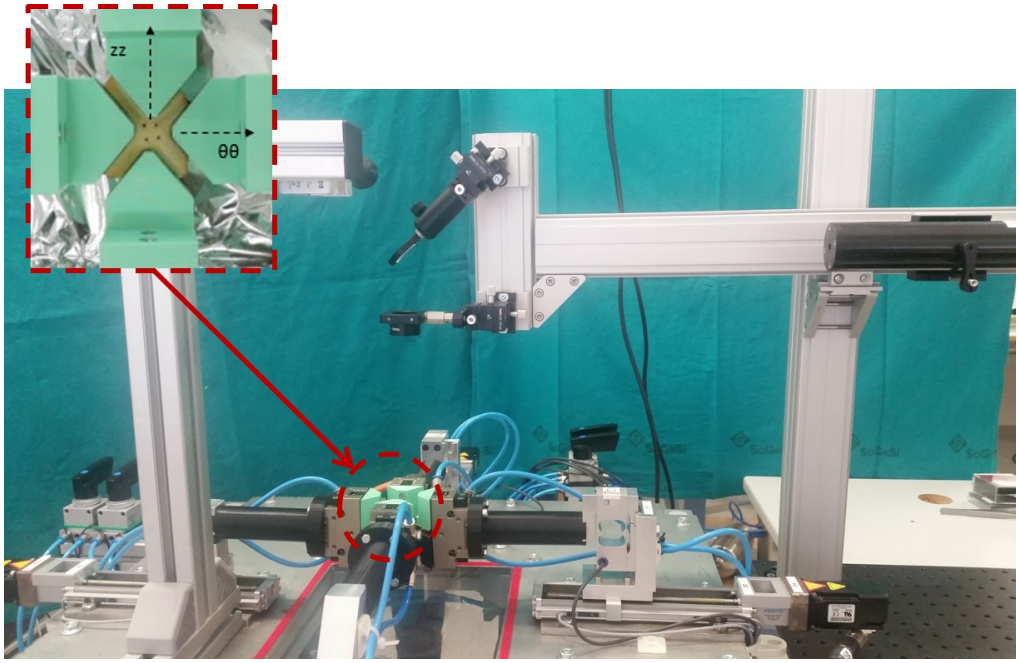

Figure 3.14: *Opto-mechanical setup ready for the performance of the in-vitro tests; the biological sample is clamped through the grippers of the biaxial machine and positioned perpendicular to the focused light beam.*

aorta, assumed as the healthy sample, and a sample of aorta affected by ascendic thoracic aorta aneurysm (aTAA) have been tested. The first tissue sample has been harvested from a frozen porcine heart, exhibiting a thickness of 1.8 mm. While, the aTAA sample has been harvested from a patient who underwent surgical procedure, exhibiting a thickness of 1.7 mm. Both the tissues have been cut to obtain square specimens with 30x30 mm dimensions, so that they could be positioned on the biaxial machine through some dedicated pneumatic grippers (Figure 3.14) connected to 4 linear screw drives (Festo) actuated by 4 servomotors (Kollmorgen), granting a displacement accuracy within the 0.1 mm range.
Regarding the mechanical part of the test, five different tension ratios $T_{\theta\theta} : T_{zz}$ (i.e. 1:1, 1:0.5, 1:0.75, 0.5:1) have been imposed, where $T_{\theta\theta}$ is the tension applied along the circumferential direction of the sample and, T_{zz} the tension applied along the longitudinal direction. Regarding the optical part, the ISO filters of the CCD camera have been set to detect the Multiscattering pattern (i.e. 8000). Figure 3.14 shows the hardware part of the opto-mechanical setup just before the performance of the *in-vitro* tests on the biological samples. For both samples, the biaxial test is performed for each tension ratio together with the optical analysis. The calculation of the eccentricity and orientation

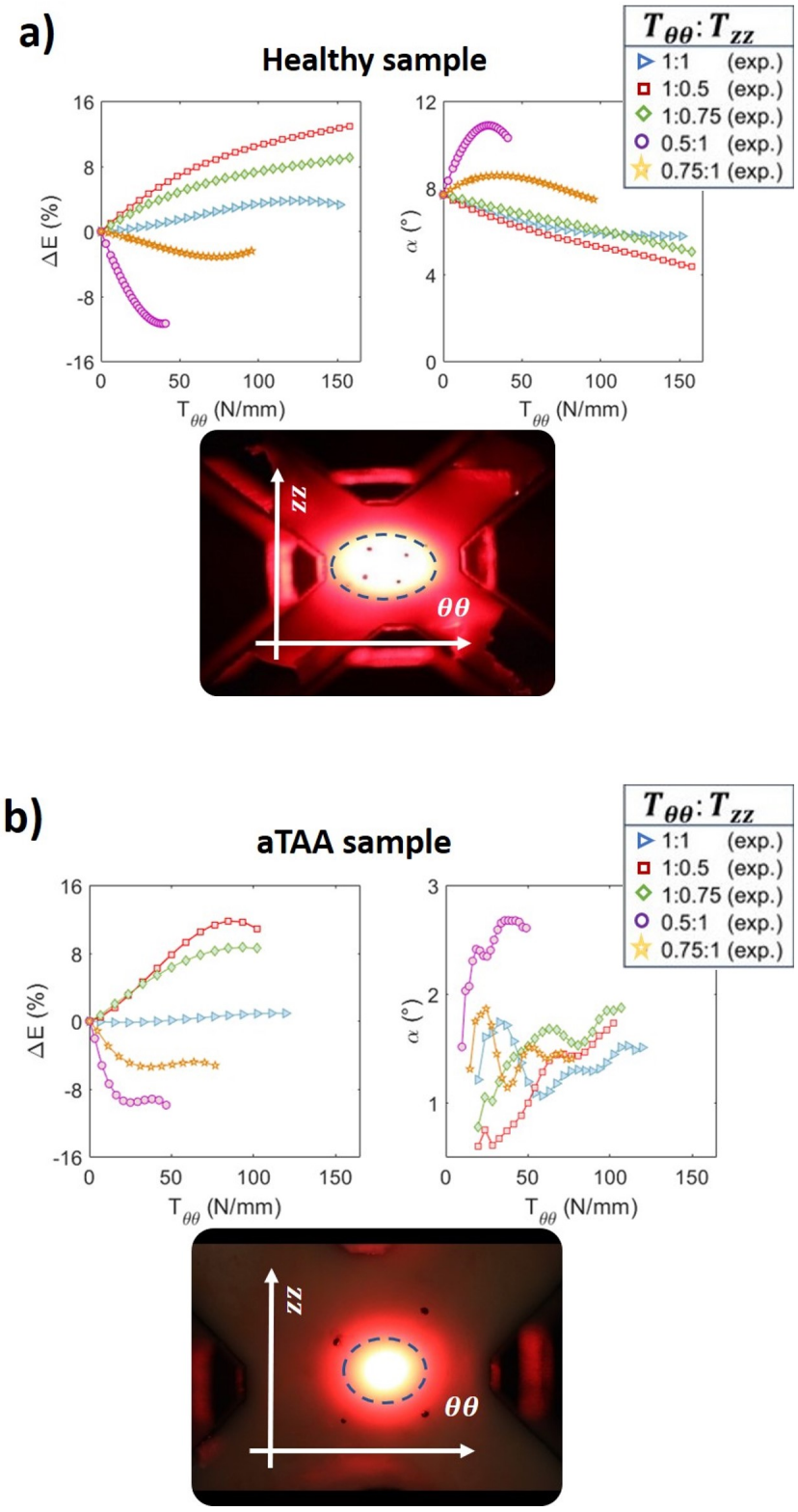

Figure 3.15: *Results of the in-vitro opto-mechanical test performed on a) the healthy sample and b) the aTAA sample.*

angle is calculated in real-time during each biaxial procedure and finally the variation of the light spot eccentricity calculated in percentage is retrieved along the duration of each measurement.
In Figure 3.15, the outcome of the *in-vitro* opto-mechanical tests performed on both healthy and aTAA biological samples are shown. Regarding the healthy sample (Figure 3.15a), the scattered spot is an ellipse directed along the longitudinal direction which the majority of fibers lays along, as expected and also confirmed by histology (Figure 3.16). The optical results from the opto-mechanical test show a high capability of fiber

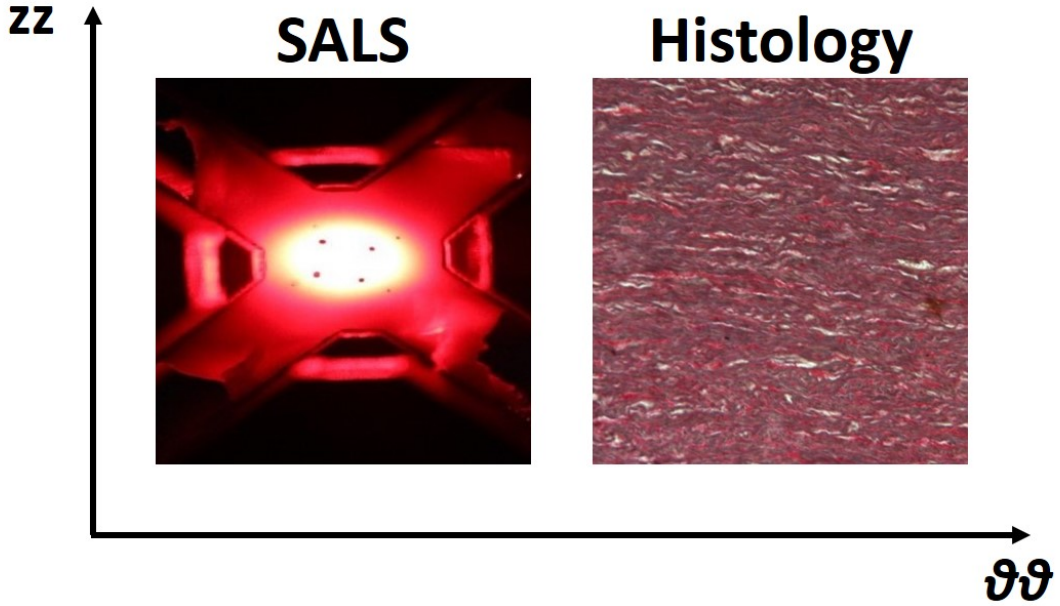

Figure 3.16: *SALS analysis confirmed by the hystological investigation of the porcine aorta sample, the preferential direction of the inner fibers lies along the circunferential direction.*

rearrangement in all the tested load conditions. The preferential fiber orientation (α) experiences a variation which is around 2.5^{o} at its highest values, and shows a continuous trend for all the imposed tension ratio. For what concern the variation of the scattered spot eccentricity which is a measure of the fiber dispersion inside the sample, for higher tension along the circumferential direction (i.e. tension ratio equals to 1:0.5 and 1:0.75), it tends to increase. This means that the embedded fibers are progressively rearranged and, it basically happens along the direction where the tension is higher, as expected. This mechanism results in a progressively increase of number of fibers directed along the circumferential direction and so an increase of the spot eccentricity. If the tension ratio is 1:1, the eccentricity variation is smaller because of the fiber recruitment process along the longitudinal direction as well. However, this values are positive because the recruitment along the circumferential direction is still more efficient and so affects a larger number of fibers with respect to the fiber recruitment along the longitudinal direction. For higher applied tension along the longitudinal direction (i.e. tension ratio equals to 0.5:1 and 0.75:1), the eccentricity variation values tend to decrease, meaning that the sample is trying to recruit as many fiber as possible along

the direction where the tension is higher (i.e. direction parallel to the minor axis of the ellipse), thus the eccentricity progressively decreases.
Regarding the aTAA sample, the ellipse along the circumferential direction is less pronounced with respect to the healthy tissue because the inner fibers are much more dispersed into the sample volume bringing to a modification of the mechanical behavior of the tissue as result of the aTAA pathology. The trends of the eccentricity variation, by varying the tension ratio, are very similar to the healthy case. However, the angle variations results very discontinuous in both initial values and trend shown during all the tested biaxial tension ratios. It means that fiber recruitment process in the aTAA sample does not work as good as in the healthy one, as expected.

3.5 Conclusive remarks

In this chapter, the development of an optical setup based on SALS technique for the characterization of the inner structure of fibrous soft tissues, preceded by the development and performance of FE-MC simulations for a better understand of the theoretical concept behind the propagation of light in thick fibrous media, has been reported. In the first stage involving the *in-silico* simulations, it has been verified that the analysis of a light spot resulting from a light beam which propagates through a fibrous medium and then is scattered outside, can provide information about the dispersion of the embedded fibers. In particular, the grade of anisotropy of the medium can be qualitatively assessed and, in case of a high spatial anisotropy along one direction (i.e. high number of fibers having the same spatial orientation), the preferential direction of the embedded fibers can be accurately retrieved. The recovery of such information slightly varies depending on the thickness of the investigated samples. Therefore, three main regions have been classified according to the sample thickness: *i*) Fraunhofer diffraction region, *ii*) Transient region and *iii*) Multiscattering region. Only in Fraunhofer diffraction and Multiscattering regions the analysis of the scattered light spot gives robust information about the inner structure of the investigated sample. Then, a study of the light spot eccentricity has been performed as function of inner fiber density. It resulted that the more is the number of inner fibers oriented along a preferential direction, the higher are the eccentricity values and thus, the higher is the sample spatial anisotropy as expected. After this feasibility study which allows to verify that a typical SALS device would properly work also with thick samples, the optical setup has been designed and assembled in both its hardware and software part. Then, such system has been validated by performing tests on thick 3D-printed samples with predetermined fiber structure. Also, the ISO filters of the camera used for the light spot acquisition have been set in such a way to acquire the entire spot resulting from investigation within the Multiscattering region. Finally, the optical system has been integrated into a customized biaxial testing machine and opto-mechanical tests consisting in real-time biaxial traction and optical analysis of fibrous sample structure, have been performed on healthy and aTAA aorta tissue samples. The feasibility of the entire opto-mechanical system has been demonstrated, since it is able to provide important information on the mechanical behavior of biological tissues giving an accurate insight on the fiber rearrangement under load. As expected, it has been deduced that this process is closely related to the healthy or pathological state of the tissue under analysis.

CHAPTER 4

Penetration capability of near infrared Laguerre-Gaussian beams through highly scattering media

4.1 Introduction

Optical imaging techniques have been investigated and applied in biomedical field since the 17th century, for both *in-vitro* characterization of biological tissues and *in-vivo* imaging, with the main aim of assisting the diagnoses of diseases. An optical imaging technique that recently is being largely adopted in clinical use through commercial systems, is the optical coherence tomography (OCT). OCT was conceived at the beginning of the nineties when the first *in-vivo* two-dimensional imaging demonstrations have been carried out. In particular, it was at first used for *in-vivo* imaging of human eye retinal structures and, after a few years, for the first endoscopic imaging of both the gastrointestinal and respiratory tracts of rabbits [112,113]. Later, in the 2000s, OCT has definitely spread and successfully applied in the cardiovascular field too, where emission wavelength in the 1.3 μm range is employed, for diagnosis of various diseases (e.g. atherosclerosis and vessel wall degradation in ascending thoracic aorta aneurysm) and guidance of semi-invasive interventional procedures (e.g. angioplasty and stenting) [34, 114]. To date, OCT-based 3D imaging is widespread in clinical use thanks to its improved performance in terms of axial and transversal resolution with respect to other conventional 3D-imaging modalities such as magnetic resonance imaging, x-ray and ultrasounds. Indeed, these latter methods generate images of the tissue structure with millimeter or at most sub-millimeter resolution against the more efficient sub-micrometer scale axial resolution and micrometer scale (10-15 μm) lateral one of OCT images [21]. In turbid media (e.g. biological tissues), OCT can image depths up to

1-2.5 mm and greater depths can even be achieved in transparent media. The optical instrumentation typically consists of a broadband and low-coherence light source, a Michelson interferometer, optical fiber, bulk optics and optical detectors [21, 22]. The typical spatial intensity distribution of the optical beam employed in conventional OCT systems consists in a Gaussian (G) shape. When light propagates through turbid media, it experiences high scattering and absorption. These physical phenomena limit the penetration depth to several hundreds of micrometers. Recently, the use of Laguerre-Gaussian (LG) vortex beams has been largely investigated in several fields such as oceanic turbulence [115], nonlinear optics [116], and mode sorting performance [117], through both numerical and experimental analyses. Therefore, the interest in studying the propagation of LG beams in both free space and highly scattering media has grown up over the last few years. In particular, it was recently demonstrated that at the same power, LG vortex beams based on Orbital Angular Momentum (OAM) of light have the capacity of penetrating deeper into turbid media with respect to conventional G beams [118, 119].
The aim of this chapter is to highlight the potential of LG vortex beams in turbid media, including blood, in the 1.3 μm wavelength range, that is the one typically used in cardiovascular and, more in general, endoscopic OCT applications. The benefits of employing LG light beams with respect to conventional G beams will be discussed and experimentally demonstrated by transmittance measurements into specific water suspensions. A higher penetration capability will be verified and quantified as it has been previously done in the red range (i.e. 633 nm) [118]. Then, reflection measurements will be performed on samples of human blood for the first time. From both transmission and reflection measurements, a higher transmittance/lower backscattering can be observed by increasing the OAM order of the light beam.

4.2 Theoretical background

4.2.1 Light transmission through turbid media

Biological tissues can be considered highly scattering media (i.e. turbid media) made up of molecules, cells, fibres and layers of different size that can range from nonometer to millimeter scales. The scattering phenomena due to such complex structures limits the penetration depth of the actual optical imaging devices. Therefore, the successful development of optical imaging techniques depends on the dealing with the problem of light scattering which is the main cause of image blurring.
Typically, light experiences scattering and absorption while propagating through a biological tissues and the degree of scattering and adsorption depend both on the wavelength of the beam and the optical properties of the tissue constituents. Indeed, it is crucial to understand how the main characteristics of the beam (i.e. intensity, coherence and polarization) changes as it is scattered and absorbed while travelling into the tissue. Absorption phenomena typically result from transition of electrons within energy levels of the atoms of the tissue. While scattering takes place when the tissue structure is characterized by refractive index mismatches, and strongly increases as the wavelength of the light beam becomes comparable to the size of the scattering elements. Given a light pulse traversing a turbid medium, the corresponding scattered pulse is broader and comprises three main components [120]:

- Ballistic: the photons belonging to this component (i.e. ballistic photons) propagate along the direction of the incoming beam traversing the shortest path, preserve most of the initial characteristics of the beam and, thus, carry the maximum information for the building of a direct image of the medium. They are also called coherently forward scattered photons.
- Diffusive: the diffusive or multiple-scattered photons traverse long paths within the medium, losing many of their original characteristics, and scatter later in all directions.
- Snake: this component is characterized by photons which scatter slightly in the forward direction, preserving significant initial properties of the incident light and giving relevant information about the medium. They are called "*snake*" because their trajectory resembles a wiggling snake.

The broader width of the scattered light pulse with respect to the initial one is due to the different transition times that the photons spend in traversing the medium. Typically, diffusive photons arrive first, followed by the snake and diffusive ones. The relative intensities of each of these light components depend on the wavelength and the characteristics of the medium. For instance, in biomedical intravascular applications, the infrared region is used as within such spectral range, the absorption is smaller and scattering is lower inside the medium, with respect to the visible range [120].
The most important parameters of a turbid medium required to develop advanced techniques for optical imaging are *i)* the absorption length (l_a) defined as the mean distance travelled by a photon before being absorbed, *ii)* the scattering mean free path (l_s) defined as the mean distance between consecutive scattering events of a photon, *iii)* the transport mean free path (l_t) defined as the distance in which the direction of a propagating photon is fully randomized after several scattering events, and *iv)* the anisotropy factor g which defines the spatial anisotropy of the scattering within the medium. The absorption and scattering lengths are intrinsic properties of the constituents of the analysed medium and are related to the absorption (μ_a) and scattering (μ_s) coefficients respectively, through the following formulas:

$$l_a = \mu_a^{-1} \tag{4.1}$$

$$l_s = \mu_s^{-1} \tag{4.2}$$

In the regime of low particle densities, the absorption coefficients, as well as l_s and l_a according to (4.1) and (4.2), depend on the particle size and concentration within the turbid medium. Such dependence is defined by the following formula:

$$l_s = \mu_s^{-1} = (N\sigma_s)^{-1} \tag{4.3}$$

$$l_a = \mu_a^{-1} = (N\sigma_a)^{-1} \tag{4.4}$$

where N is the volume concentration of the particles and, σ_s and σ_a are the scattering and absorption cross-sections respectively. The anisotropy factor (g) is approximated to the mean cosine of the scattering angle (θ), $g =< \cos\theta >$. The parameters of the medium can be computed by exploiting the Mie scattering theory. In particular, it has been demonstrated that the anisotropy factor of a medium strongly depends on the wavelength for particle sizes smaller than 1 μm. Regarding the scattering and transport mean free path coefficients, due to their dependence on the wavelength, they are

approximately equal for particle sizes smaller than 0.2 μm and start differing between each other for larger particle diameters [120, 121].

4.2.2 Orbital Angular Momentum of light and Laguerre-Gaussian beams

The OAM of light is a vector quantity which expresses the amount of dynamical rotation of the electromagnetic field of light. Indeed, a light beam can be rotating (or *"spinning"* or *"twisting"*) around its own axis. Typically, OAM of light is the component of angular momentum of a light beam which depends on the field spatial distribution, and not on the polarization state of the beam. An OAM of light can be defined as *i)* "*internal*" if it is origin-independent and can be associated with an helical wavefront or, *ii)* "*external*" if it is origin-dependent and can be obtained through the cross product of the light beam position and its total linear momentum. In this work, "*internal*" OAM of light only is treated.
A LG beam is an example of OAM of light. Referring to the formulation in [122], the complex electric field amplitude for a generic LG beam can be written as following:

$$\begin{aligned} E(r,\Phi,z) = E_0 exp\left[\frac{-ikr^2z}{2\left(z_R^2+z^2\right)}\right] exp\left[\frac{-r^2}{w^2}\right] \\ \times exp\left[-i(2p+L+1)\arctan\left(\frac{z}{z_R}\right)\right] \\ \times exp[-iL\Phi](-1)^p\left(\frac{r\sqrt{2}}{w}\right)^L L_p^L\left(\frac{2r^2}{w^2}\right) \end{aligned} \tag{4.5}$$

where *r* is the radial distance from the centre axis of the beam, *z* is the axial distance from the narrowest point of the beam, *i* is the imaginary unit, *k* is the wavenumber, *w* is the beam width at position *z*, z_R is the Rayleigh range, L_p^L are the generalized Laguerre polynomials, *p* is the radial index (i.e. $p \geq 0$), *L* is the azimuthal index known as the helical phase winding number or topological charge (hereafter also referred to as OAM order), which can be zero or an integer value. When $p = 0$ and $L = 0$, the exponential term $exp(-iL\Phi)$ which defines a vortex phase, is unitary and the equation defines a G beam. When $L > 0$, the term $exp(-iL\Phi)$ gives rise to the complex electrical field with a vortex phase, and higher-order transverse beams (i.e. LG beams) are defined.
Therefore, the change of the azimuthal index brings substantial morphological changes to the light beam, as clearly visible in Figure 4.1. In the figure, it can be seen that by changing the topological charge from zero to an integer value higher or smaller than zero through the application of a determined phase mask to the original Gaussian beam, it is possible to generate different twisted wavefronts, each one associated to a certain beam profile. For instance, the main characteristics that distinguish a LG beam from a conventional G beam are listed below and clearly shown in Figure 4.1:

- the vortex phase $exp(-iL\Phi)$;
- the helical and twisted wavefronts;
- the donut intensity shape;
- the dependence of the beam size to the OAM order through the law r^L, so that the radius of the light crown tends to enlarge exponentially with the topological

charge. In Figure 4.2, it can be appreciated how the radial distance of the field amplitude peak increases when increasing L.

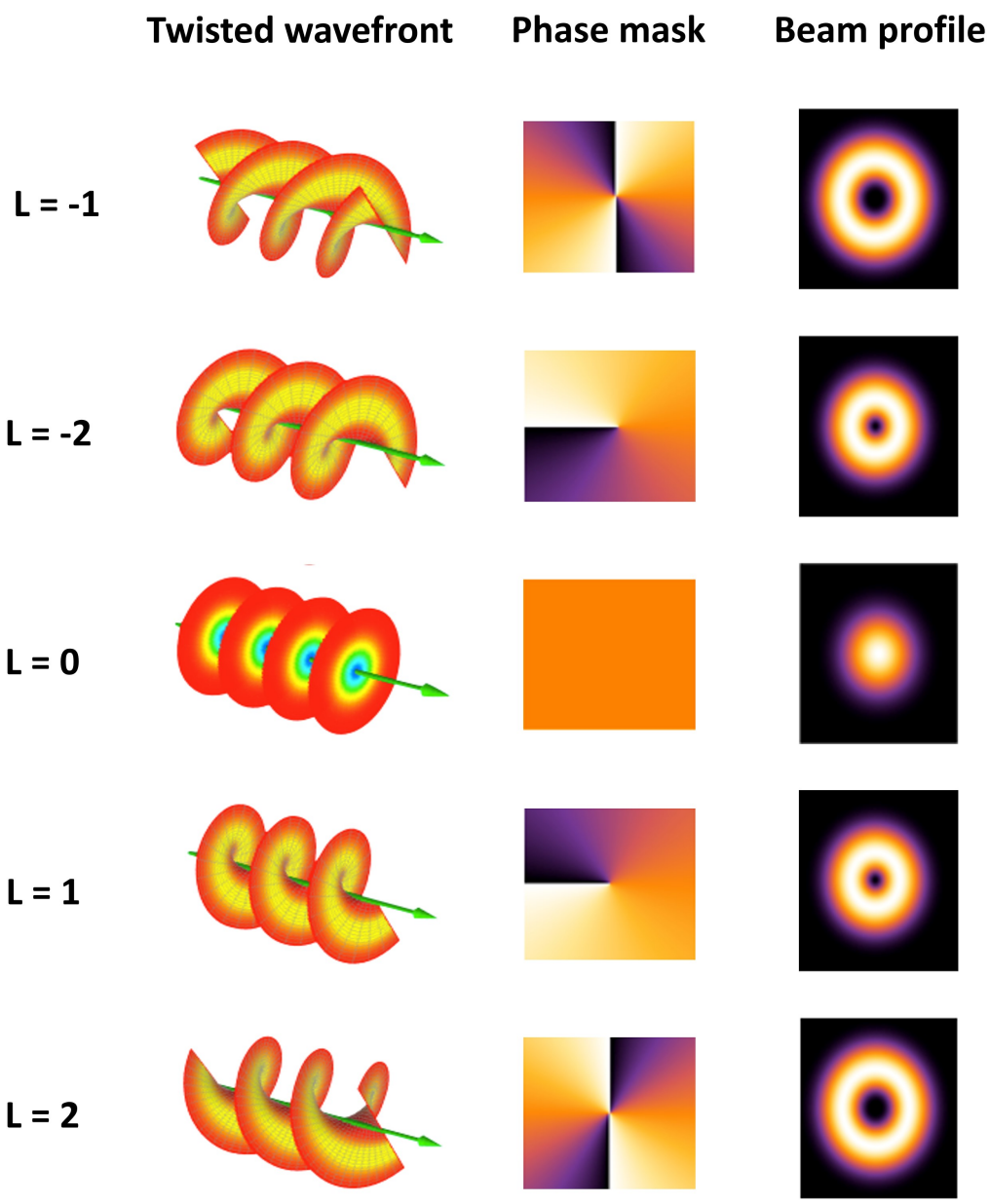

Figure 4.1: *Examples of LG gaussian beams by varying the topological charge and keeping the radial index constant (i.e. $p = 0$). For each beam, the corresponding twisted wavefront and phase mask are shown.*

Some works revealed that the variation of the OAM order leads not only to a drastic morphological change of the beam, but also to different behaviour in propagating into highly scattering turbid media. It was predicted an increase of the transmittance in turbid media by increasing the OAM order of the light beam, and through experimental tests at a wavelength range of 633 nm, the effect was observed with synthetic turbid media emulating the highly scattering properties of biological fluids [118, 119, 123,

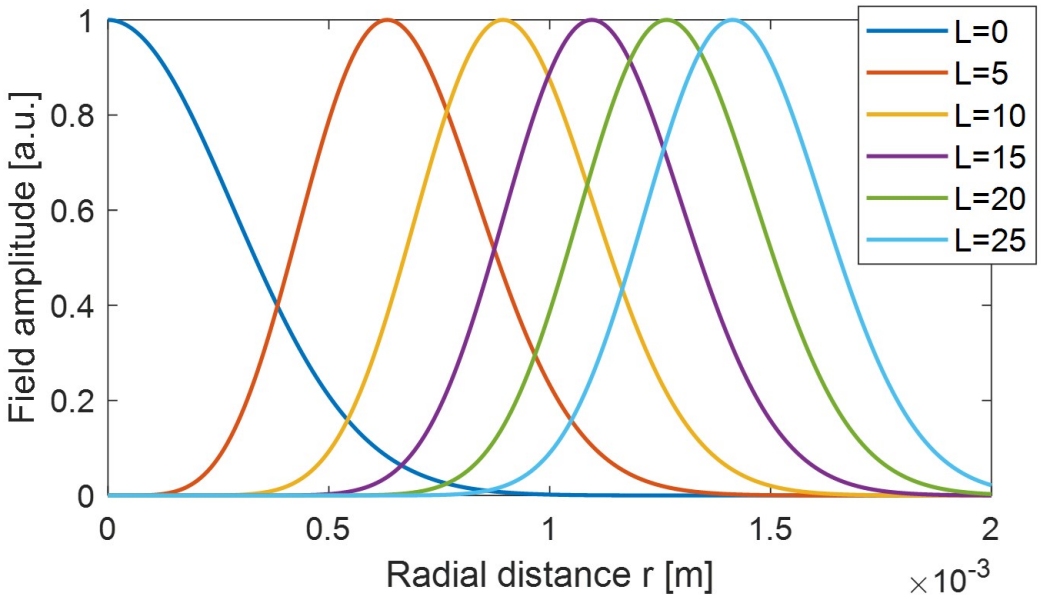

Figure 4.2: *Field amplitude from Equation* (4.6) *versus radial distance r, for the values of L considered in the reported experiments.*

124].

4.3 Transmission measurements

4.3.1 Description of the experimental setup

From the schematic in Figure 4.3, the transmission measurement setup is shown, emphasizing three main blocks that are *i)* beam generation, *ii)* beam splitting into reference beam and beam transmitted to the sample, *iii)* beam acquisition and post-processing.
A light source operating at a wavelength of 1.3 μm is connected to a collimator that generates and propagates in free space a Gaussian light beam. Through the use of a fiber-based polarization controller and a free-space polarizer, a linear polarization state with arbitrary orientation has been obtained. The beam is then directed to a polarization-dependent Spatial Light Modulator (SLM), i.e. PLUTO-2-NIRO-023 by Holoeye, that consists of different diffraction patterns and works in reflection. Through a dedicated software the diffraction pattern can be changed and consequently the SLM properly tailors the spatial phase of the incident light beam (on the plane perpendicular to the propagation direction) so as to generate different OAM orders. The generated LG beam is finally divided by a beam splitter into two separate beams (i.e. sample and reference beams). The reference beam and the one transmitted through the sample are acquired by two separate infrared cameras (XS-4440, Xenics), so as to quantify and therefore take into account the small variation of incident power when varying L and for different types of sample. The beam size before hitting the sample is about 1 mm.
The highly scattering turbid media used as samples for the experimental transmission tests are three particulate suspensions of 0.1 μm polystyrene beads diluted in water (by Sigma-Aldrich) at different concentration percentages (i.e. 1%, 5% and 10%) with a

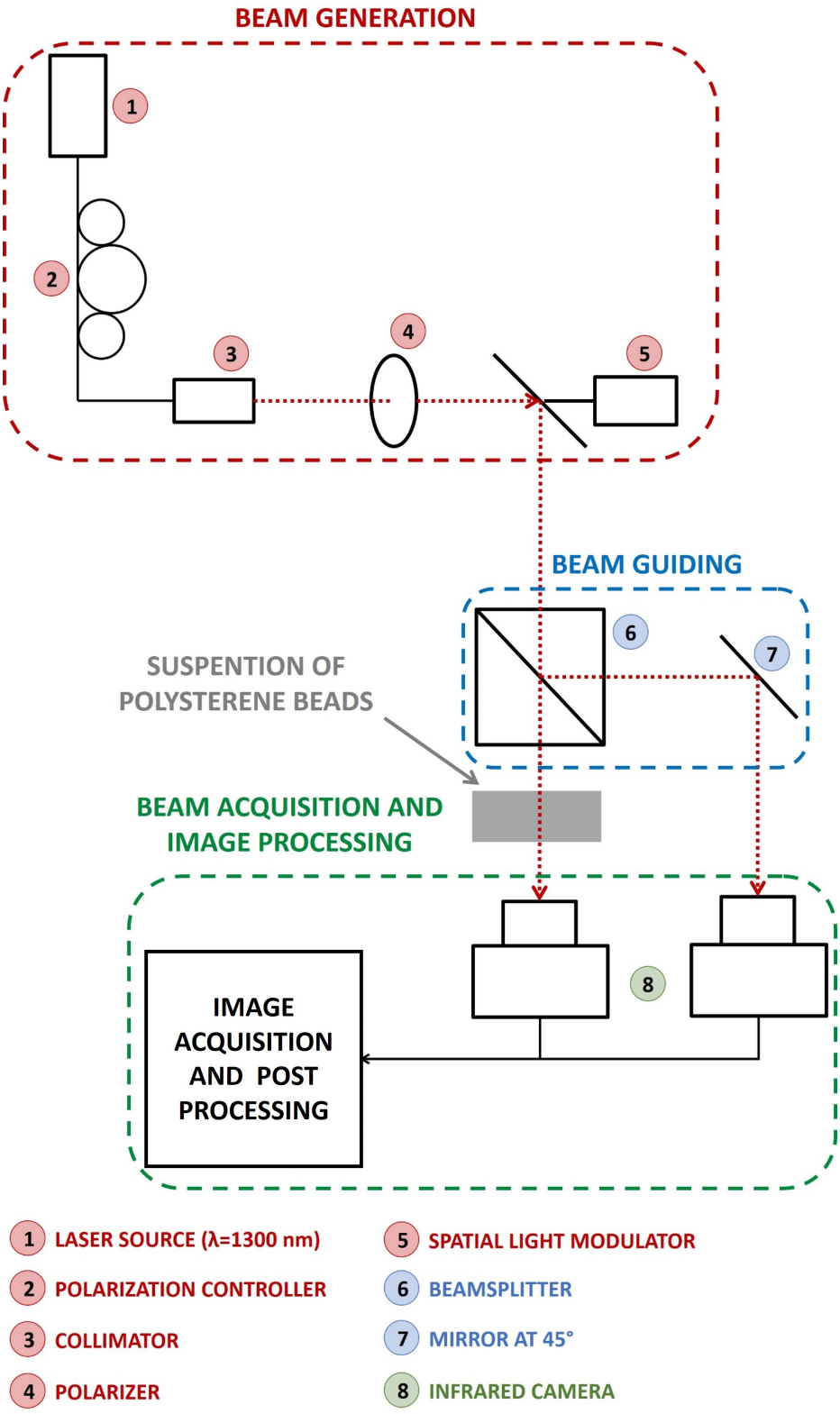

Figure 4.3: *Setup to perform the transmission measurements.*

sample thickness of 10 mm. For each suspension, six different beams having a different OAM order each, have been tested. They are shown in Figure 4.4 and consist in a G beam ($L = 0$) and five higher-order LG vortex beams ($L = 5, 10, 15, 20, 25$). All the generated beams have radial index equals to zero ($p = 0$).

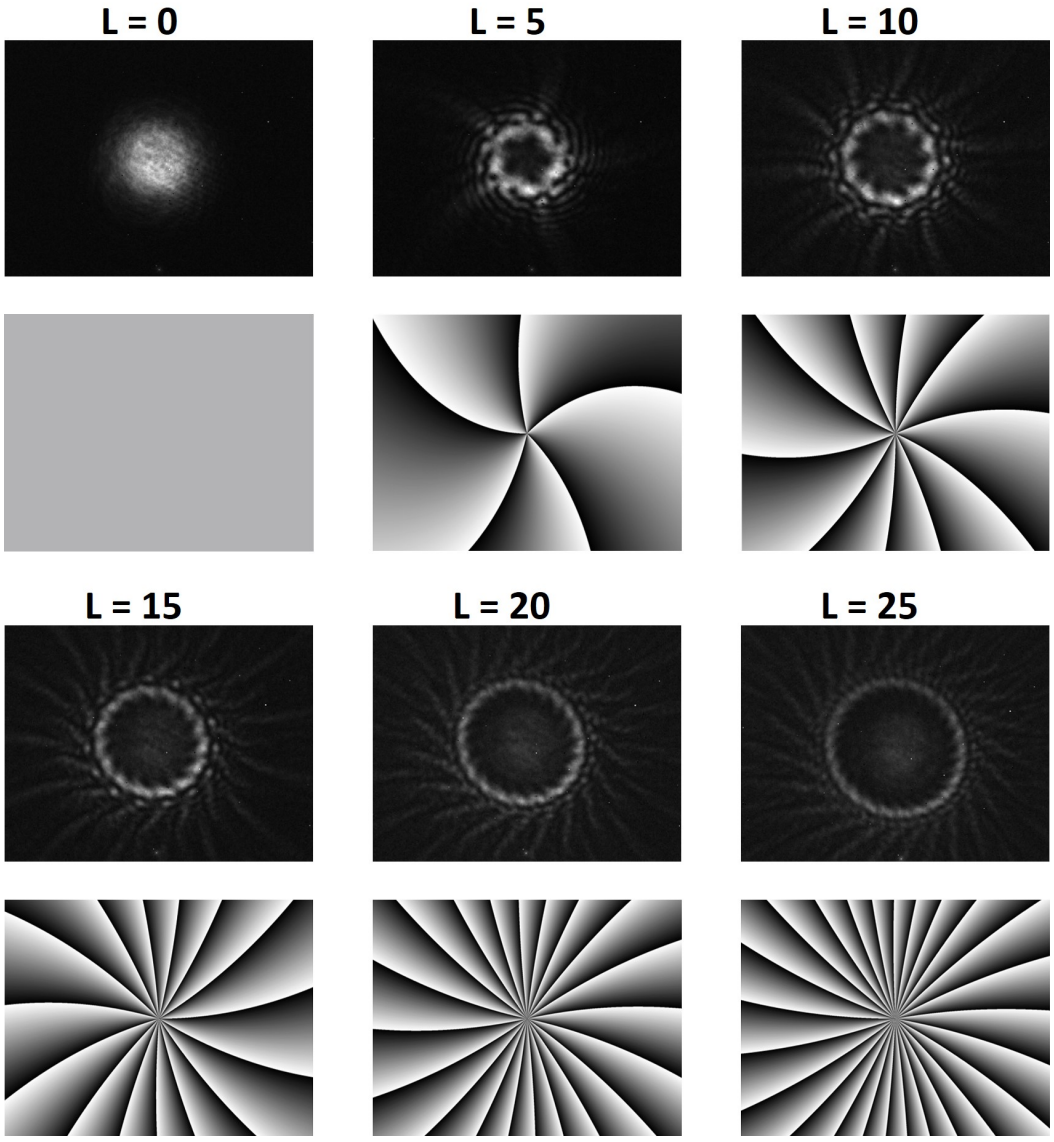

Figure 4.4: *Infrared images of the six tested optical beams with each corresponding phase mask to be charged on the SLM. The azimuthal index or OAM order (L) is varying while keeping the radial index constant ($p = 0$)*

The typical "doughnut"-shaped intensity includes spiral rays. These are due to the interference among the generated OAM beam and the co-propagating residual Gaussian beam. This residual Gaussian beam is due to the not perfect linear polarization of the Gaussian beam incident on the SLM. The light portion that possesses a polarization orthogonal with respect to the SLM principal axes does not undergo the SLM-induced phase modulation, maintaining the Gaussian intensity profile. Another system non-ideality is represented by the dimension of the SLM pixels. When the OAM order

increases, i.e. the phase variation per angle on the SLM is faster, the quality of the generated OAM beam decreases. A broad range of L values have been used in order to determine to what extent the OAM topological charge is relevant to the penetration strength. A step of $\Delta L = 5$ has been chosen in order to reduce the total number of measurements. The maximum topological charge ($L = 25$) was determined by the maximum diameter of the CCD camera. Higher topological charges would not be entirely collected by the CCD.
The concentrations of polystyrene beads in water have been chosen to limit the total attenuation in transmission, such that a detected power above the system sensitivity has been achieved for all the considered cases. Indeed, the expected theoretical power transmitted through the suspension (I_t) has been obtained through the law of Lambert-Beer:

$$I_t = I_0 exp(-(\mu_s + \mu_a)x) \tag{4.6}$$

where I_0 is the input power, μ_a is the absorption coefficient of water in the 1.3 μm range (i.e. 7.1478 cm^{-1}), μ_s is the scattering coefficient of the suspension given by $\mu_s = 1/l_s$ (where l_s is the scattering mean free path coefficient of the suspension, which has been calculated through the Mie scattering theory) and x is the optical path traversed by the beam. Furthermore, through the calculation of l_s operation in the diffusive region has been verified. Indeed, according to previous studies [118, 125], the OAM effect in turbid media is pronounced in such region and, in particular, the diffusive region occurs when the scattering mean free path is smaller than the thickness of the investigated medium (z) (i.e. $\frac{z}{l_s} > 10$ for a particle diameter of 0.1 μm). In Table 4.1, the values of the scattering mean free path related to each tested suspension are reported.

Table 4.1: *Values of l_s and z/l_s ratio for each tested bead suspension.*

Particle concentration (%)	l_s (mm)	z/l_s
1	0.0965	103.63
5	0.0194	515.46
10	0.0097	1030.93

A proper post-processing is implemented through a Matlab script, based on the images acquired by the two infrared cameras. Based on a preliminary calibration process which compensates for nonlinear camera intensity, a lookup table was first created for mapping the integral of the pixels' intensity to the corresponding incident optical power, also verifying the non-saturation regime of each camera. Each acquired image is properly converted to a power level in dBm. The script also compensates for possible reference power variations, through the acquired reference images at the second camera. Moreover, eventual camera saturation is avoided by applying proper attenuation at the input of the camera used on the reference arm. Finally, the received power is computed for each image by averaging the pixel values and is plotted as a function of the OAM order (L) for each suspension.

4.3.2 Results and discussion

The plot of the received power as function of OAM order is shown in Figure 4.5. For a Gaussian beam shape, it resulted that the received power decrease is quite small while increasing the beads concentration in water (≈ 1.5 dB from 1% to 5%, ≈ 1.2 dB from 5% to 10%). From the behavior of the curves, it can be seen that the power received by the infrared Camera increases while increasing the OAM order of the beam. These

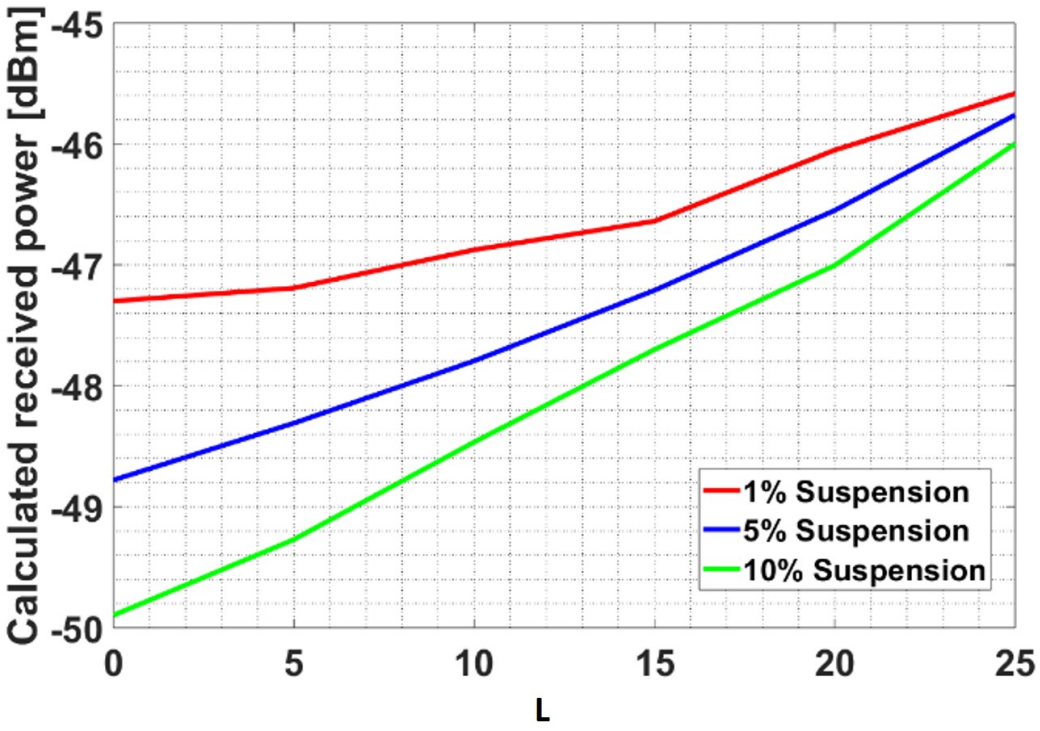

Figure 4.5: *Received power versus OAM mode for 1%, 5% and 10% suspension concentration.*

results confirm that also in the infrared range (e.g. 1.3 μm) higher-order LG vortex beams are able to penetrate deeper in highly scattering turbid media by increasing the OAM order, as it has been previously demonstrated in the visible red range (i.e. 633 nm). The received power in case of G beam decreases by increasing the suspension concentration, because of the higher total attenuation. As the total attenuation is given by water absorption and particulate scattering, such decrease rate is not proportional to the particle concentration increase rate. However, the curve slope becomes steeper by increasing the beads concentration. Indeed, the total increase of the received power from the G beam case to the case L = 25 is 1.72 dB, 3 dB and 3.9 dB for 1%, 5% and 10% dilution percentage respectively. This means that the capacity of penetrating deeper in turbid media increases by increasing the particle concentration. Since, as claimed in [124, 126], LG light beams characterized by higher L leads to less scattering from each incident particle, the higher the amount of interacting particles, the higher the intensity increase of transmitted power through the medium for a given change of the value of the OAM order.

4.4 Reflection measurements

4.4.1 Description of the experimental setup

Regarding the measurements performed in reflection on samples of human blood, the scheme of the involved setup is represented in Figure 4.6. It differs from the transmission setup only for the placement of the sample. At the beam splitter, the beam is divided into sample and reference beams. Part of the sample beam is then backscattered by the blood sample and acquired by one of the infrared cameras. The blood sample is placed in a specific dark container such that the reflection artifacts at its lateral and bottom surfaces are negligible. The tested beams are the ones already listed for the transmission tests and the only parameter that has been changed is the thickness of the blood sample (i.e. 0.2, 0.3, 0.4, 0.5, 0.6, 0.7, 0.8, 0.9 and 1 cm).

4.4.2 Results and discussion

Similarly to what has been done in the previous set of measurements, a proper script derives the plots of the received power as a function of the OAM order (L), in this case for each sample thickness. The results from the reflection measurements on human blood samples at different thicknesses are shown in Figure 4.7.
Clearly, the trend of the curves is inverted compared to the one resulted from the transmission measurements. Indeed, the received power decreases while increasing the OAM order. Moreover, the acquired power increases while increasing the sample thickness. This happens as the number of scattering events increases while increasing the sample thickness. As a consequence, the backscattered power increases too. In addition, for thicknesses higher than 0.5 cm the acquired backscattered power tends to saturate (at about -30.5 dBm for G beam). This behavior is justified by the fact that the fraction of light beam penetrating deeper is negligible, due to the high total attenuation through blood, in forward and backward direction. However, the power decrease from the case L = 0 to L = 25 for each considered thickness is not higher than 1.3 dB. This is due to the reflection artifact occurring at the surface of the sample which could be deleted by making a coherent measurement, with the possibility to discriminate the power backscattered from a specific depth. Indeed, the calculated reflectance at the interface between air and blood is about 20% of the input power. Therefore, such a constant reflected amount of power partly obscures the measured power related to the backscattering events due to the particulate portion of the blood.
These results confirm the initial hypothesis that the use of LG vortex beams could improve the performance of OCT systems in clinical diagnosis with respect to the use of conventional G beams, allowing a deeper penetration of the optical light beams in biological tissues, in particular in the field of cardiovascular imaging (i.e. IVOCT applications) where 1.3 μmm–wavelength range is used and blood severely affects the performance. Indeed, for OCT the choice of the employed wavelength region strictly depends on the application. In general, for highly scattering tissues longer wavelengths are recommended, but on the other hand water absorption decreases when decreasing the wavelength in the (near) infrared regime. From another perspective, longer wavelengths might guarantee single-mode transmission through standard optical fiber, necessary to reach remote tissues through optical endoscopes, and the massive exploita-

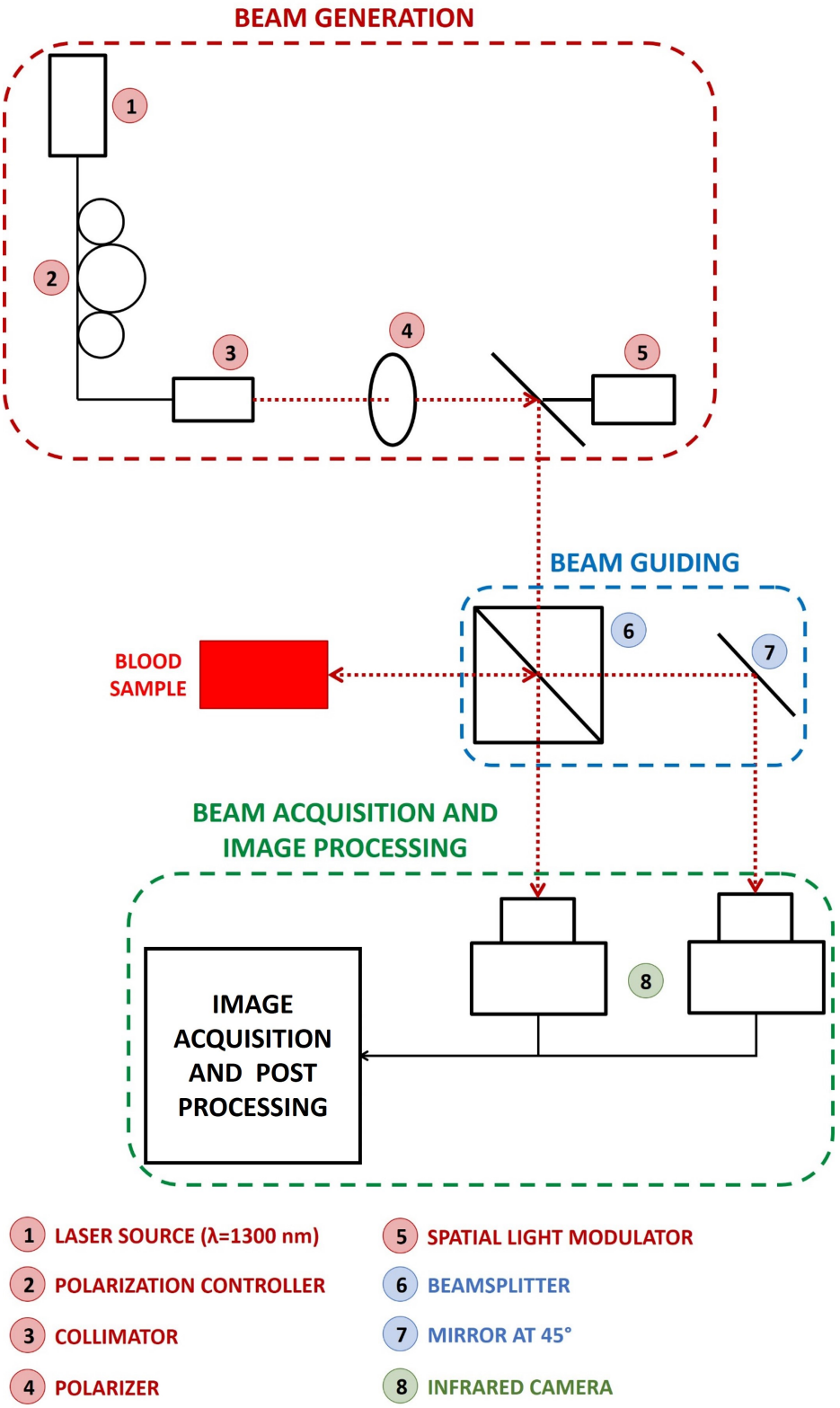

Figure 4.6: *Setup to perform the reflection measurements.*

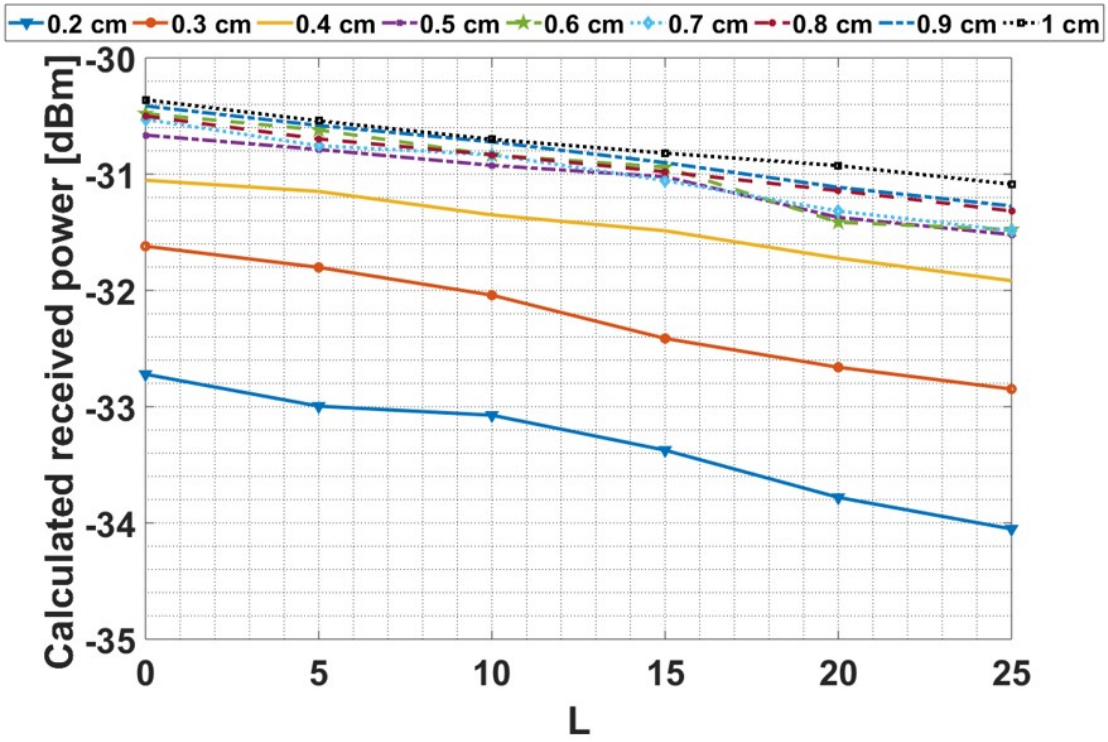

Figure 4.7: *Received power as a function of OAM mode for different blood sample thicknesses (in reflection).*

tion in telecom of long wavelengths makes those optical sources more mature, reliable and high-performance. In case of testing a suspension, from [118] can be inferred that the observed higher penetration capability for higher L values is more pronounced for smaller particles with respect to wavelength. This could potentially mean that for longer wavelengths an enhanced effect could also be obtained. However, the trade-off with water absorption coefficient trend versus wavelength would have to be considered, to quantify the actual impact on the absolute received power level by changing the employed wavelength. A physical or theoretical explanation of the observed higher penetration capability for higher OAM orders, is still missing. An analysis based on the self-healing properties of those modes, recently confirmed by other publications [127], could be the way.

4.5 Conclusive remarks

In summary, in this chapter it is experimentally demonstrated the higher capacity of LG vortex beams of penetrating highly scattering turbid media (i.e. water suspensions and blood) with respect to conventional G beams. In particular, an increase of OAM order implies the increase of this capacity. Such phenomenon is demonstrated in the 1.3 μm–wavelength range, typically used for *in-vivo* cardiovascular IVOCT procedures, by performing transmission and reflection measurements. Therefore, the adoption of LG vortex beams in IVOCT systems could have the potential of increasing the penetration depth, as it mitigates the effect of scattering experienced by the light beam traversing the biological fluids, which is one of the issues limiting the commercial IVOCT systems,

especially in cardiovascular applications. From a clinical point of view, that could potentially lead to unprecedented diagnoses of diseases and to the use of OCT in novel *in-vitro* and *in-vivo* biomedical scenarios.

CHAPTER 5

Development of an ultra-high speed A-scan system for Optical Coherence Tomography applications based on real-time optical spectrum Fourier transformation

5.1 Introduction

With the wording «*Optical reflectometry*» we refer to a powerful set of techniques which are based on the acquisition of reflected optical waves to get information from the medium or optical component under investigation. They are characterized by high spatial resolutions (i.e. typically submillimeter resolution) and, for this main reason, they are exploited in a broad range of applications [128] such as material and component diagnosis, characterization of optical components and modules, laser ranging and metrology, and to implement 3D imaging for biomedical applications [129–132]. In biomedical field, one of the most powerful imaging techniques based on optical reflectometry is the Optical Coherence Tomography (OCT) which allows high performance in terms of spatial resolution and speed. For this reason, OCT imaging has rapidly spread out in both clinical and biomedical research environments. Indeed, OCT systems can achieve very high axial and lateral resolutions [133], i.e. up to 1 μm and up to 3 μm respectively. Nowadays, OCT imaging is employed in several clinical scenarios such as ophthalmology [134, 135], angiography [136] and catheter-based applications which include visualization of the gastrointestinal tract [137] and the cardiovascular system [138, 139]. Typically, the wavelength adopted for OCT light sources lies within the infrared region (i.e. between 800 and 1300 nm). This is because, within this spectral range, water absorption is minimized, while the portion of signal which is scattered from biological tissues is maximized. In particular, a wavelength of 1300 nm is com-

monly used for intravascular OCT (IVOCT) applications because the blood absorption spectrum exhibits a local minimum at this wavelength value. The high spatial resolution of IVOCT systems is achieved thanks to the broad bandwidth of the generated optical signal which guarantees much higher resolutions than other corresponding techniques that are generally used in clinical scenarios (e.g. conventional angiography and intravascular ultrasound imaging) [34, 140]. However, the main issues of conventional OCT axial (A)-scan systems include the need of mechanical movement of the reference mirror e.g. in Time-Domain OCT (TD-OCT), and time-consuming post-processing of digital data, e.g. in Spectral Domain OCT (SD-OCT) and Swept Source OCT (SS-OCT). These operations reduce the speed of the signal acquisition process and update rate of the imaging operation. Typically, the acquisition speed plays a crucial role in medical imaging. For instance, in ophtalmology the eye movements can be a source of noise during the measurements [141], while in intravascular imaging applications, high acquisition times can cause cardiac complications such as arrhythmia [34]. The increase of the speed in performing signal acquisition and processing, could solve the above mentioned problems. Indeed, in ophtalmology, a sufficiently high system speed could make eye movements negligible, while, in intravascular imaging, could allow a real-time monitoring of the entire 3D arterial wall structure without the risk of complications arising. This last achievement would have an unprecedented impact in cardiosurgery because it could allow the check of the correct stent placement after a surgical intervention through the real-time monitoring of the artery wall elasticity during heartbeat [140, 142, 143]. In general, even if OCT techniques in the frequency domain (i.e. SD-OCT and SS-OCT) do not require mechanical movements such as TD-OCT techniques and so, they results faster, the signal acquisition speed is anyway limited by digital post-processing (i.e. Fourier transformation in the digital domain) for FD-OCT systems or by the wavelength scan for SS-OCT systems [144, 145].
The aim of this work is to design, calibrate and experimentally develop a photonics-based A-scan circuit for IVOCT systems (i.e. 1300 nm wavelength range) able to perform both acquisition and processing of the optical reflected signals, coming from the target tissue, in the analog domain without any scanning or post-processing steps as it is required in TD-OCT or SD-OCT imaging. This innovative A-scan system is based on a simple fiber-optics configuration that performs the real-time optical spectrum Fourier transformation (RT-OSFT) [146–148]. This is an optical approach that enables the real-time implementation of the target Fourier transformation of the acquired signals in the optical domain at MHz update rates, much higher than conventional OCT update rates (i.e. typically below 100 kHz) [149, 150].

5.2 Theoretical background: conventional A-scan OCT systems

5.2.1 TD-OCT approach

TD-OCT A-scan system exploits the interference between the reflected signal coming from the reference optical arm, where a moving mirror is placed, and the backscattered signal coming from the sample under investigation. This enables the detection of the position (and entity) of the sample's inner discontinuities were refractive index changes are present, that produce reflections of the induced radiation. The scheme of a typical TD-OCT A-scan system is showed in Figure 5.1. The optical source generates a low

coherence radiation, i.e. a broadband source. A Michelson interferometer splits such radiation in two parts. One is directed to a moving mirror which is the reference arm of the interferometer. While the other one is directed to the sample (i.e. sample arm). In the reference arm the mirror entirely reflects the optical beam, while in the sample arm the beam hits the sample. The beam portion which comes back from the sample to the interferometer is characterized by the back-scattered signals generated at the different sample discontinuity interfaces. Then, the radiations coming from the two interferometer's arms, interfere and the resulting wave is directed to a photoreceiver. The position of the sample discontinuities can be detected thanks to this working principle and the crucial features are *i)* the translation of the mirror, during the acquisition, along a distance at least equals to the sample thickness, and *ii)* the broad spectrum of the generated signals [151]. In the following section the analytical expression describing the intensity

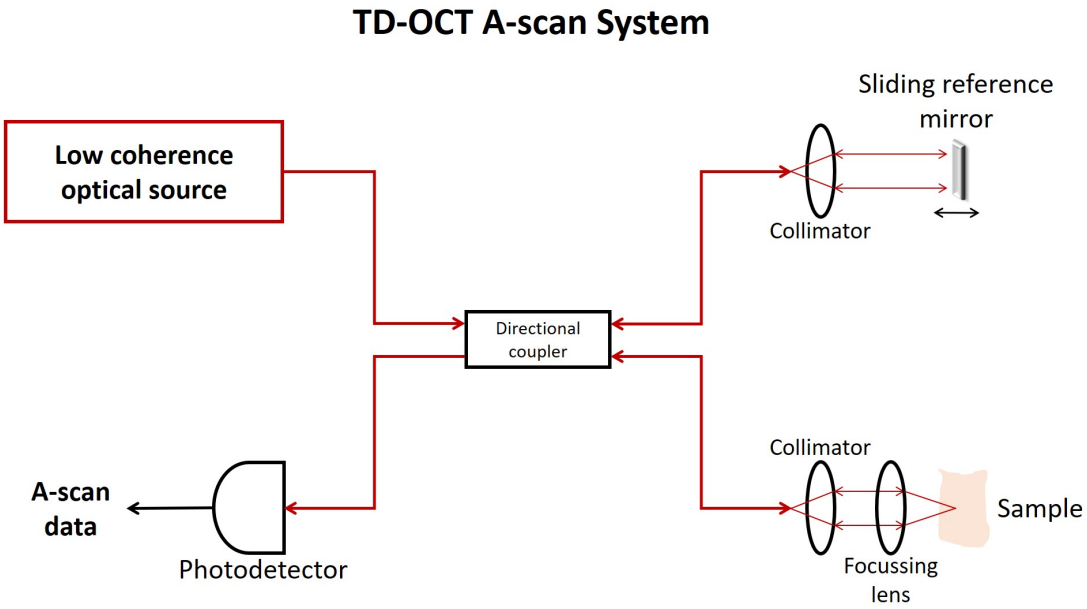

Figure 5.1: *Scheme of a typical TD-OCT A-scan system.*

of the optical wave acquired at the photoreceiver is given together with the reason why the broad spectrum of the generated signal is fundamental for a correct implementation of TD-OCT A-scan [151].
Firstly, it is supposed that the generated optical beam sent to the interferometer is monochromatic and so, a perfect coherent radiation. In this case, the electrical fields of the two beams travelling along the reference ($\vec{E_r}$)and sample arms ($\vec{E_s}$), as a function of the travelled distance ($\vec{r}$) and time (t), are respectively:

$$\vec{E_r}(\vec{r},t) = E_r \times exp[j(2\pi ft + \phi_r(\vec{r}))] \tag{5.1}$$

$$\vec{E_s}(\vec{r},t) = E_s \times exp[j(2\pi ft + \phi_s(\vec{r}))] \tag{5.2}$$

where E_r and E_s are the amplitudes of the electrical fields, j is the imaginary unit, f is the frequency of the monochromatic source and, ϕ_r and ϕ_s are the phases of the reference and sample beams. The dependence of the phase terms on the distance travelled

by the corresponding waves is given by the following formulas:

$$\phi_r(\vec{r}) = \beta_r 2l_r = \frac{2\pi}{\lambda_r} 2l_r \tag{5.3}$$

$$\phi_s(\vec{r}) = \beta_r 2l_s = \frac{2\pi}{\lambda_s} 2l_s \tag{5.4}$$

where β_r and β_s are the propagation constants related to the medium which the radiations travel through in reference and sample arms, λ_r and λ_s are the wavelengths, l_r and l_s are the lengths of reference and sample arms which are multiplied by two because, for each arm, the signal being reflected travels two times the path length. Making the assumptions that the propagation constants and the wavelengths are equal in both the interferometer arms (i.e. $\beta_r = \beta_s = \beta$ and $\lambda_r = \lambda_s = \lambda$), the total electrical field of the beam coming out from the interferometer ($\vec{E_{tot}}$) is the sum of the electrical fields generated by the reference and sample beams:

$$\vec{E_{tot}} = \vec{E_r} + \vec{E_s} \tag{5.5}$$

Therefore, the intensity associated to E_{tot} revealed by the photodetector (I) is determined as following:

$$I \propto \frac{1}{2}[|E_r|^2 + |E_s|^2 + 2E_r E_s cos(\phi_r - \phi_s)] = I_r + I_s + 2\sqrt{I_r I_s} cos\left(2\pi \frac{\Delta l}{\frac{\lambda}{2}}\right) \tag{5.6}$$

where I_r and I_s are the intensities related to the reference and sample signals respectively and, Δl is the difference of the two optical paths traversed by reference and sample beams (i.e. $\Delta l = l_r - l_s$). Thus, a dependence exists between the intensity of the beam acquired by the photodetector and the difference between the two travelled lengths.
As it can be seen from equation (5.6), the interference term has a period of $\frac{\lambda}{2}$. Hence, for a monochromatic source, by translating the mirror, for each step equals to $\frac{\lambda}{2}$, the final signal shows a infinite number of peaks by varying Δl (Figure 5.2a). If the source is characterized by a broad spectrum and so, by several wavelengths, the equation (5.6) is applied to each component. Thus, the components have different periods between each other's and the resulting interference signal goes to zero for most of the values of Δl. In particular, when $\Delta l = 0$ and so, $l_r = l_s$, the signals related to the several chromatic components sum up and the phenomenon of low-coherence interferometry, which is the main working principle of OCT systems, happens (Figure 5.2b).
The intensity acquired by the photodetector, given a broadband source, differs from equation (5.6) (i.e. interference of monochromatic waves) for a factor (γ_{sr}) which represents the degree of coherence between the reflected beams coming from the reference and sample arms:

$$I = I_r + I_s + 2\sqrt{I_r I_s}|\gamma_{sr}|cos\left(2\pi \frac{\Delta l}{\frac{\lambda}{2}}\right) \tag{5.7}$$

λ is now the central wavelength of the broadband source and γ_{sr} is a normalized function, in particular:

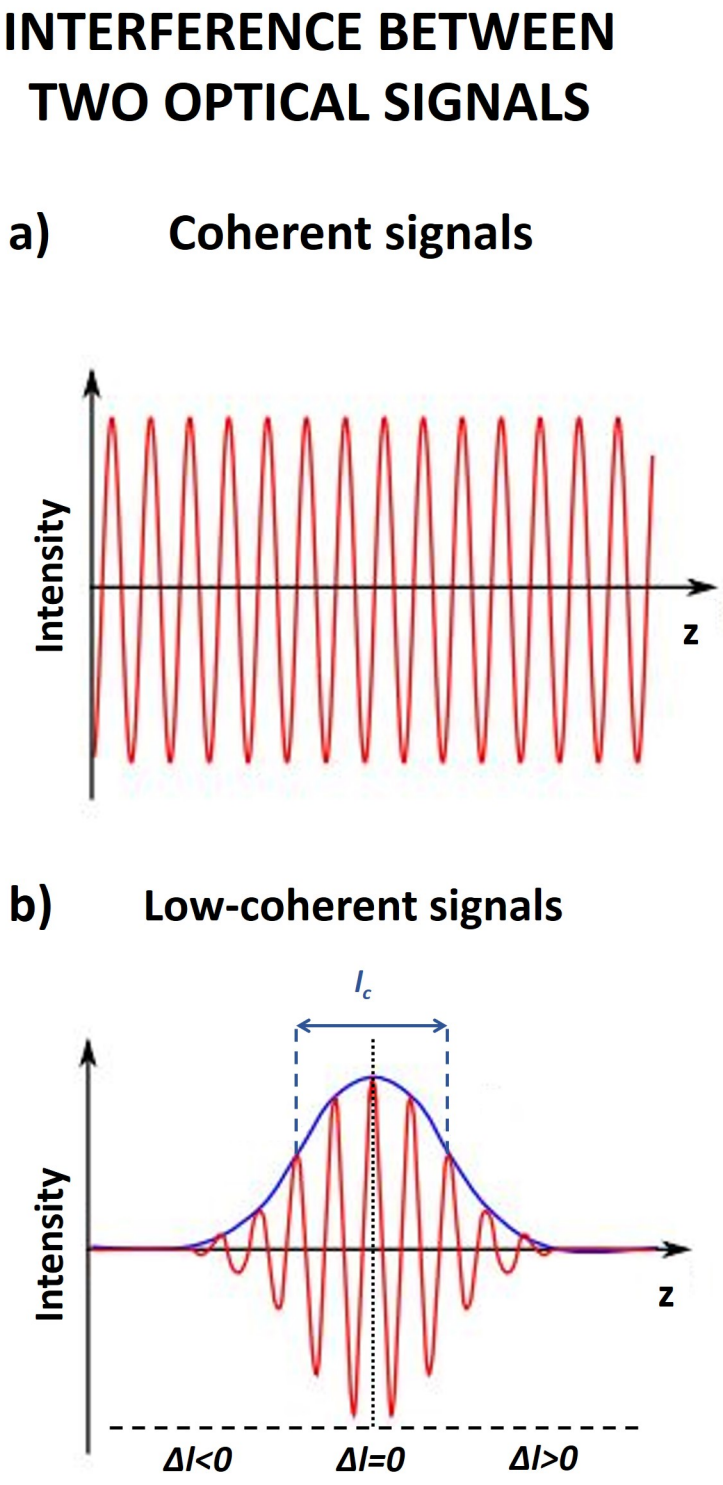

Figure 5.2: *Interference of two optical signals as function of the optical difference path (Δl) for a) coherent and b) low-coherent signals.*

- If $|\gamma_{sr}| = 1$ the reflected waves coming from the sample and reference arms are perfectly correlated and equation (5.7) reduces to equation (5.6). So, the beams can be considered perfectly coherent and the behaviour of the resulting interference signal is as shown in Figure 5.2a.
- If $|\gamma_{sr}| = 0$ the reference and sample beams are uncorrelated and when they interfere, they sum up but the interference term goes to zero.
- If $0 < |\gamma_{sr}| = 0 < 1$ the reference and sample beams are partially correlated, the phenomenon of low coherence interferometry takes place and the interference term is a peak, as shown in Figure 5.2b, whose envelope has a full width at half maximum (FWHM) equals to the coherence length of the optical source (l_c).

The degree of coherence can be expressed also as function of l_c:

$$|\gamma_{sr}| = 1 - \frac{\Delta l}{l_c} \tag{5.8}$$

when $\Delta l < l_c$. If this last inequality is not verified and so, $\Delta l > l_c$, the degree of coherence goes to zero. It means that the interference term can be acquired by the photodetector only when the difference of the distances travelled in each arm of the interferometer is less than the coherence length.
It is important to note that the oscillating interference term (Figure 5.2b) corresponds to the autocorrelation of the electrical field of the source. Indeed, considering that reference mirror and sample are spectrally uniform, the reflected waves coming from the reference and sample arms differ only for the travelled distance:

$$\vec{E_r}(\omega) \approx \vec{E_s}(\omega) \approx \vec{E_{source}}(\omega) \tag{5.9}$$

$$\vec{E_s}(\omega)(l = l_s + \Delta l) \approx \vec{E_r}(\omega)(l = l_r) \tag{5.10}$$

hence, the interference term acquired by the photodetector is proportional to the autocorrelation of the electrical fields generated by the optical source as function of $2\Delta l$:

$$Re[\vec{E_r}(\omega)\vec{E_s^*}(\omega)] \approx Re[\vec{E_{source}}(\omega)\vec{E_{source}^*}(\omega)] \tag{5.11}$$

As consequence, the width of the envelope of the interference term is equal to the source coherence length. Furthermore, for the Wiener-Khinchin theorem, which states that the spectral power density of a signal is the Fourier transformation of its autocorrelation, the width of the interference term and the width of the source radiation are inversely proportional. Thus, the width of the source spectrum plays an important role in the axial resolution of the system. Indeed, the more is the spectral width of the source, the shorter is the coherence length and, consequently, the narrower is the FWHM of the envelope of the interference term. During an A-scan OCT acquisition, the narrower are the envelopes of the interference terms corresponding to each sample interface, the better is the axial resolution.
In general, for optical gaussian sources, the axial resolution of the system is equal to the coherence length of the input spectrum, expressed by the following relationship:

$$l_c = \frac{2ln(2)}{\pi}\frac{\lambda_0^2}{\Delta\lambda} = 0.4413\frac{\lambda_0^2}{\Delta\lambda} \tag{5.12}$$

where λ_0 is the center wavelength of the source spectrum and $\Delta\lambda$ is the FWHM of the input spectral width.

5.2.2 SD-OCT approach

SD-OCT is another approach for OCT A-scan in which the optical signal is treated in the frequency domain. The source is again an optical radiation characterized by a broad spectrum ($\Delta\lambda$) and the reference mirror is kept in a fixed position. In Figure 5.3

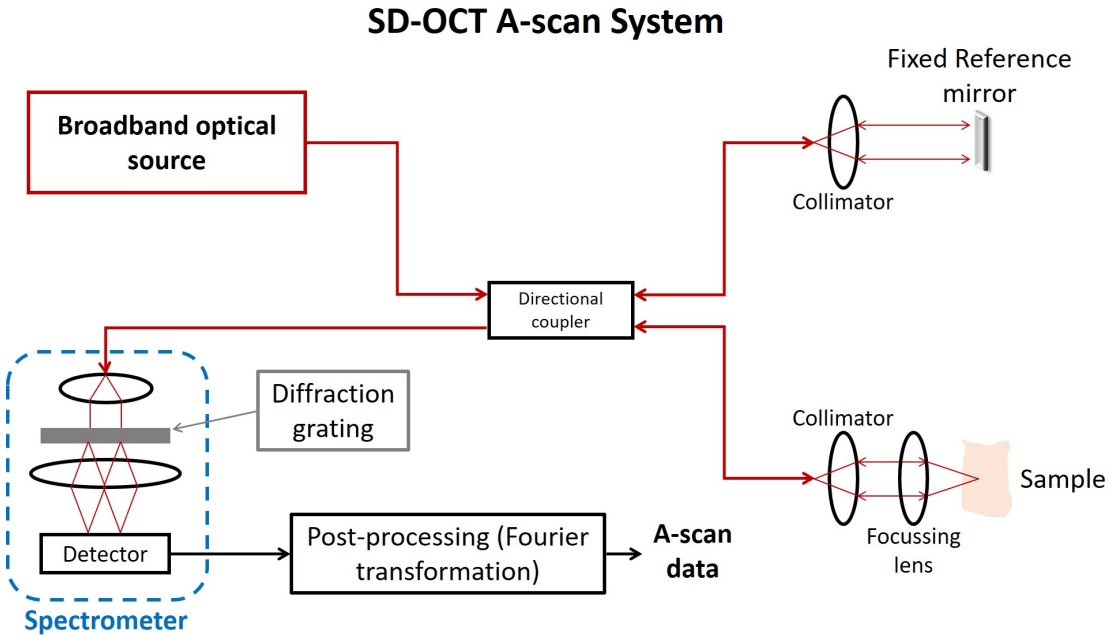

Figure 5.3: *Scheme of a typical SD-OCT A-scan system.*

a scheme of a typical SD-OCT A-scan system is presented. The broadband radiation is split into the reference and sample arm and the two corresponding reflected signals (i.e. one from the reference fixed mirror and the other one from the analysed sample) interfere. The interference signal goes to a spectrometer where a diffraction grating spatially separates the spectral component that are acquired by a detector. As soon as the spectrum of the interference signal is acquired, the Fourier transformation is done in post-processing and the A-scan data in the temporal domain are computed. In this configuration, the reference mirror position is kept fixed because the information is acquired simultaneously for each internal reflection within the sample deleting, in this way, eventual sources of mechanical noise due to mirror translations, and increasing the signal acquisition speed [151].
Analytically [151], supposing that only one reflection occurs within the sample at a certain depth (i.e. $z_0 = l_s - l_r$ so, $\Delta l = |l_s - l_r|$) and the absorption within the sample does not affect the spectrum of the source signal, the intensity of the signal coming out from the interferometer at a certain angular frequency ω, can be written as following:

$$I(\omega) = \left[|a_r|^2 + |a_s|^2 + 2a_r a_s cos\left(\omega\frac{2\Delta l}{c}\right)\right] S(\omega) \tag{5.13}$$

where $|a_r|^2$ and $|a_s|^2$ are the amplitude of the reflected signal coming from the reference and sample arm respectively, $S(\omega)$ is the normalized spectrum of the source signal at the considered angular frequency ω. The signal described by equation (5.30) enters

the spectrometer where all the spectral components are separated. Basically, the acquired intensity is a sinusoidal spectrum whose envelope consists of the source signal spectrum, characterized by two main components, the continuum one (DC) and the oscillating one (AC):

$$I(\omega) = I_{DC}(\omega) + I_{AC}(\omega) \tag{5.14}$$

where:

$$I_{DC}(\omega) = \left(|a_r|^2 + |a_s|^2\right) S(\omega) \tag{5.15}$$

$$I_{AC}(\omega) = \left[2a_r a_s cos\left(\omega \frac{2\Delta l}{c}\right)\right] S(\omega) \tag{5.16}$$

The only term which brings spatial information on the reflection occurred within the sample is the AC one. So, the DC term is usually deleted. The period of the AC component and so, the resulting A-scan data are evaluated by finally doing the Fourier transformation:

$$FT^{-1}[I_{AC}(\omega)] = G_{sr}(t-\tau) + G_{sr}(-t-\tau) \tag{5.17}$$

where $G_{sr}(t)$ is the correlation product of the electrical fields of the reference arm and sample arm, and τ is the temporal period of the oscillation and also, the delay between the radiations travelled along reference and sample arm. The relationship between the delay and the optical path difference is the following one:

$$\tau = \frac{2\Delta l}{c} \tag{5.18}$$

So far, a sample with only one reflective interface has been considered. So, only one AC term would appear. If the sample possesses multiple reflective interfaces, the oscillating terms (i.e. AC terms) related to each spatial location of a single reflection occurred within the sample and revealed through the Fourier transformation, would be multiple as well.
The axial resolution of the system corresponds to the coherence length of the source and so, depends, again, on the width of the optical source as for the TD-OCT approach (i.e. equation (5.12)).

5.2.3 SS-OCT approach

Unlike TD-OCT and SD-OCT approaches where the intensity data are acquired simultaneously, in this other configuration, data are collected sequentially. The source is a tunable laser characterized by a tight bandwidth that performs a linear wavelength/frequency sweep. In Figure 5.4 a scheme of a typical SS-OCT A-scan system is shown. The reference arm goes to a fixed mirror as in SD-OCT approach. Since the coherence of the source signal is very high and the propagation time along the sample arm is supposed to be longer than the one along the reference arm, the reflected radiations coming back from mirror and sample constructively interfere and the photodiode acquires simultaneously radiations that enter the interferometer at different times. The frequency difference between the acquired radiations is proportional to the optical path difference, because of the linear sweep of the source. This allows the visualization of a peak in the frequency domain which brings to the acquisition of the position of the corresponding reflective interface within the sample, after the Fourier transformation

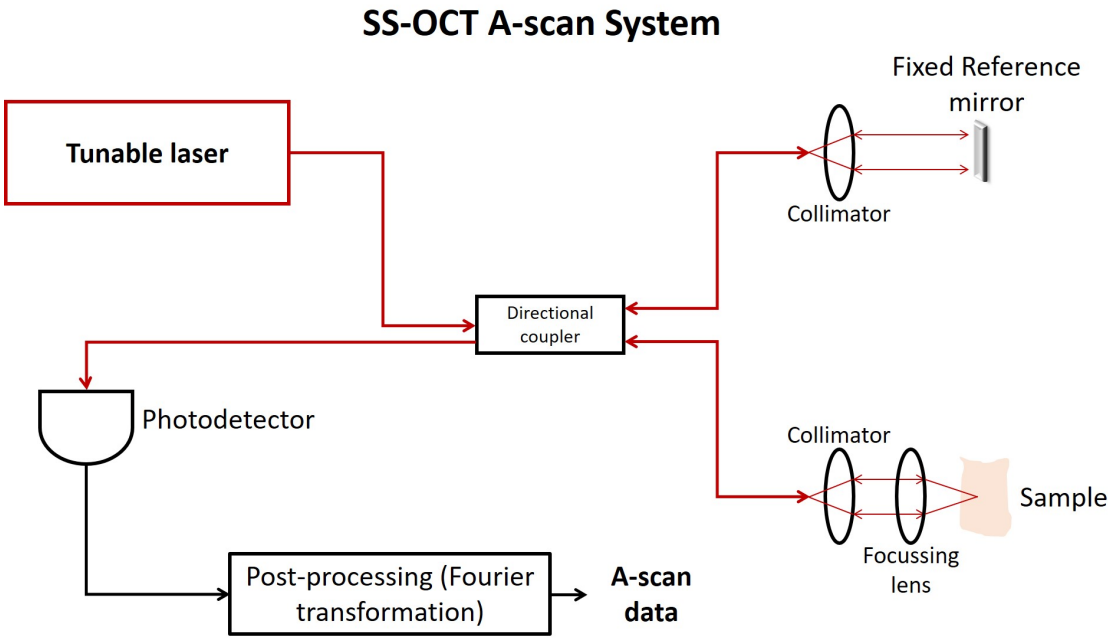

Figure 5.4: *Scheme of a typical SS-OCT A-scan system.*

of the signal [151].
Analytically [151], the electrical field generated by the tunable laser can be described by the following equation:

$$\vec{E_{so}}(t) = E_{so} exp\left[j\omega(t)t\right] \tag{5.19}$$

where $\omega(t)$ varies linearly in time:

$$\omega(t) = \omega_0 + mt \tag{5.20}$$

where ω_0 is the initial angular frequency and $m = \frac{d\omega}{dt}$ is the chirp rate. Considering again a sample with a single reflective interface at $\Delta l = |l_s - l_r|$, at $t = t_i$ the tunable laser sends a radiation with angular frequency of ω_i. This wave is splitted at the interferometer, one part goes to the mirror and the other part to the sample. The reflected radiation coming from the sample, comes back at the instant $t_i + 2t_s$, while the reflected radiation coming from the reference mirror comes back before, at $t_i + 2t_r$. Since $t_s > t_r$, the reference radiation is associated to a different frequency with respect to the sample one. This results in different angular frequencies (ω_s and ω_r) of the acquired reflections coming from the sample and reference arms respectively:

$$\omega_s = \omega(t_i) \tag{5.21}$$

$$\omega_r = \omega(t_i + 2t_s - 2t_r) = \omega(t_i - \tau) \tag{5.22}$$

where τ is the delay between the two radiations that is correlated to the optical path difference (Δl) as it is shown in equation (5.18). Thus, at $t_i + 2t_s$ the phenomenon of signal beat happens at the interferometer and the final signal coming out and acquired by the photodiode is characterized by an angular frequency (ω_{beat}) which is correlated

to Δl as following:

$$\omega_{beat} = m\tau = m\frac{2\Delta l}{c} \tag{5.23}$$

By applying the Fourier transformation in post-processing, the position of the reflective interface is finally retrieved. In case of sample with multiple reflective interfaces, the acquired interference signal would contain multiple beat frequencies (i.e. $\omega_{beat,i}$). Each frequency is correlated to the optical path difference of each single interface and, therefore, the result, after the Fourier transformation, would be a series of peaks at the positions corresponding to the depth of each single reflective interface.

5.2.4 Comparison between the three OCT A-scan approaches

The TD-OCT configuration has been the first approach used for the implementation of A-scan systems. It is characterized by broadband optical source and a moving mirror which allows to retreive the axial profile of the sample under test. This allows the user to have the A-scan data in time domain without additional post-processing operations (i.e. Fourier transformation). However, the translation of the mirror not only adds eventual mechanical noise to the signal, but also limits the frame rate of the system. Indeed, for a given scan period (T_{scan}), a TD-OCT system guarantees only a limited time (t_l) for the acquisition of the signal that is given by the following formula:

$$t_l = \frac{l_c}{z_s} T_{scan} \tag{5.24}$$

where z_s is the path travelled by the mirror which corresponds to the depth scanned by the system through the sample. In particular, the inverse of the scan period represents the frame rate of the system (f_{sys}) which depends on the scan speed of the mirror (v_m) as following:

$$f_{sys} = \frac{1}{T_{scan}} = \frac{2v_m}{\lambda} \tag{5.25}$$

This implies that TD-OCT A-scan systems are characterized by limited frame rates which are usually only tens of kHz.
The frequency domain approaches are younger and deletes these limits introduced by the translation of the reference mirror, by fixing it and acquiring the signals in frequency domain. In particular, SD-OCT A-scan systems are characterized by a spectrometer that discriminates the frequency components of the signal coming out from the interferometer. The Fourier transformation of the output of the spectrometer allows the recovery of the A-scan data. The result is an A-scan system which is much faster than traditional TD-OCT configurations (i.e. frame rates up to 100 kHz).
On the other hand, with the SS-OCT approach, it has been obtained a system which is as simple as the TD-OCT ones (i.e. both absence of the spectrometer and moving mirror), but guarantees the high frame rates of the SD-OCT configurations.
In the next section, some basics on the real-time optical Fourier transformation (RT-OFT) are given. Indeed, in this work it is experimentally demonstrated that an A-scan system, based on this new optical approach, has the capability of increasing the frame rates from a maximum of 100 kHz typical of actual OCT systems, to 1 MHz.

5.2.5 Real-time optical Fourier transformation

A key tool for signal processing is the Fourier Transformation which allows the transformation of a signal from frequency to temporal domain and vice versa. Over the years, in the field of Photonics, many studies have been focused on the implementation of methods for the Fourier transformation in the optical domain (i.e. all-optical Fourier transformation). Such methods allow to perform the Fourier transformation in the analog domain by skipping signal post-processing steps after optoelectronic conversion, signal acquisition and digitalization. This could imply the potential of higher speed in temporal optical signal processing which is an important concept widely investigated for a large range of applications including ultra-fast computing [152], ultrafast laser pulse manipulation, control and measurements [153], high-speed information processing in optical communications [49,154], microwave engineering [155,156] and, last but not least, biomedical imaging [157]. All-optical Fourier transformation was predominately investigated on spatial-domain light waves. However, recently, similar techniques have been investigated also for the manipulation of temporal optical signal such as the RT-OFT which allows to map the spectrum of the signal under test in the temporal domain by means of analog optical components only [146–148, 158]. Whereas many applications still requires the manipulation of the output signal through digital signal processing (i.e. retrieving of the optical spectrum through the Fourier transformation) introducing additional processing times and latencies, RT-OFT enables the acquisition of the energy signal spectrum without post-processing operations at a very high speed (i.e. update rates into the MHz range) [159–163].
The method implemented in this work is the real-time Fourier transformation (RT-OSFT) which implements the RT-OFT of a given optical energy spectrum, normally captured through an optical spectrum analyzer (OSA). Thus, it fits well for applications such as optical frequency domain reflectometry and OCT platforms [163–165]. It is based on the time-spectrum convolution concept which consists of the temporal convolution between an input incoherent energy spectrum and a temporal modulation waveform, i.e. the kernel function. Then, the resulting modulated field propagates through a linear dispersive medium which induces a uniform group velocity dispersion (GVD), $\ddot{\Phi}$, over the entire input optical bandwidth. In particular, such uniform group velocity dispersion is defined as:

$$\ddot{\Phi} = \frac{-\delta^2 \Phi}{\delta \omega^2} \tag{5.26}$$

where $\Phi(\omega)$ is the spectral phase transfer function of the dispersive medium along the bandwidth of the input source. The output of the time-spectrum convolution is an average time-domain optical intensity which is proportional to the convolution of the temporal modulation intensity and a time-scale version of the incoherent light energy spectrum (input of the system). In the system proposed in this work, a chirped temporal sinusoidal waveform is used as temporal modulation waveform.
A simplified scheme is given in Figure 5.5 where a broadband rectangular pulse is used as input. Given a chirped temporal sinusoidal waveform $m(t)$ [166]:

$$m(t) = cos\left(\frac{D_m}{2} t^2\right) \tag{5.27}$$

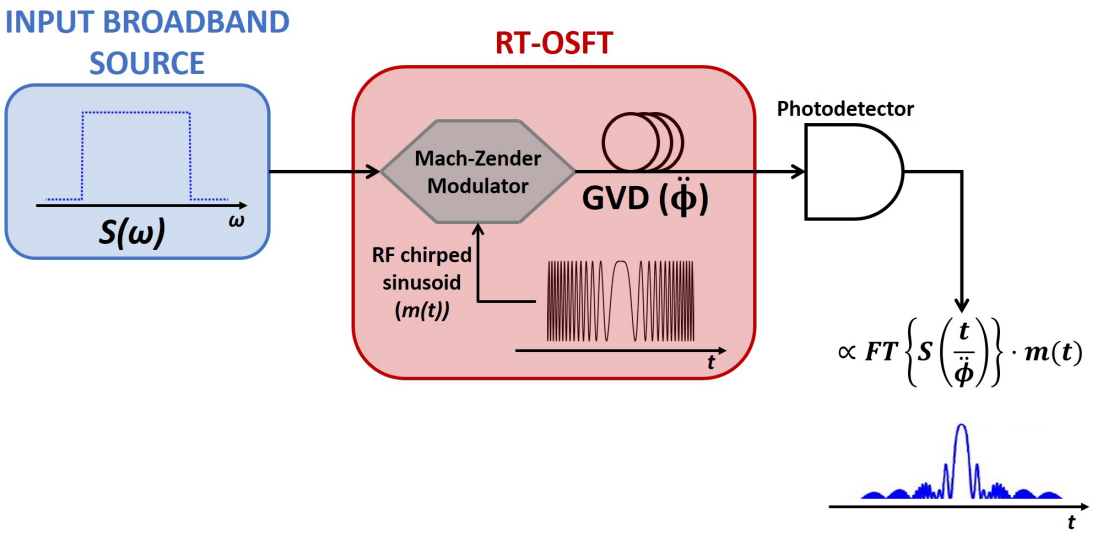

Figure 5.5: *Scheme of the RT-OSFT process with a spectral input characterized by a broadband rectangular waveform.*

where $D_m = \frac{\Delta\omega_m}{\Delta t_m}$ is the linearly chirped term of the temporal modulation sinusoid which shows an instantaneous angular frequency ranging from 0 to $\Delta\omega_m$ in a temporal period dictated by Δt_m. If the applied GVD is sufficiently high (i.e. first-order dispersion), it has been demonstrated that at the output of the process, the resulting convolution integral of the output energy spectrum can be approximated as the real/imaginary part of its Fourier transformation [166, 167]:

$$S\left(\frac{t}{\ddot{\Phi}}\right) \otimes m(t) \cong Re\left[s(\omega') \cdot exp\left(j\frac{D_m}{2}t^2\right)\right] \tag{5.28}$$

with,

$$s(\omega') = FT\left[S\left(\frac{t}{\ddot{\Phi}}\right)\right] \tag{5.29}$$

where $S(\omega)$ is the energy spectrum of the input, with bandwidth $\Delta\omega$ around a given central optical frequency (ω_c), $\ddot{\Phi}$ is the first order dispersion and FT states as Fourier transformation. It is important to note that the temporal period of the chirped sinusoid (Δt_m) defines the switching time between consecutive realizations of the RT-OSFT process. Consequently, the maximum measurement frame rate (f_{rate}) is defined as following:

$$f_{rate} = \frac{1}{\Delta t_m} \tag{5.30}$$

Furthermore, the equivalence (5.28) is valid under two important conditions that should be verified for a correct functioning of the process [147, 166]. The first one is the Fraunhofer condition:

$$D_m << \frac{8\pi}{(|\ddot{\Phi}|\Delta\omega)^2} \tag{5.31}$$

where $\Delta\omega$ is the FWHM of the optical broadband source. It is important to satisfy this condition because it translates into a temporal separation of the spectral component of

the input broadband energy spectrum which is the basis of RT-OSFT. The second condition (i.e. dispersion condition) is the following inequality, involving the bandwidth of the chirped sinusoid and the dispersion parameter:

$$|\Delta\omega_m^2 \frac{\ddot{\Phi}}{8}| << \pi \tag{5.32}$$

Equation (5.32) basically guarantees that the optical dispersion is kept sufficiently low in such a way to prevent eventual distortions of the temporal modulated waveform while propagating through the optical dispersive medium.
From both conditions (equations (5.31) and (5.32)), the bandwidth of the chirped modulation signal should be larger than the bandwidth of the input energy spectrum which is inversely proportional to the product of optical dispersion and the frequency resolution of the input spectrum ($\delta\omega$). Moreover, the two conditions imposes the following constraint to the temporal period of the chirped modulation waveform:

$$\Delta t_m > |\ddot{\Phi}| \frac{\Delta\omega^2}{\delta\omega} \tag{5.33}$$

Since the temporal period of the modulation function corresponds to the duration of one realization of the RT-OSFT process, from the above inequality, it results that the minimum switching time between consecutive realizations of the RT-OSFT process, is limited by both the bandwidth and the resolution of the input optical spectrum to be processed. Given all these conditions which regulates the performance of RT-OSFT and need to be satisfied, it is clear that for the implementation of an experimental RT-OSFT setup, it is crucial the tuning of the main parameters related to each single optical/electronic component. The most important parameters to be tuned are the bandwidth of the input optical energy spectrum, the GVD, the bandwidth of the temporal modulation waveform and its period.

5.3 Development of an IVOCT A-scan system based on RT-OSFT process

The system based on RT-OSFT concept for IVOCT A-scan has been experimentally developed by taking into account values of frequency chirp and dispersion able to give to the system a penetration capability of 1 mm, typical of conventional IVOCT systems. Then, these parameters have been changed in order to achieve deeper depth. However, the change of parameters for the achievement of deeper penetration depths, has been seen to be responsible of signal distortion affecting the resolution of the system along the temporal/spatial range. This brought to the need of a system calibration for a parameters' optimization aimed to minimize signal distortions. To do so, the A-scan system based on RT-OSFT has been first simulated through a dedicated software for the design of optical and electrical circuits (i.e. VPIPhotonics). Then, the circuit has been calibrated and the optimal value ranges related to the parameters of each single electrical and optical component, have been chosen based on Frahunofer and dispersion conditions (i.e. equations (5.31) and (5.32)). In such a way, the optimal ranges of parameters have been found for a correct implementation of the system.

5.3.1 Experimental development of the system

The scheme of the customized experimental A-scan system for IVOCT based on RT-OSFT that has been developed at our laboratory, is shown in Figure 5.6. A super-

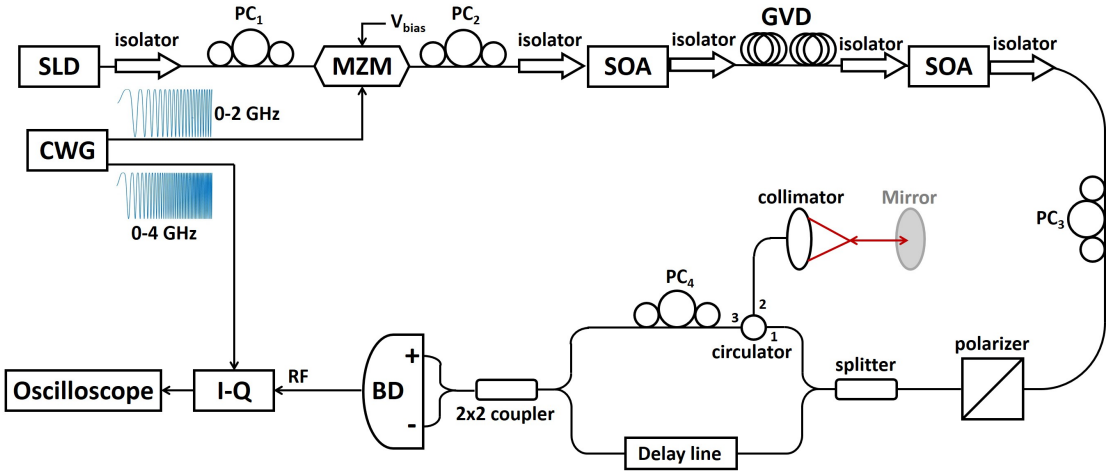

Figure 5.6: *Scheme of the experimental IVOCT A-scan system based on RT-OSFT.*

luminescent diode (SLD) is used as broadband incoherent light source. Its FWHM bandwidth is about 70 nm with central wavelength of 1300 nm, and its typical output power is about 2 mW. The signal generated by the SLD is modulated through a MZM which is driven by a linearly frequency chirped sinusoid generated by a dedicated chirped waveform generator (CWG). The linear frequency chirp goes from 0 to 2 GHz with a repetition period of 1 μs. The required optical GVD of the first order is induced by employing three spools of fibers connected in series. In particular, the spool series is characterized by 24 km of dispersion shifted fiber (LEAF), 5 km of single mode fiber (SMF) and two dispersion compensating modules (PureForm DCM, Avenex). The first two components introduce a first order dispersion of about 408 ps/nm. While the latter ones are added in order to ensure that the second order dispersion contribute can be neglected. Then, a fiber-optics Mach-Zender interferometer (MZI) with a fixed reference arm is placed after the GVD medium. In the sample arm, a mirror is placed. Indeed, for setup validation purposes, the reflection from a single-point target (e.g. mirror) is monitored. The mirror is mount on a tunable delay line, in order to test the setup performance along the entire depth range. The output time-domain signal is captured by a 30 GHz dual balanced photodetector. Then the signal coming out from the photodetector is processed through an IQ demodulator driven by a chirped sinusoid generated by the CWG with a frequency chirp double the one of the waveform sent to the MZM (frequency chirp from 0 to 4 GHz at 1 μm repetition period). The final signal is the squared magnitude of the incoming signal envelope in the scope trace. Furthermore, polarization controllers (PC in Figure 5.11) are added along the circuit together with a polarizer before the MZI, in order to maintain a constant and linear polarization of light. Two semiconductor optical amplifiers (SOA) are placed before the GVD components and the MZI respectively, in order to guarantee high enough power at the system output.

In Figure 5.7 the results from the test of the described A-scan setup are shown. In

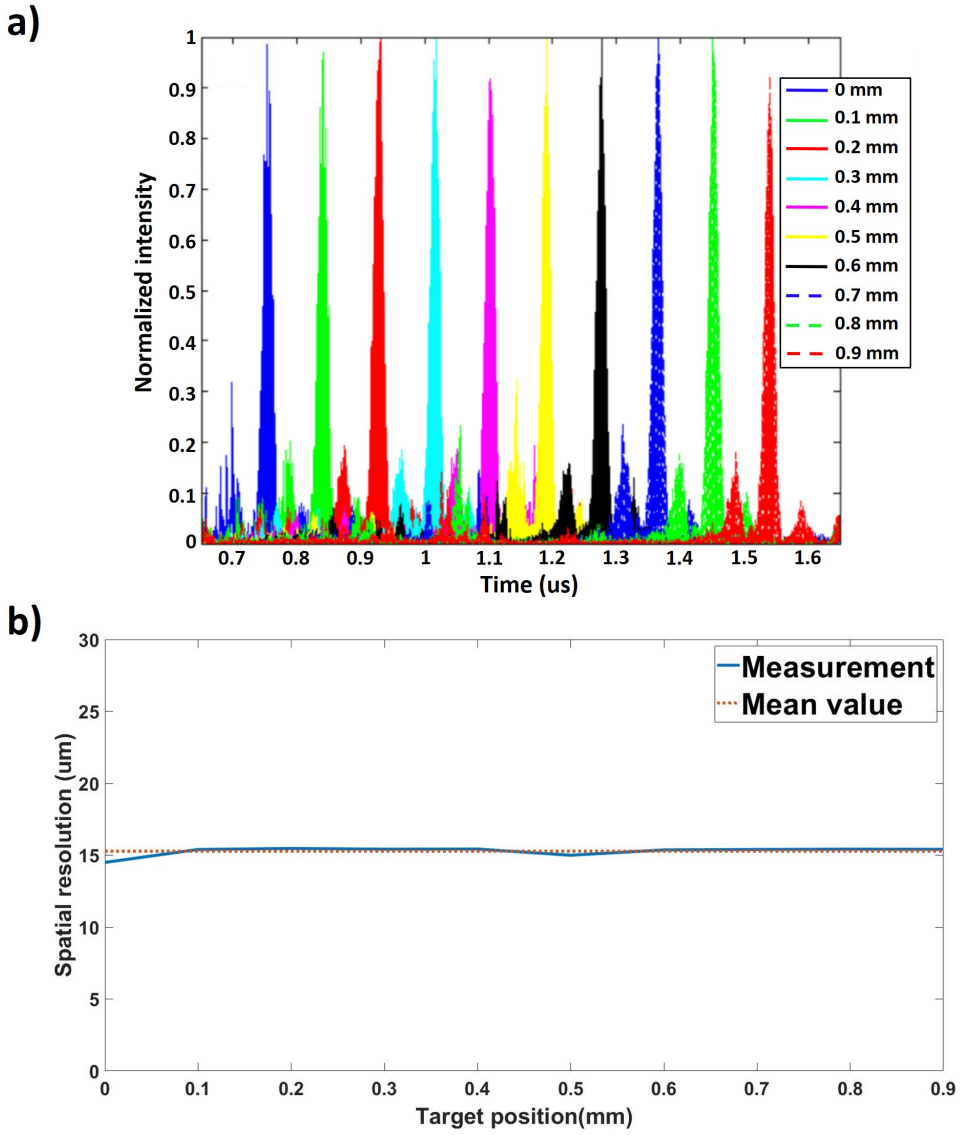

Figure 5.7: *a) Output of the A-scan signals before undergoing post-processing procedure (IQ demodulation) as function of the temporal range, acquired by moving the target mirror within the spatial range [0,1] mm with a step size of 0.1 mm; b) spatial resolution of the system along the spatial range.*

Figure 5.7a a set of measurements of the output A-scan temporal signal acquired while shifting the mirror with a step size of 0.1 mm is presented. The signal has not been averaged and has been visualized at the scope with an update rate of 1 MHz (i.e. inverse of the period of the chirped electrical sinusoid). Typically, the signal is a single peak at the location of the reflective interface that is the single-point reflection due to the mirror and is determined, as expected, by the Fourier transformation of the input broadband light spectrum. The temporal/spatial resolution of the system along its penetration depth is typically determined by the FWHM of each single peak acquired for each position of the target mirror. As it is depicted in the plot (Figure 5.7b), the spatial resolution is almost constant along the range, with a mean of 15.28 μm. The maximum penetration depth of the system using the described parameter configuration is 1 mm.

The relationship that bounds the penetration capability (δS) of such system with the parameters of the circuit components, in particular the frequency chirp ($\delta\Omega_m$) and the GVD ($|\ddot{\Phi}|$), is the following one:

$$\Delta S < c|\ddot{\Phi}|\Delta\omega_m \tag{5.34}$$

Considering that the system works in reflection, the maximum analyzed depth within the sample is $\frac{\Delta S}{2}$.
In order to drastically increase the penetration capacity of the system to unprecedented depths never achieved so far in the field of intravascular optical imaging, two further parameter configurations have been tested. Hence, considering equation (5.34), the following parameters have been chosen:

- a frequency chirp of 6 GHz with a longer dispersion shifted fiber of 24 km, for a total first order dispersion of 408 ps/nm;
- a frequency chirp of 6 GHz with a dispersion shifted fiber of 28 km, for a total first order dispersion of 476 ps/nm.

These configurations have been tested on a single-point target (i.e. a mirror) and the corresponding results are shown in Figure 5.8. As it can be seen from the plot of the output signals of the system (Figure 5.8a,b), the two configurations taken into account, guarantee much deeper penetration depth with respect to the first configuration tested (i.e. from 1 mm to 3.3 mm). However the new configurations bring to a considerable signal distortion along the spatial range which translates into a degradation of the system resolution which results to be non-constant along the range. This phenomenon suggests that a trade-off between frequency chirp of the modulated sinusoid and dispersion value has to be found for a proper system operation. To do so, a proper design and calibration of the optoelectronic components of the circuit has been necessary.

5.3.2 System design and calibration

VPIPhotonics circuit

The VPIPhotonics scheme of the designed IVOCT A-scan circuit based on RT-OSFT process is presented in Figure 5.9. VPIPhotonics is a block language where each block corresponds to a certain physical optical or electrical component which performs some designated operations. The blocks are very versatile. Indeed, each one possesses a list of local parameters that can be adjusted in order to adapt the performed operations to each specific working process. Furthermore, a list of global parameters, valid for all the blocks of the circuit, can be set, i.e. temporal and spectral windows of the generated signals, centre frequency and number of sample characterizing the signal.
The part of the circuit simulating the RT-OSFT process (Figure 5.10a) consists of the generation and interference of an optical gaussian broadband spectrum (Figure 5.11a), i.e. centre wavelength 1300 nm, and a sine frequency chirped electrical signal (Figure 5.11b). Then the resulting interference signal (Figure 5.11c) travels through a GVD medium (i.e. chromatic dispersion of the first order). The broadband optical spectrum is generated by filtering white gaussian noise with a first-order gaussian filter. The linearly frequency chirped sinusoid is generated through a Matlab program, imported in VPIPhotonics and then normalized. The optical and electrical signals interfere through

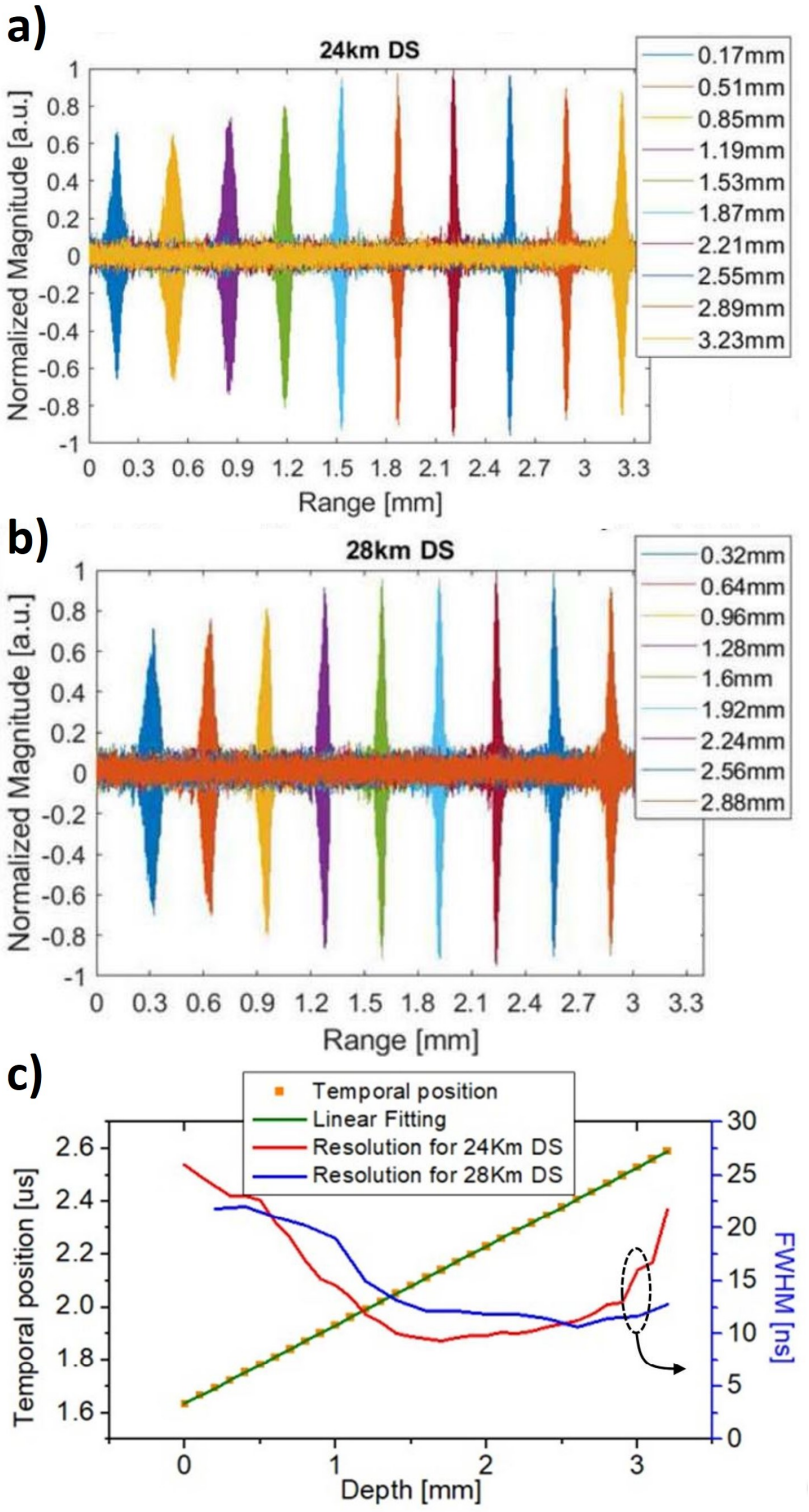

Figure 5.8: *Output signals of the A-scan system as function of the spatial range [0,3.3] mm with a) 24km dispersion shifted fiber and b) 28km dispersion shifted fiber; c) spatial resolution of the two configurations along the spatial range.*

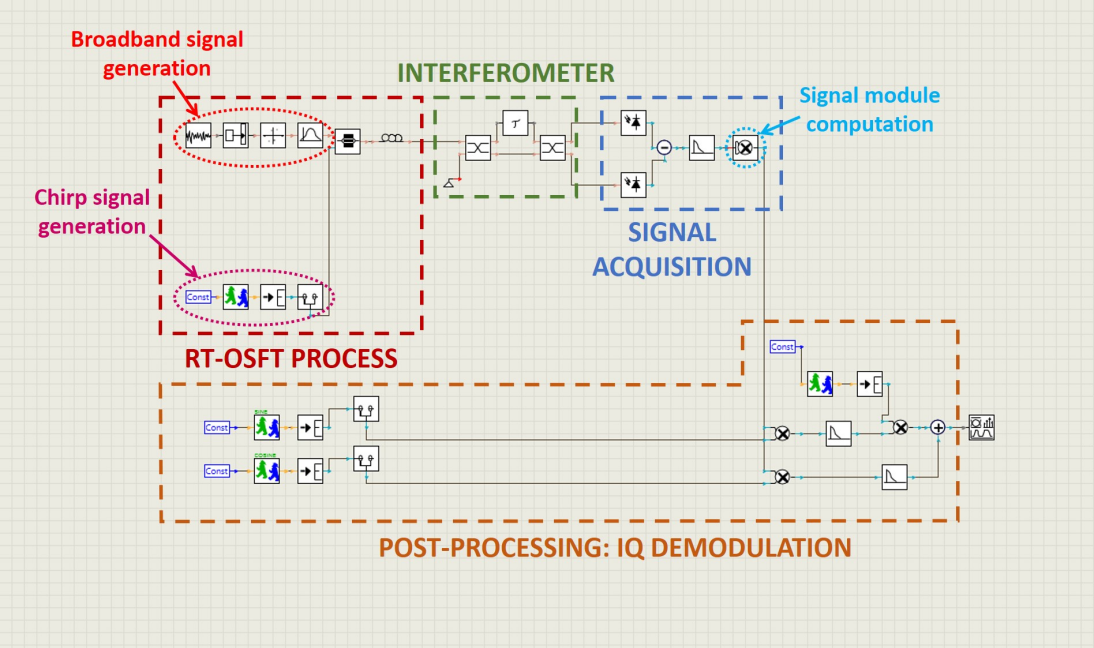

Figure 5.9: *Scheme of the circuit for RT-OSFT A-scan designed on VPIPhotonics.*

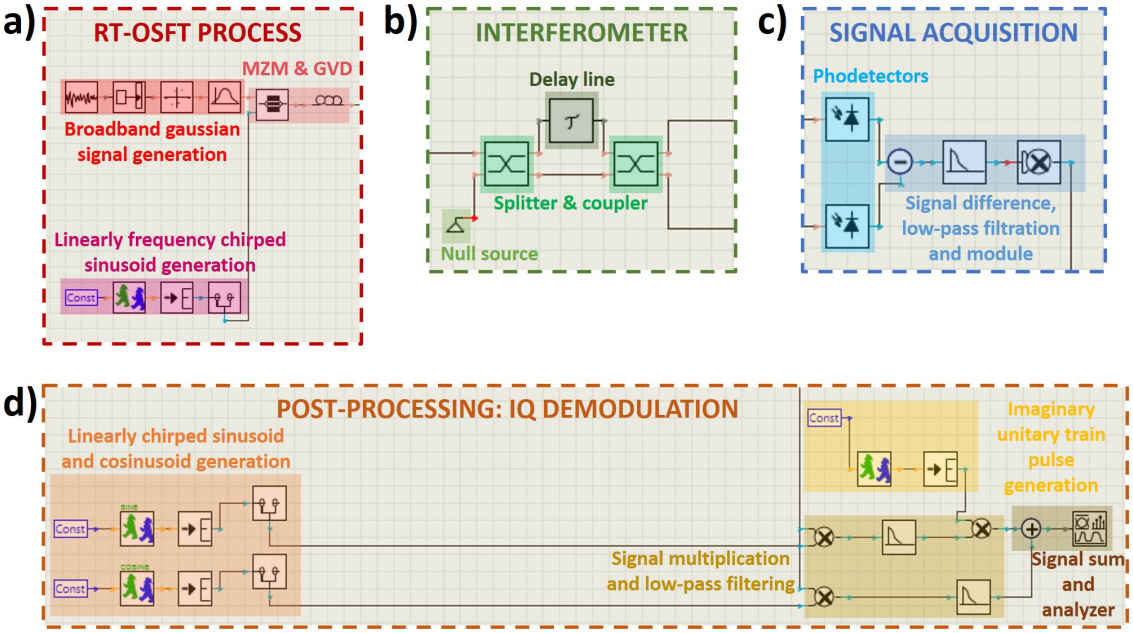

Figure 5.10: *Zoom of each single part of the VPIPhotonics circuit presented in Figure 5.6: a) RT-OSFT process, b) interferometer, c) analogic signal acquisition, and d) IQ demodulation of the acquired signal.*

a Mach-Zender modulator (i.e. MZM in Figure 5.10a) whose bias voltage is set in such a way to both maximize the output signal and prevent eventual distortion. Then, the signal resulting from such modulation travels through the last component involving the RT-OSFT process, that is a block which simulates chromatic dispersion of the first or-

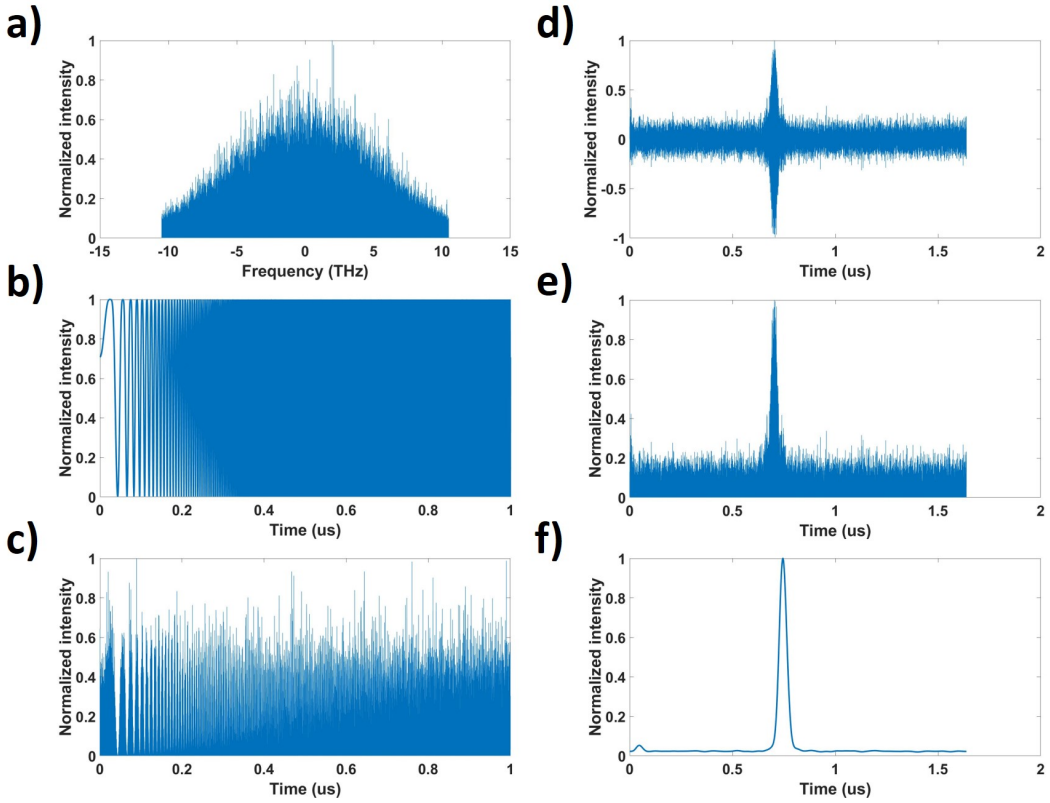

Figure 5.11: *a) Broadband gaussian optical spectrum, b) linearly frequency chirped sinusoid waveform, c) interference between the broadband spectrum and the chirped waveform, d) system output signal coming from the interference between the RT-OSFT output signal and its delayed counterpart (i.e. delay time of 3 ps), e) module of the system output signal, and d) its envelope.*

der (i.e. GVD in Figure 5.10a).
The signal resulting from the RT-OSFT process, which is basically the Fourier transformation of the input gaussian spectrum, goes to the interferometer (i.e. typical component of every OCT A-scan), shown in Figure 5.10b. It is constituted by a splitter which sends part of the input signal (the one coming out from the RT-OSFT process) to the reference arm, which keeps the signal unaltered, and the other part to the sample arm which is characterized by a block that simulates a total reflective interface (e.g. a mirror) at a certain position by introducing a temporal delay line (TDL) into the travelling signal. The actions of increasing or decreasing the TDL correspond to simulations of a certain translation of the reflective interface to be investigated. The important thing is to keep such delay lower than the coherence time of the simulated system.
Then, reference and sample signals are acquired and subtracted. This is made by the analog acquisition part of the circuit (Figure 5.10c) which is constituted by two photodetectors which acquires the reference and sample signals separately. Then, the signal resulting from the difference between the photodetectors' outputs is filtered through a low-pass electrical filter. The result is a signal characterized by both a positive and a negative peak (Figure 5.11d) at the location of the reflective interface which is simulated by the TDL block of the interferometer. The module of this signal is further computed in order to cancel out its negative components (Figure 5.11e). Hence, the

row output signal of the conceived A-scan IVOCT system based on RT-OSFT is a positive peak at a location corresponding to the set TDL.
Finally, this signal undergoes post-processing consisting of an IQ demodulation procedure (Figure 5.10d) which allows to compute the envelope of the input positive peak (Figure 5.11f). The IQ demodulation is characterized by three main step [168]:

- Down-mixing: the input signal is split and its two copies are multiplied by a sinusoid (i.e. In-phase component) and a cosinusoid (i.e. Quadrature component) respectively. The sinusoid term is then multiplied by the imaginary unit in such a way that a real component and an imaginary component appear. In our case, the cosine and sine signals are linearly frequency chirped, with a chirp factor that is double the one of the electrical sinusoid interfering with the optical spectrum at the Mach-Zender modulator.
- Low-pass filtering: the complex signal is low-pass filtered in order to remove the negative frequency spectrum and cancel out eventual noise within the desired bandwidth.
- Reconstruction of the envelope of the original signal: the two filtered components (i.e. real and imaginary components) are summed.

The final result of this operation is the square magnitude envelope of the output signal of the A-scan system, which is the one shown in Figure 5.10d.

System calibration and parameter optimization

The search for the optimal conditions to guarantee a high system performance has been carried out soon after the circuit assembly in VPIPhotonics, exploiting equations (5.31) and (5.32).
In particular, the calibration of the system has been carried out through the optimization of both the local parameters of each block and the global parameters valid for the entire circuit. The main goal of this step was to find a compromise between resolution, frame rate and penetration depth. To do so, the Fraunhofer and dispersion conditions (i.e. equations (5.31) and (5.32)) were taken into account. From equation (5.31), the Fraunhofer term (i.e. $\frac{\Delta\omega_m}{\Delta t_m}(|\ddot{\Phi}|\Delta\omega)^2$) has been made explicit as follows:

$$D_m(|\ddot{\Phi}|\Delta\omega)^2 << 8\pi \longrightarrow \frac{\Delta\omega_m}{\Delta t_m}(|\ddot{\Phi}|\Delta\omega)^2 << 8\pi \tag{5.35}$$

While, from (5.32), the dispersion term (i.e. $|\Delta\omega_m^2 \frac{\dddot{\Phi}}{8}|$) is already explicit. Both inequalities have been analyzed and the Fraunhofer and dispersion terms have been plotted as function of chromatic dispersion ($\ddot{\Phi}$) and chirp bandwidth of the sinusoid signal ($\Delta\omega_m$) as shown in the plots in Figure 5.12. In particular, the analysis of the two terms as function of the chromatic dispersion has been carried out for different values of the chirp bandwidth within the range $[0.5, 4]GHz$ and vice versa, as function of the chirp bandwidth for different values of the chromatic dispersion within the range $[200, 800]\frac{ps}{nm}$. The bandwidth of the input gaussian spectrum ($\Delta\lambda$) has been kept around 90 nm in order to ensure a small enough coherence length and thus, a good axial resolution. Indeed, the coherence length of the system depends on the bandwidth of the input spectrum as highlighted by equation (5.12). Furthermore, the curves in Figure 5.12 do not change

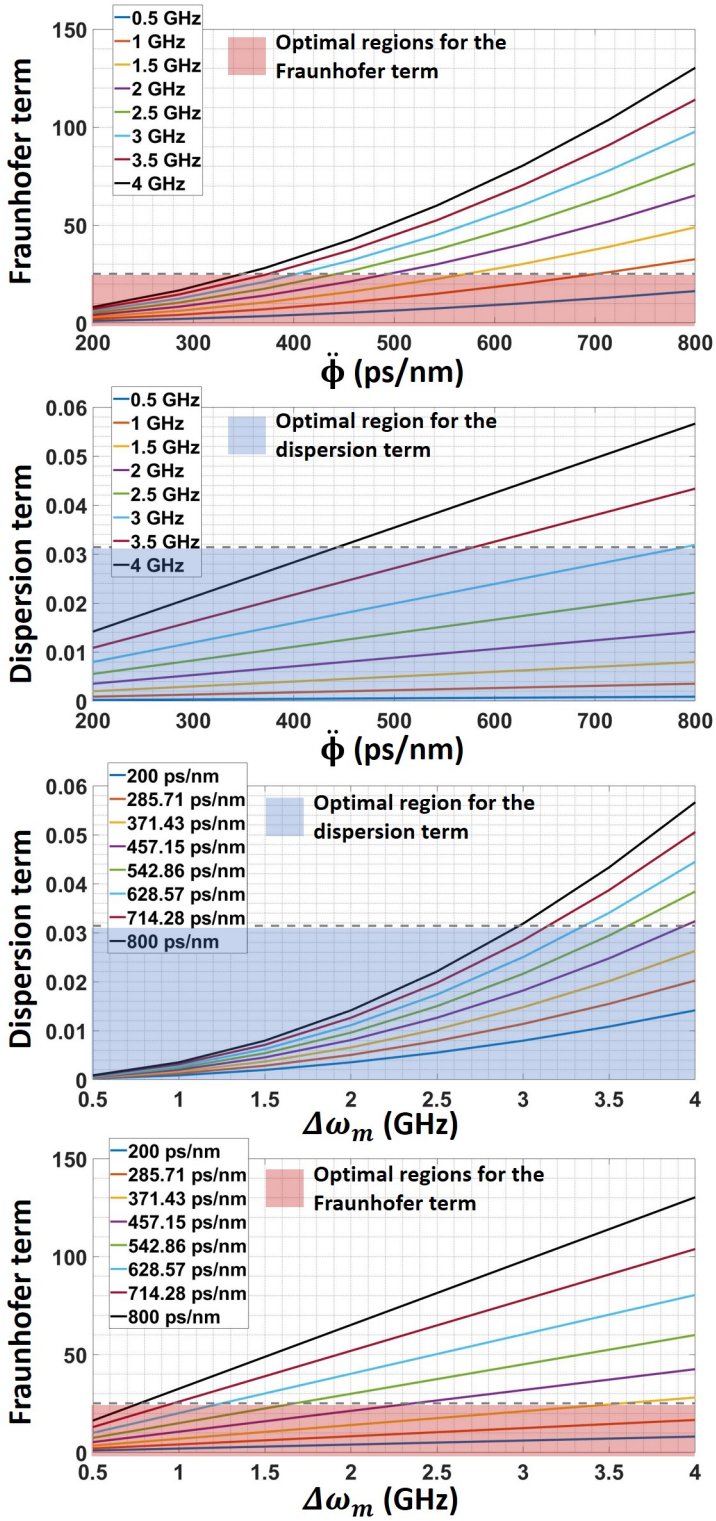

Figure 5.12: *Results of the calibration of the VPIPhotonics circuit. The highlighted regions in each plot represents the values where the Fraunhofer (i.e. blue) or dispersion (i.e. red) conditions are respectively satisfied.* $\ddot{\Phi}$ *is the chromatic dispersion,* $\Delta\omega_m$ *is the chirp bandwidth.*

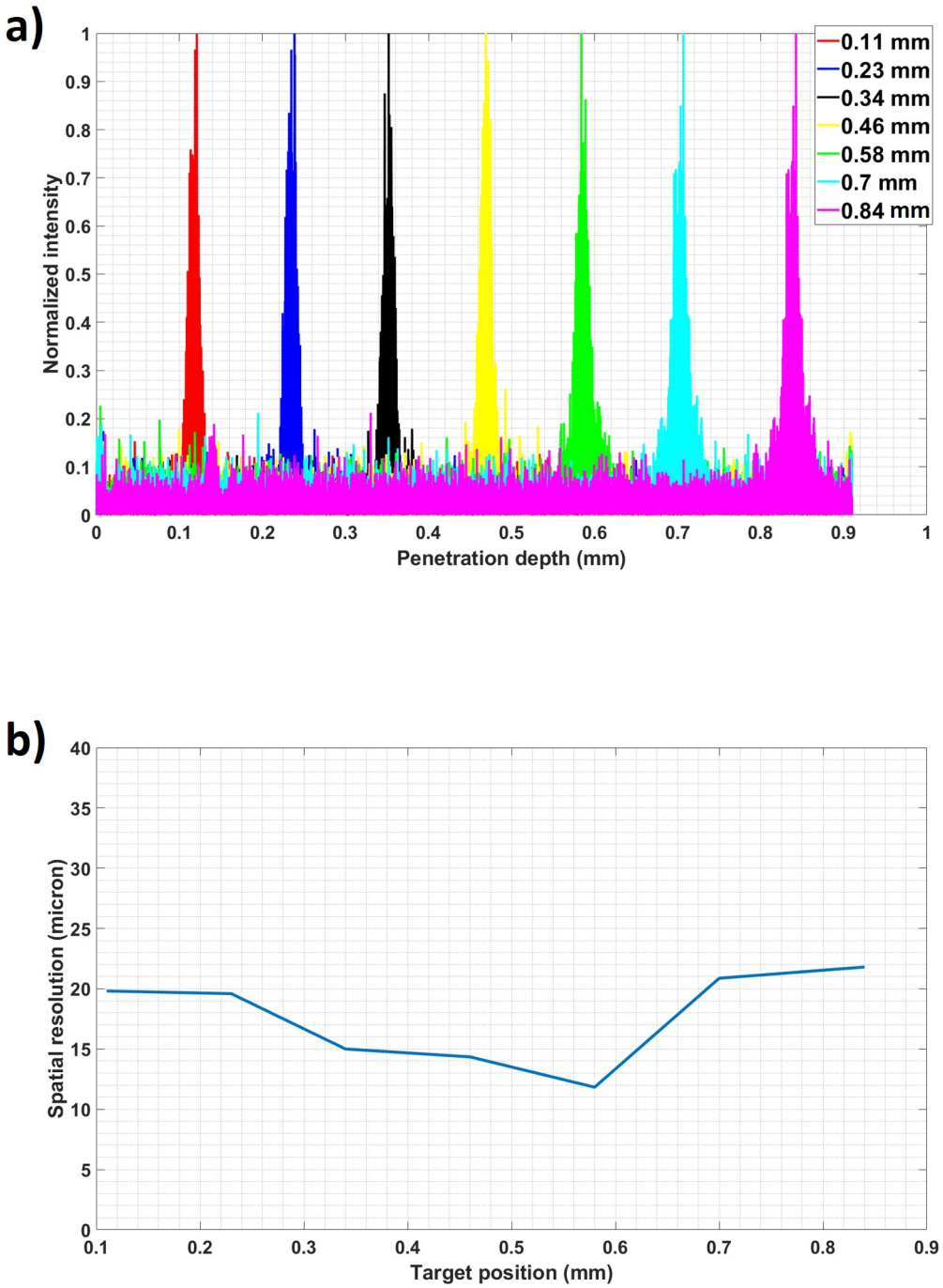

Figure 5.13: *a) output simulation signals before undergoing IQ demodulation as function of the spatial range (input spectrum bandwidth = 70 nm, frequency chirp bandwidth = [0,2] GHz, GVD dispersion 457.15 ps/nm). b) Spatial resolution of the system as function of the target position.*

significantly by varying the input spectrum bandwidth within the range $[70, 100]nm$ which includes high enough values guaranteeing a spatial resolution not higher than 30 μm. In Figure 5.12, for each plot related to Fraunhofer and dispersion conditions, the region characterized by the optimal values of $\ddot{\Phi}$ and $\Delta\omega_m$ are shown. If the values of

these two parameters do not satisfy the two conditions, a distortion of the signal occurs, resulting in a degradation of the system resolution along the temporal/spatial range as it has been found in the experimental measurements with a frequency chirp bandwidth of 6 GHz. The values of $\ddot{\Phi}$ and $\Delta\omega_m$ falling within the optimal values resulting from the system calibration have been collected and also analyzed in terms of the maximum path travelled by the light through the sample (ΔS). Indeed, the penetration capacity of A-scan system based on RT-OSFT is limited by the inequality (5.34). Such relationship, together with the analysis on Fraunhofer and dispersion conditions, suggests a design trade-off between the depth range and resolution of the system. Hence, the input optical spectrum can have a sufficiently broad bandwidth (i.e. within the range [70,100] nm). In turn, the bandwidth of the linear frequency chirp and the chromatic dispersion should be kept at values that satisfy equations (5.31) and (5.32) in order to prevent signal distortions and, so, keep the resolution constant, as much as possible, along the temporal/spatial range, and guarantee a maximum penetration depth of at least 1 mm at the same time (i.e. $\Delta S \geq 2$ mm), for feasibility purposes in the field of IVOCT.
In Figure 5.13, an example of the simulation output signal, with dispersion and chirp bandwidth terms falling within the optimal ranges, is given as function of spatial coordinates (penetration depth) together with the plot of the axial resolution along the spatial range. As it can be noticed from the simulation results and also from the first set of experimental measurements (Figure 5.7), by setting the proper dispersion and chirp bandwidth parameters a good spatial resolution (around 15 μm), almost constant along the spatial range, together with a penetration depth of 1 mm typical of the IVOCT systems can be achieved with this setup based on RT-OSFT that guarantees ultra-high speed in terms of signal acquisition (acquisition time of 1 μs).

5.4 Conclusive remarks

In this chapter, a fiber-optic scheme, referred to as RT-OSFT, for all-optical, real-time calculation of Fourier transformation of a lightwave energy spectrum has been experimentally developed and customized at 1.3μm-wavelength range. It has been demonstrated the high processing speed improvement offered by RT-OSFT method in terms of axial scan, achieving a system update rate within the MHz range while avoiding the need of numerical post-processing typical of conventional approaches. This makes the system interesting for biomedical imaging applications, in particular in the field of intravascular imaging (i.e. IVOCT) where massive spectral data need to be processed in a time period which has to be as short as possible for the safety of the patient under evaluation. Hence, this technology could have the potential of improving the diagnosis of intravascular diseases while significantly diminishing the risk of the patients to undergo cardiac complications thanks to the ultra-fast frame rate.

CHAPTER 6

Conclusion

The current thesis work had the main objectives to develop novel systems and improve already existing methods for the optical characterization of biological tissues by means of optical imaging techniques. In particular, two techniques have been treated, that are small angle light scattering (SALS) and optical coherence tomography (OCT) with a particular focus on intravascular OCT applications (IVOCT).
Regarding the SALS technique, a dedicated optical setup has been developed and integrated into a biaxial testing machine. This activity had the main objective to respond to the need of a complete optomechanical characterization of arterial wall microstructure in terms of both mechanical properties (response to a given stress during biaxial testing), and orientation and dispersion of the inner tissue fibers. These two latter parameters together with mechanical ones, are crucial for the development of constitutive models of aorta wall in both healthy and diseased state. Among all the possible methods able to accomplish to such need, SALS technique has been chosen for its working process simplicity, the relatively low-cost equipment and because damage to the sample, in our case, is a non-issue. For the development of the SALS setup the following steps have been followed:

- study of light propagation in thick samples;
- optical setup design and assembly;
- setup validation;
- opto-mechanical biaxial tests on biological aorta tissue samples.

The first step involves *in-silico* Monte Carlo simulation of light transport in fibrous media. The chose of the Monte Carlo approach instead of the classical one based on the anisotropic diffusion theory, is based on the fact that several studies have demonstrated

that the Monte Carlo methods applied to light transport brings to much more accurate results. This kind of study has been carried out for the purpose to better understand the working principle of the conceived optical setup based on SALS. Indeed, SALS technique has always been applied to very thin biological samples (thickness smaller than 700 μm), while in this case the investigated samples would have been much thicker (thickness >1 mm). From the simulations it has resulted that the SALS analysis is feasible also in this last range of sample thicknesses by slightly change the analysis of the light spot, giving qualitative information on the inner fiber dispersion and a quantitative and precise value related to the main fiber orientation. Then, the optical system has been designed and all the optical components have been carefully chosen. Then vali-

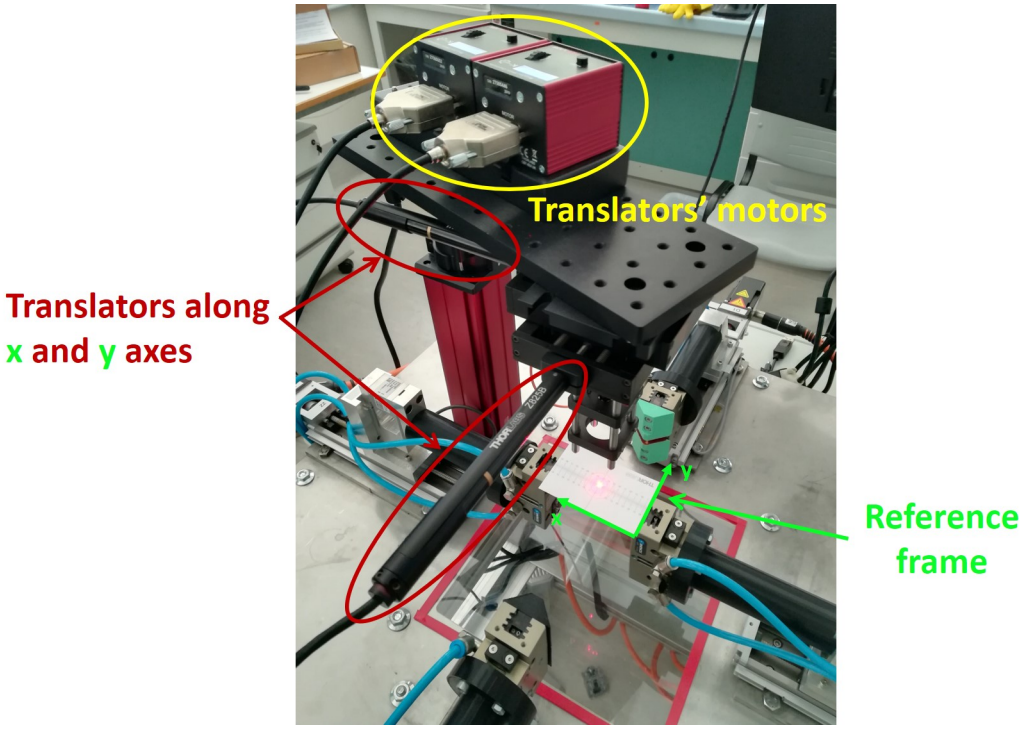

Figure 6.1: *Optical setup automated in two direction for enabling further inner sample structure investigations involving the scanning of the upper sample surface.*

dation measurements have been done on 3D printed samples, demonstrating the actual accuracy of the system. Once the feasibility of the novel optical setup has been tested, it has been integrated into the biaxial machine already developed at the Biocardiolab, and mechanical-biaxial characterization together with optical investigation in real-time of healthy and aTAA aorta tissue samples has been carried out for the first time. It has been demonstrated that the system is able to give important information on the inner fiber rearrangement in real-time during biaxial test using different tension ratios. This kind of analysis is crucial for the development of constitutive models of aorta samples. Moreover, in future, when a consistent number of both healthy and diseased samples are investigated, the information provided by such system could have a potential impact in the clinical study of the pathological features involved in the development of cardiovascular diseases such as aTAA. Last but not least, the optical setup has been made more flexible by adding a collimator (fiber to free-space) at the output of the involved

He-Ne laser and it has also been automated in such a way that a complete planar scanning of the sample can be done by moving the light beam in two direction by means of two translators as shown in Figure 6.1.
If on one side this work has focused on the development of an optical setup for a robust characterization of fibrous biological tissues, on the other hand a deep study on a well-established optical technique for both *in-vivo* and *in-vitro* imaging, i.e. intravascular optical coherence tomography (IVOCT), has been carried out with the main aim to develop and propose novel and innovative methods for the improvement of performance of actual operating systems in terms of light penetration through blood and signal acquisition speed.
To increase light penetration through blood, the exploitation of orbital angular momentum (OAM) technology through the use of Laguerre-Gaussian (LG) beams, is proposed. This study is based on previous works in which the capability of the LG beams of penetrating deeper into turbid media and biological tissue samples with respect to Gaussian (G) ones, conventionally used in current IVOCT applications, is demonstrated at the 633nm-wavelength range (red light). Through this thesis work, this effect has been first demonstrated in the 1300μm-wavelength range (typical of IVOCT systems) by performing measurements in transmission on biological fluids-mimicking samples. Then, for the first time, this effect has been demonstrated also by performing reflection measurements on human blood samples. The experiments performed in this thesis work, are still far from a clinical development and integration of the technology in commercial IVOCT systems. However, they have been very innovative for the scientific community because they represents a strong starting point for future investigations of the benefits of the use of OAM technology rather than G beams in intravascular optical imaging. Indeed, a future development of IVOCT systems based on OAM beams capable of penetrating deeper through blood could bring to unprecedented diagnosis. Further investigations are needed though. And an additional demonstration of this effect should be done through measurements in reflection by using a coherent setup (the simplest one would be a TD-OCT setup, Figure 5.1) able to discriminate the backscattered optical signal coming from the sample along its depth. This kind of analysis would be necessary to quantify the penetration power of such beams through blood more precisely.
Regarding the last, but not least, work implemented in this thesis, an ultra-fast experimental optical axial scan (A-scan) setup operating at 1300μm-wavelength range for IVOCT applications has been developed and optimized. This work has been conceived from the need of ultra-fast signal acquisition in the field of catheter-based intravascular imaging. Indeed, a fast acquisition of the signal is crucial for the safety of patients who could take the risk of undergoing cardiac complications if the imaging procedure is too long. Actual IVOCT A-scan systems are characterized by an update rate of maximum 100 kHz. The main objective of this work has been the implementation of an A-scan system able to achieve update rate up to 1 MHz, ten times higher than conventional systems. This is possible through the exploitation of real-time optical spectrum Fourier transformation (RT-OSFT) which consists on the implementation of Fourier transformation (FT) of the acquired signals directly in the analog domain. This implies the skip of the post-processing steps involving FT that are necessary in actual IVOCT systems, reducing the signal acquisition time from some tens of μs to 1 μs. This translates into the increase of the system frame rate from tens of kHz to 1 MHz. The RT-OSFT has

been usually investigated in many fields involving optical communication and this has been the first time that such concept has been applied to A-scan IVOCT field. The experimental setup has been first build and tested in three parameter configurations. Then, since the optical signal has been seen to get distorted in some parameter conditions, the proposed A-scan system has been simulated through VPIPhotonics software and then optimized in order to retrieve the optimal parameter values for a proper operation of the entire system. Further works on this setup could consist of the performance of measurements in biological samples and the integration of a lateral B-scan for a complete sample characterization and 3D-construction of images in the post-processing part.
In conclusion, this thesis has the main objectives to propose effective optical solutions to problems arisen in both biomedical research field and clinical scenarios. The optical SALS setup has been developed in response to the need of a complete opto-mechanical characterization of fibrous cardiovascular tissues which is crucial for the development of *in-silico* model of aorta, useful for a better understand of its properties and how such properties change in case of diseases. Information that could be very important in clinical scenarios where precise and early disease diagnoses are needed for the safety of the patients. On the other hand, the experimental setups based on OAM technology and RT-OSFT concept have been conceived for the purpose of creating a good starting point for further investigations aimed to finally integrated such methods on IVOCT systems, guaranteeing an unprecedented improvement in terms of light penetration through blood and acquisition speed. Factors that could bring to unprecedented diagnosis of intravascular diseases, while decreasing the risk of collateral effects in patients.

Bibliography

[1] J. C. Watson, A. M. Gorbach, R. M. Pluta, R. Rak, J. D. Heiss, and E. H. Oldfield. Real-time detection of vascular occlusion and reperfusion of the brain during surgery by using infrared imaging. *Journal of Neurosurgery*, 96:918–923, 2002.

[2] J. Marescaux, and L. Soler. Image-guided robotic surgery. *Seminars in Laparoscopic Surgery*, 11(2):113–122, 2004.

[3] K. Hynynen, W. R. Freund, H. E. Cline, A. H. Chung, R. D. Watkins, J. P. Vetro, and F. A. Jolesz. A clinical, noninvasive, mr imaging-monitored ultrasound surgery method. *Imaging and Therapeutic Technology*, 16:185–195, 1996.

[4] S. Celi, N. Martini, L. E. Pastormerlo, V. Positano, and S. Berti. Multimodality imaging for interventional cardiology. *Current Pharmaceutical Design*, 23(22):3285–3300, 2017.

[5] G. Pasterkamp, E. Falk, H. Woutman, and C. Borst. Techniques characterizing the coronary atherosclerotic plaque: influence on clinical decision making? *Journal of the American College of Cardiology*, 36(1):13–21, 2000.

[6] J. A. Elefteriades, and E. A. Farkas. Thoracis aortic aneurysm. *Journal of the American College of Cardiology*, 55(9):841–57, 2010.

[7] D. A. Vorp, B. J. Schiro, M. P. Ehrlich, T. S. Juvonen, M. A. Ergin, and B. P. Griffith. Effect of aneurysm on the tensile strength and biomechanical behavior of the ascending thoracic aorta. *Annals Thoracic Surgery*, 75:2010–4, 2003.

[8] D. A. Vorp, M. L. Raghavan, and M. W. Webster. Mechanical wall stress in abdominal aortic aneurysm: influence of diameter and asymmetry. *Journal of Vascular Surgery*, 27:632–9, 1998.

[9] L. L. LaRoy, P. J. Cormier, T. A. S. Matalon, S. K. Patel, D. A. Turner, and B. Silver. Imaging of abdominal aortic aneurysm. *American Journal of Roentgenology*, 152:785–792, 1989.

[10] P. M. White, J. M. Wardlaw, and V. Easton. Can noninvasive imaging accurately depict intracranial aneurysms? a systematic review. *Radiology*, 217:361–370, 2000.

[11] Y. Honda, and P. J. Fitzgerald. Frontiers in intravascular imaging technologies. *Circulation*, 117:2024–2037, 2008.

[12] A. J. Martin, and R. M. Henkelman. Intravascular mr imaging in a porcine animal model. *Magnetic Resonance in Medicine*, 32:224–229, 1994.

[13] W. J. Rogers, J. W. Prichard, Y. Hu, P. R. Olson, D. H. Benckart, C. M. Kramer, D. A. Vido, and N. Reichek. Characterization of signal properties in atherosclerotic plaque components by intravascular mri. *Atherosclerosis, Thrombosis, and Vascular Biology*, 20:1824–1830, 2000.

[14] L. C. L. Correia, E. Atalar, M. D. Kelemen, O. Ocali, G. M. Hutchins, J. L. Fleg, G. Gerstenblith, E. A. Zerhouni, and J. A. C. Lima. Intravascular magnetic resonance imaging of aortic atherosclerotic plaque composition. *Atherosclerosis, Thrombosis, and Vascular Biology*, 17:3626–3632, 1997.

[15] A. Maehara, G. S. Mintz, and N. L. Weissman. Advances in intravascular imaging. *Circulation: Cardiovascular Intervention*, 2:482–490, 2009.

[16] E. Escolar, G. Weigold, A. Fuisz, and N. J. Weissman. New imaging techniques for diagnosing coronary artery disease. *Canadian Medical Association Journal*, 174(4):487–95, 2006.

[17] K. Nieman, F. Cademartini, P. A. Lemos, R. Raaijmakers, P. M. T. Pattynama, and P. J. de Feyter. Reliable noninvasive coronary angiography with fast submillimeter multislice spiral computed tomography. *Circulation*, 106:2051–2054, 2002.

[18] K. Koch, F. Oelling, K. Oberholzer, P. Bender, P. Kunz, P. Mildenberger, U. Hake, K. F. Kreitner, and M. Thelen. Assessment of right ventricular function by 16-detector-row ct: comparison with magnetic resonance imaging. *European Radiology*, 15:312–318, 2005.

[19] K. U. Juergens, M. Grude, D. Maintz, E. M. Fallenberg, T. Wichter, W. Heindel, and R. Fischbach. Multi–detector row ct of left ventricular function with dedicated analysis software versus mr imaging: initial experience. *Radiology*, 230:2051–2054, 2004.

[20] B. D. MacNeill, H. C. Lowe, M. Takano, V. Fuster, and I. Jang. Intravascular modalities for detection of vulnerable plaque. *Atherosclerosis, Thrombosis, and Vascular Biology*, 23:1333–1342, 2003.

[21] W. Goth, J. Lesicko, M. S. Sacks, and J. W. Tunnell. Optical-based analysis of soft tissue structures. *Annual Review of Biomedical Engineering*, 18:357–385, 2016.

[22] C. Balas. Review of biomedical optical imaging — a powerful, non-invasive, non-ionizing technology for improving in vivo diagnosis. *Measurement Science and Technology*, 20(10):4020–032, 2009.

[23] F. Ishibashi, K. Aziz, G. S. Abela, and S. Waxman. Update on coronary angioscopy: review of a 20-year experience and potential application for detection of vulnerable plaque. *Journal of Interventional Cardiology*, 19:17–25, 2006.

[24] Y. Ueda, M. Asakura, A. Hirayama, K. Komamura, M. Hori, and K. Kodama. Intracoronary morphology of culprit lesions after reperfusion in acute myocardial infarction: serial angioscopic observations. *Journal of the American College of Cardiology*, 27(3):606–10, 1996.

[25] K. Mizuno, A. Miyamoto, K. Satomura, A. Kurita, T. Arai, M. Sakurada, S. Yanagida, and H. Nakamura. Angioscopic coronary macromorphology in patients with acute coronary disorders. *Lancet*, 337:809–12, 1991.

[26] Y. Uchida, F. Nakamura, T. Tomaru, T. Morita, T. Oshima, T. Sasaki, S. Morizuki, and J. Hirose. Prediction of acute coronary syndromes by percutaneous coronary angioscopy in patients with stable angina. *American Heart Journal*, 130:195–203, 1995.

[27] Y. Ueda, T. Ohtani, M. Shimizu, A. Hirayama, and K. Kodama. Assessment of plaque vulnerability by angioscopic classification of plaque color. *Interventional Cardiology*, 148(2):333–335, 2004.

[28] J. Kotani, M. Awata, S. Nanto, M. Uematsu, F. Oshima, H. Minamiguchi, G. S. Mintz, and S. Nagata. Incomplete neointimal coverage of sirolimus-eluting stents. angioscopic findings. *Journal of the American College of Cardiology*, 47:2108–11, 2006.

[29] J. Oyabu, Y. Ueda, N. Ogasawara, K. Okada, A. Hirayama, and K. Kodama. Angioscopic evaluation of neointima coverage: sirolimus drug-eluting stent versus bare metal stent. *American Heart Journal*, 152:1168–74, 2006.

[30] M. Takano, T. Ohba, S. Inami, K. Seimija, S. Sakai, and K. Mizuno. Angioscopic differences in neointimal coverage and in persistence of thrombus between sirolimus-eluting stents and bare metal stents after a 6-month implantation. *European Heart Journal*, 27:2189–2195, 2006.

[31] N. D. Desai, S. Miwa, D. Kodama, G. Cohen, G. T. Christakis, B. S. Goldman, M. O. Baerlocher, M. P. Pelletier, and S. E. Fremes. Improving the quality of coronary bypass surgery with intraoperative angiography. validation of a new technique. *Journal of the American College of Cardiology*, 46(8):1521–5, 2005.

[32] F. Ishibashi, K. Mizuno, A. Kawamura, P. P. Singh, R. W. Nesto, and S. Waxman. High yellow color intensity by angioscopy with quantitative colorimetry to identify high-risk features in culprit lesions of patients with acute coronary syndromes. *American Journal of Cardiology*, 100:1207–1211, 2007.

[33] M. Kawasaki, H. Takatsu, T. Noda, K. Sano, Y. Ito, K. Hayakawa, K. Tsuchiya, M. Arai, K. Nishigaki, G. Takemura, S. Minatoguchi, T. Fujiwara, and H. Fujiwara. In vivo quantitative tissue characterization of human coronary arterial plaques by use of integrated backscatter intravascular ultrasound and comparison with angioscopic findings. *Circulation*, 105:2487–2492, 2002.

[34] F. Prati, E. Regar, G. S. Mintz, E. Arbustini, C. Di Mario, I. Jang, T. Akasaka, M. Costa, G. Guagliumi, E. Grube, Y. Ozaki, F. Pinto, and P. W. J. Serruys. Expert review document on methodology, terminology, and clinical applications of optical coherence tomography: physical principles, methodology of image acquisition, and clinical application for assessment of coronary arteries and atherosclerosis. *European Heart Journal*, 31:401–415, 2010.

[35] J. G. Fujimoto, S. A. Boppart, G. J. Tearney, B. E. Bouma, C. Pitris, and M. E. Brezinski. High resolution in vivo intra-arterial imaging with optical coherence tomography. *Heart*, 82:128–133, 1999.

[36] I. Jang, G. Tearney, and B. Bouma. Visualization of tissue prolapse between coronary stent struts by optical coherence tomography. comparison with intravascular ultrasound. *Circulation*, 104:2754, 2001.

[37] I. Jang, B. E. Bouma, D. Kang, S.-J. Park, S.-W. Park, K. Seung, K. Choi, M. Shishkov, K. Shlendorf, E. Pomerantsev, S. L. Houser, T. Aretz, and G. J. Tearney. Visualization of coronary atherosclerotic plaques in patients using optical coherence tomography: comparison with intravascular ultrasound. *Journal of the American College of Cardiology*, 39(4):604–9, 2002.

[38] C. M. Matter, M. Stuber, and M. Nahrendorf. Imaging of the unstable plaque: how far have we got? *European Heart Journal*, 30:2566–2574, 2009.

[39] H. Yabushita, B. E. Bouma, S. L. Houser, H. T. Aretz, I. Jang, K. H. Schlendorf, C. R. Kauffman, M. Shishkov, D. Kang, E. F. Halpern, and G. J. Tearney. Characterization of human atherosclerosis by optical coherence tomography. *Circulation*, 106:1640–1645, 2002.

[40] T. Kubo, T. Imanishi, S. Takarada, A. Kuroi, S. Ueno, T. Yamano, T. Tanimoto, Y. Matsuo, T. Masho, H. Kitabata, K. Tsuda, Y. Tomobuchi, and T. Akasaka. Assessment of culprit lesion morphology in acute myocardial infarction. ability of optical coherence tomography compared with intravascular ultrasound and coronary angioscopy. *Journal of the American College of Cardiology*, 50(10):933–9, 2007.

[41] I. Jang, G. J. Tearney, B. MacNeill, M. Takano, F. Moselewski, N. Iftima, M. Shishkov, S. Houser, T. Aretz, E. F. Halpern, and B. E. Bouma. In vivo characterization of coronary atherosclerotic plaque by use of optical coherence tomography. *Circulation*, 111:1551–1555, 2005.

[42] P. W. Serruys, J. A. Ormiston, Y. Onuma, E. Regar, N. Gonzalo, H. M. Garcia-Garcia, K. Nieman, N. Bruining, C. Dorange, K. Miquel-Hebert, S. Veldhof, M. Webster, L. Thuesen, and D. Dudek. A bioabsorbable everolimus-eluting coronary stent system (absorb): 2-year outcomes and results from multiple imaging methods. *Lancet*, 373:897–910, 2009.

[43] R. C. Chan, A. H. Chau, W. C. Karl, S. Nadkarni, A. S. Khalil, N. Iftimia, M. Shishkov, G. J. Tearney, M. R. Kaazempur-Mofrad, and B. E. Bouma. Oct-based arterial elastography: robust estimation exploiting tissue biomechanics. *Optics Express*, 12(19):4558–4572, 2004.

[44] J. K. Barton, and F. G. A. Tumlinson. Dual modality instrument for simultaneous optical coherence tomography imaging and fluorescence spectroscopy. *Journal of Biomedical Optics*, 9(3):618–623, 2004.

[45] G. J. Tearney, S. Waxman, M. Shishkov, B. J. Vakoc, M. J. Suter, M. I. Freilich, A. E. Desjardins, W. Oh, L. A. Bartlett, M. Rosenberg, and B. E. Bouma. Three-dimensional coronary artery microscopy by intracoronary optical frequency domain imaging. *Journal of the American College of Cardiology*, 1(6):752–761, 2008.

[46] L. Liu, J. A. Gardecki, S. K. Nadkarni, J. D. Toussaint, Y. Yagi, B. E. Bouma, and G. J. Tearney. Imaging the subcellular structure of human coronary atherosclerosis using micro–optical coherence tomography. *Nature Medicine*, 17(8):1010–14, 2011.

[47] M. Kashiwagi, L. Liu, K. K. Chu, C.-H. Sun, A. Tanaka, J. A. Gardecki, and G. J. Tearney. Feasibility of the assessment of cholesterol crystals in human macrophages using micro optical coherence tomography. *PLoS One*, 9(7):e102669, 2014.

[48] D. K. Hamilton, J. R. Sheppard. Differential phase contrast in scanning optical microscopy. *Journal of Microscopy*, 133(1):27–39, 1984.

[49] P. O. Bayguinov, D. M. Oakley, C.-C. Shih, D. J. Geanon, M. S. Joens, and J. A. J. Fitzpatrick. Modern laser scanning confocal microscopy. *Current Protocols in Cytometry*, e39:doi:10.1002/cpcy.39, 2018.

[50] W. B. Amos, and J. G. White. How the confocal laser scanning microscope entered biological research. *Biology of the Cell*, 95:335—-342, 2003.

[51] W. B. Amos, J. G. White, and M. Fordham. Use of confocal imaging in the study of biological structures. *Applied Optics*, 26(16):3239–3243, 1987.

[52] M. Rajadhyaksha, M. Grossman, D. Esterowitz, R. H. Webb, and R. R. Anderson. In vivo confocal scanning laser microscopy of hultlan skin: melanin provides strong contrast. *Journal of Investigative Dermatology*, 104:946–952, 1995.

[53] G. J. Brakenhob, H. T. M. Van der Voort, E. A. Van Spronsen, and N. Nanninga. Three-dimensional imaging in fluorescence by confocal scanning microscopy. *Journal of Microscopy*, 153(2):151–159, 1989.

[54] M. Rajadhyaksha, R. R. Anderson, R. H. Webb. Video-rate confocal scanning laser microscope for imaging human tissues in vivo. *Applied Optics*, 38(10):2105–2115, 1999.

[55] J. G. White, W. B. Amos, and M. Fordham. An evaluation of confocal versus conventional imaging of biological structures by fluorescence light microscopy. *Journal of Cell Biology*, 105:41–48, 1987.

[56] C. L. Smithpeter, A. K. Dunn, A. J. Welch, and R. Richards-Kortum. Penetration depth limits of in vivo confocal reflectance imaging. *Applied Optics*, 37(13):2749–54, 1998.

[57] K. S. Nehal, D. Gareau, and M. Rajadhyaksha. Skin imaging with reflectance confocal microscopy. *Seminars in Cutaneous Medicine and Surgery*, 27(13):37–43, 2008.

[58] F. Helmchen, and W. Denk. Deep tissue two-photon microscopy. *Nature Methods*, 2(12):932–940, 2005.

[59] G. H. Patterson, and D. W. Piston. Photobleaching in two-photon excitation microscopy. *Biophysical Journal*, 78:2159—-2162, 2000.

[60] W. Denk, D. W. Piston, and W. W. Webb. Two-photon molecular excitation in laser-scanning microscopy. *Handbook of Biological Confocal Microscopy*, Chapter 28:445—-458, 1995.

[61] M. Oheim, E. Beaurepaire, E. Chaigneau, J. Mertz, and S. Charpak. Two-photon microscopy in brain tissue: parameters influencing the imaging depth. *Journal of Neuroscience Methods*, 111:29—-37, 2001.

[62] K. H. Kim, C. Buehler, and P. T. C. So. High-speed, two-photon scanning microscope. *Applied Optics*, 38:6004—-09, 1999.

[63] T. J. Farrell, M. S. Patterson, and B. Wilson. A diffusion theory model of spatially resolved, steady-state diffuse reflectance for the noninvasive determination of tissue optical properties in-vivo. *Medical Physics*, 19(4):879—-888, 1992.

[64] J. L. Kinsey. Laser-induced fluorescence. *Annual Review of Physical Chemistry*, 28:349—-372, 1977.

[65] Z. Movasaghi, S. Rehman, and I. U. Rehman. Raman spectroscopy of biological tissues. *Applied Spectroscopy Reviews*, 28:349—-372, 2007.

[66] J. D. Caplan, S. Waxman, R. W. Nesto, and J. E. Muller. Near-infrared spectroscopy for the detection of vulnerable coronary artery plaques. *Journal of the American College of Cardiology*, 47(8):C92—-6, 2006.

[67] P. R. Moreno, R. A. Lodder, K. R. Purushothaman, W. E. Charash, W. N. O'Connor, and J. E. Muller. Detection of lipid pool, thin fibrous cap, and inflammatory cells in human aortic atherosclerotic plaques by near-infrared spectroscopy. *Circulation*, 105:923–927, 2002.

[68] C. M. Gardner, H. Tan, E. L. Hull, J. B. Lisauskas, S. T. Sum, T. M. Meese, C. Jiang, S. P. Madden, J. D. Caplan, A. P. Burke, R. Virmani, J. Goldstein, and J. E. Muller. Detection of lipid core coronary plaques in autopsy specimens with a novel catheter-based near-infrared spectroscopy system. *Journal of the American College Cardiology*, 1(5):638–48, 2008.

[69] T. J. Romer, J. F. Brennan, M. Fitzmaurice, M. L. Feldstein, G. Deinum, J. L. Myles, J. R. Kramer, R. S. Lees, and M. S. Feld. Histopathology of human coronary atherosclerosis by quantifying its chemical composition with raman spectroscopy. *Circulation*, 97:878–885, 1998.

[70] J. N. Brennan, T. J. Romer, R. S. Lees, A. M. Tercyak, J. R. Kramer, and M. S. Feld. Determination of human coronary artery composition by raman spectroscopy. *Circulation*, 96:99—-105, 1997.

[71] J. T. Motz, M. Hunter, L. H. Galindo, J. A. Gardecki, J. R. Kramer, R. R. Dasari, and M. S. Feld. Optical fiber probe for biomedical raman spectroscopy. *Applied Optics*, 43(3):542—-554, 2004.

[72] D. J. Cuccia, F. Bevilacqua, A. J. Durkin, and B. J. Tromberg. Modulated imaging: quantitative analysis and tomography of turbid media in the spatial-frequency domain. *Optics Letters*, 30(11):1354—-1356, 2005.

[73] S. D. Konecky, A. Mazhar, D. Cuccia, A. J. Durkin, J. C. Schotland, and B. J. Tromberg. Quantitative optical tomography of sub-surface heterogeneities using spatially modulated structured light. *Optics Express*, 17(17):14780—-14790, 2009.

[74] D. J. Cuccia, F. Bevilacqua, A. J. Durkin, F. R. Ayers, and B. J. Tromberg. Quantitation and mapping of tissue optical properties using modulated imaging. *Journal of Biomedical Optics*, 14(2):024012–1—-024012–13, 2009.

[75] S. L. Jacques, and J. C. Ramella-Roman. Polarized light imaging of tissues. *Lasers and Current Optical Techniques in Biology: Comprehensive Series in Photochemistry and Photobiology*, 4(Chapter 19):591—-607, 2004.

[76] S. G. Demos, and R. R. Alfano. Optical polarization imaging. *Applied Optics*, 36(1):150—-155, 1997.

[77] J. F. de Boer, T. E. Milner, M. J. C. van Gemert, and J. S. Nelson. Two-dimensional birefringence imaging in biological tissue by polarization-sensitive optical coherence tomography. *Optics Letters*, 22(12):934—-936, 1997.

[78] K. Sokolov, R. Drezek, K. Gossage, and R. Richards-Kortum. Reflectance spectroscopy with polarized light: is it sensitive to cellular and nuclear morphology. *Optics Express*, 5(13):302—-317, 1999.

[79] B. Yang, J. Lesicko, M. Sharma, M. Hill, M. S. Sacks, and J. W. Tunnell. Collagen fiber orientation mapping with top layer discrimination using polarized light spatial frequency domain imaging (psfdi) on native heart tissue. *Biomedical Optics*, OSA Technical Digest:BM4B.5, 2014.

[80] M. S. Sacks, D. B. Smith, and E. D. Hiester. A small angle light scattering device for planar connective tissue microstructural analysis. *Annals of Biomedical Engineering*, 25:678–589, 1997.

[81] M. S. Sacks, and D. B. Smith. Effects of accelerated testing on porcine bioprosthetic heart valve fiber architecture. *Biomaterials*, 19:1027–1036, 1998.

[82] M. S. Sacks, and D. C. Gloeckner. Quantification of the fiber architecture and biaxial mechanical behavior of porcine intestinal submucosa. *Journal of Biomedical Materials Research*, 46(1):1–10, 1999.

[83] G. C. Engelmayr, V. L. Sales, J. E. Mayer, and M. S. Sacks. Cyclic flexure and laminar flow synergistically accelerate mesenchymal stem cell-mediated engineered tissue formation: implications for engineered heart valve tissues. *Biomaterials*, 27:6083–6095, 2006.

[84] H. Aghamohammadzadeh, R. H. Newton, and K. M. Meek. X-ray scattering used to map the preferred collagen orientation in the human cornea and limbus. *Structure*, 12:249–256, 2004.

[85] O. Kostyuk, and R. A. Brown. Novel spectroscopic technique for in situ monitoring of collagen fibril alignment in gels. *Biophysical Journal*, 87:648–655, 2004.

[86] T. T. Tower, and R. T. Tranquillo. Alignment maps of tissues: I. microscopic elliptical polarimetry. *Biophysical Journal*, 81:2954–2963, 2001.

[87] S. L. Voytik-Hatbin, B. Rajwa, and J. P. Robinson. Three-dimensional imaging of extracellular matrix and extracellular matrix-cell interactions. *Methods in Cell Biology*, 63:593–597, 1998.

[88] A. O. Brightman, B. P. Rajwa, J. E. Sturgis, M. E. McCallister, J. P. Robinson, and S. L. Voytik-Harbin. Time-lapse confocal reflection microscopy of collagen fibrillogenesis and extracellular matrix assembly in vitro. *Biopolymers*, 54(3):222–234, 2000.

[89] P. J. Campagnola, A. C. Millard, M. Terasaki, P. E. Hoppe, C. J. Malone, and W. A. Mohler. Three-dimensional high-resolution second-harmonic generation imaging of endogenous structural proteins in biological tissues. *Biophysical Journal*, 81:493–508, 2002.

[90] K. Konig, and I. Rieman. High-resolution multiphoton tomography of human skin with subcellular spatial resolution and picosecond time resolution. *Journal of Biomedical Optics*, 8(3):432–439, 2003.

[91] W. Goth, B. Yang, J. Lesicko, A. Allen, M. S. Sacks, and J. W. Tunnell. Polarized spatial frequency domain imaging of heart valve fiber structure. *Proceeding of SPIE*, 97:1019–1025, 2016.

[92] A. Kienle, C. Wetzel, A. Bassi, D. Comelli, P. Taroni, and A. Pifferi. Determination of the optical properties of anisotropic biological media using an isotropic diffusion model. *Journal of Biomedical Optics*, 12(1):014026–014035, 2007.

[93] A. A. Leino, A. Pulkkinen, and T. Tarvainen. Valomc: a monte carlo software and matlab toolbox for simulating light transport in biological tissue. *OSA Continuum*, 2(3):957–972, 2019.

[94] S. L. Jacques. Optical properties of biological tissues: a review. *Physics in Medicine and Biology*, 58:R37–R61, 2013.

[95] T. Linder, T. Lofqvist, E. L. G. Wernersson, and P. Gren. Light scattering in fibrous media with different degrees of in-plane fiber alignment. *Optics Express*, 22(14):16829–16840, 2014.

[96] A. Kienle, F. Foschum, and A. Hohmann. Light propagation in structural anisotropic media in the steady-state and time domains. *Physics in Medicine and Biology*, 58:6205–6223, 2013.

[97] E. Simon, P. Krauter, and A. Kienle. Time-resolved measurements of the optical properties of fibrous media using the anisotropic diffusion equation. *Journal of Biomedical Optics*, 19(7):075006, 2014.

[98] C. Donner, and H. W. Jensen. Light diffusion in multi-layered translucent materials. *ACM Transactions on Graphics*, 24(3):1032–1039, 2005.

[99] R. C. Haskell, L. O. Svaasand, T.-T. Tsay, T.-C. Feng, M. S. McAdams, and B. J. Tromberg. Boundary conditions for the diffusion equation in radiative transfer. *Journal of the Optical Society of America*, 11(10):2727–2741, 1994.

[100] C. Zhu, and Q. Liu. Review of monte carlo modeling of light transport in tissues. *Journal of Biomedical Optics*, 18(5):050902, 2013.

[101] B. C. Wilson, and G. Adam. A monte carlo model for the absorption and flux distributions of light in tissue. *Medical Physics*, 10(6):824–830, 1983.

[102] S. T. Flock, M. S. Patterson, B. C. Wilson, and D. R. Wyman. Monte carlo modeling of light propagation in highly scattering tissues-i: model predictions and comparison with diffusion theory. *Transactions on Biomedical Engineering*, 36(12):1162–1168, 1989.

[103] S. L. Jacques, and L. Wang. Monte carlo modeling of light transport in tissues. *Optical-Thermal Response of Laser-Irradiated Tissue*, 4:73–100, 1995.

[104] S. A. Prahl, M. Keijzer, S. L. Jacques, and A. J. Welch. A monte carlo model of light propagation in tissue. *Dosimetry of Laser Radiation in Medicine and Biology*, 5:102–111, 1989.

[105] B. Farina, S. Saponaro, E. Pignoli, S. Tomatis, and R. Marchesini. Monte carlo simulation of light fluence in tissue in a cylindrical diffusing fibre geometry. *Physics in Medicine and Biology*, 44:1–11, 1999.

[106] D. Fukutomi, K. Ishii, and K. Awazu. Determination of the scattering coefficient of biological tissue considering 354 the wavelength and absorption dependence of the anisotropy factor. *Optical Review*, 23:291–298, 2016.

[107] M. C. Robitaille, R. Zareian, C. A. Di Marzio, K. T. Wan, and J. W. Ruberti. Small-angle light scattering to detect strain-directed collagen degradation in native tissue. *Interface Focus*, 1:767–776, 2011.

[108] M. I. Mishchenko. *Electromagnetic scattering by particles and particle groups: an introduction*. Cambridge University Press, 2014.

[109] R. Gaul, D. Nolan, and C. Lally. Collagen fibre characterisation in arterial tissue under load using sals. *Journal of the Mechanical Behavior of Biomedical Materials*, 75:359–368, 2017.

[110] A. Whelan, E. Williams, D. R. Nolan, B. Murphy, P. S. Gunning, D. O'Reilly, and C. Lally. Bovine pericardium of high fibre dispersion has high fatigue life and increased collagen content; potentially an untapped source of heart valve leaflet tissue. *Annals of Biomedical Engineering*, pages 1–11, 2020.

[111] S. A. Self. Focusing of spherical gaussian beams. *Applied Optics*, 22(5):658–661, 1983.

[112] A. F. Fercher. Ophtalmic interferometry. *Optics in Medicine, Biology and Environmental Research*, Ed. G von Bally and S Khanna (Amsterdam Elsevier):221–35, 1990.

[113] G. J. Tearney, M. E. Brezinski, B. E. Bouma, S. A. Boppart, C. Pitris, J. F. Southern, and J. G. Fujimoto. In vivo endoscopic optical biopsy with optical coherence tomography. *Science*, 276(5321):2037–2039, 1997.

[114] E. Real, A. Eguizabal, A. Pontón, M. Calvo Díez, J. F. Val-Bernal, M. Mayorga, J. M. Revuelta, J. M. López-Higuera, and O. M. Conde. Optical coherence tomography assessment of vessel wall degradation in thoracic aortic aneurysms. *Journal of Biomedical Optics*, 18(12):126003, 2013.

[115] T. Xia, D. Liu, A. Dong, G. Wang, H. Zhong, and Y. Wang. Properties of partially coherent elegant laguerre-gaussian beam in free space and oceanic turbulence. *Optik–International Journal for Light and Electron Optics*, 201:163514, 2020.

[116] M. A. Cruz-Gomez, D. Lopez-Aguayo, and S. Lopez-Aguayo. Two-dimensional solitons in laguerre-gaussian potentials. *Journal of Optics*, 22(1):015504, 2019.

[117] N. K. Fontaine, R. Ryf, H. Chen, D. T. Neilson, K. Kim, and J. Carpenter. Laguerre-gaussian mode sorter. *Nature Communications*, 10(1):1–7, 2019.

[118] W. B. Wang, R. Gozali, L. Shi, L. Lindwasser, and R. R. Alfano. Deep transmission of laguerre-gaussian vortex beams through turbid scattering media. *Optics Letters*, 41(9):2069–2072, 2016.

[119] S. Mamani, L. Shi, T. Ahmed, R. Karnik, A. Rodriguez-Contreras, and R. R. Alfano. Transmission of classically entangled beams through mouse brain tissue. *Journal of Biophotonics*, 11(12), 2018.

[120] R. R. Alfano, W. B. Wang, L. Wang, and S. K. Gayen. Light propagation in highly scattering turbid media: concepts, techniques, and biomedical applications. *Photonics: Scientific Foundations, Technology and Applications*, IV(Chapter 9):First Edtion, 2005.

[121] L. Wang. Picosecond kerr gated imaging of phantoms in turbid media. *PhD Thesis*, 1995.

[122] K. Dholakia, N. B. Simpson, and M. J. Padgett. Second-harmonic generation and the orbital angular momentum of light. *Physical Review A*, 54(5):R3745, 1996.

[123] L. Shi, L. A. Sordillo, A. Rodriguez-Contreras, and R. R. Alfano. Transmission in near-infrared optical windows for deep brain imaging. *Journal of Biophotonics*, 9(1–2):38–43, 2016.

[124] C. Z. Sun, and Z. Xiong. Experimental study of tightly focused vortex beams through turbid media. *Acta Optica Sinica*, 34(6), 2014.

[125] A. Yaroshevsky, Z. Glasser, E. Granot, and S. Sternklar. Transition from the ballistic to the diffusive regime in a turbid medium. *Optics Letters*, 36(8):1395–1397, 2011.

[126] J. Ou, J. Yue-Song, S. Yu-Wei, and Q. Xiao-Sheng. Scattering of the laguerre-gaussian beam by a homogeneous spheroid. *Acta Optica Sinica*, 62(11), 2013.

[127] M. A. Cox, L. Maqondo, R. Kara, G. Milione, L. Cheng, and A. Forbes. The resilience of hermite- and laguerre-gaussian modes in turbulence. *Journal of Lightwave Technology*, 37(16):3911–3917, 2019.

[128] H. H. Gilgen, R. P. Novak, R. P. Salathè, W. Hodel, and P. Beaud. Submillimeter optical reflectometry. *Journal of Lightwave Technology*, 7(8):1225–1233, 1989.

[129] S. H. Yun, G. J. Tearney, J. F. de Boer, N. Iftimia, and B. E. Bouma. High-speed optical frequency-domain imaging. *Optics Express*, 11(22):2953–2963, 2003.

[130] E. C. W. Lee, J. F. de Boer, M. Mujat, H. Lim, and S. H. Yun. *In vivo* optical frequency domain imaging of human retina and choroid. *Optics Express*, 14(10):4403–4411, 2006.

[131] K. Yuksel, M. Wuilpart, V. Moeyaert, and P. Mégret. Optical frequency domain reflectometry: A review. *ICTON 2009: 11th International Conference on Transparent Optical Networks*, 2009.

[132] C.-H. Yeh, C.-W. Chow, J.-Y. Sung, P.-C. Wu, W.-T. Whang, and F.-G. Tseng. Measurement of organic chemical refractive indexes using an optical time-domain reflectometer. *Sensors*, 12:481–488, 2012.

[133] W. Drexler, U. Morgner, F. X. Kartner, C. Pitris, S. A. Boppart, X. D. Li, E. P. Ippen, and J. G. Fujimoto. *In vivo* ultrahigh-resolution optical coherence tomography. *Optics Letters*, 24(17):1221–1223, 1999.

[134] C. A. Puliajito, M. R. Hee, C. P. Lin, E. Reichel, J. S. Schuman, J. S. Duker, J. A. Izatt, E. A. Swanson, and J. G. Fujimoto. Imaging of macular diseases with optical coherence tomography. *Ophtalmology*, 102:217–229, 1995.

[135] T. C. Chen, B. Cense, M. C. Pierce, N. Nassif, B. H. Park, S. H. Yun, B. R. White, B. E. Bouma, G. J. Tearney, and J. F. de Boer. Spectral domain optical coherence tomography ultra-high speed, ultra-high resolution ophtalmologic imaging. *Archives of Ophtalmology*, 123:1715–1720, 2005.

[136] S. S. Gao, Y. Jia, M. Zhang, J. P. Su, G. Liu, T. S. Hwang, S. T. Bailey, and D. Huang. Optical coherence tomography angiography. *Investigatives Ophtalmology and Visual Science*, 57(9):OCT27–OCT36, 2016.

[137] S. Jäckle, N. Gladkova, F. Feldchtein, A. Terentieva, B. Brand, G. Gelikonov, V. Gelikonov, A. Sergeev, A. Fritscher-Ravens, J. Freund, U. Seitz, S. Schröder, and N. Soehendra. In vivo endoscopic optical coherence tomography of the human gastrointestinal tract - towards optical biopsy. *Endoscopy*, 32(10):743–749, 2000.

[138] H. Jia, F. Abtahian, A. D. Aguirre, S. Lee, S. Chia, H. Lowe, K. Kato, T. Yonetsu, R. Vergallo, S. Hu, J. Tian, H. Lee, S.-J. Park, Y.-S. Jang, O. C. Raffel, K. Mizuno, S. Uemura, T. Itoh, T. Kakuta, S.-Y. Choi, H. L. Dauerman, A. Prasad, C. Toma, I. McNulty, S. Zhang, B. Yu, V. Fuster, J. Narula, R. Virmani, and I.-K. Jang. In vivo diagnosis of plaque erosion and calcified nodule in patients with acute coronary syndrome by intravascular optical coherence tomography. *Journal of the American College of Cardiology*, 62(19):1748–1758, 2013.

[139] F. J. van der Meer, D. J. Faber, J. Perrèe, G. Pasterkamp, D. B. Sassoon, and T. G. van Leeuwen. Quantitative optical coherence tomography of arterial wall components. *Lasers in Medical Science*, 20:45–51, 2005.

[140] S. Celi, and S. Berti. *In-vivo* segmentation and quantification of coronary lesions by optical coherence tomography images for a lesion type definition and stenosis grading. *Medical Image Analysis*, 18:1157–1168, 2014.

[141] D. Koozekanani, K. Boyer, and C. Roberts. Retinal thickness measurements from optical coherence tomography using a markov boundary model. *IEEE Transaction of Medical Imaging*, 20(9):900–916, 2001.

[142] H. Kawamori, J. Shite, T. Shinke, H. Otake, D. Matumoto, M. Nakagawa, Y. Nagoshi, A. Kozuki, H. Hariki, T. Inoue, T. Ohsue, Y. Taniguchi, R. Nishio, N. Hiranuma, and K. Hirata. Natural consequence of stent malaposition assessed by optical coherence tomography. *Journal of the American College of Cardiology*, 57(14):E1744, 2011.

[143] G. J. Ughi, J. Verjans, A. M. Fard, H. Wang, E. Osborn, T. Hara, A. Mauskapf, F. A. Jaffer, and G. J. Tearney. Dual modality intravascular optical coherence tomography (oct) and near-infrared fluorescence (nirf) imaging: a fully automated algorithm for the distance-calibration of nirf signal intensity for quantitative molecular imaging. *International Journal of Cardiovascular Imaging*, 31:259–268, 2015.

[144] Y. Yasuno, Y. Hong, S. Makita, M. Yamanari, M. Akiba, M. Miura, and T. Yatagai. In vivo high-contrast imaging of deep posterior eye by 1-μm swept source optical coherence tomography and scattering optical coherence angiography. *Optics Express*, 15(10):6121–6139, 2007.

[145] R. Huber, M. Wojtkowski, and J. G. Fujimoto. Fourier domain mode locking (fdml): A new laser operating regime and applications for optical coherence tomography. *Optics Express*, 14(8):3225–3237, 2006.

[146] Y. C. Tong, L. Y. Chan, and H. K. Tsang. Fibre dispersion or pulse spectrum measurement using a sampling oscilloscope. *Electronics Letters*, 33(11):983–985, 1997.

[147] J. Azaña, and M. A. Muriel. Real-time optical spectrum analysis based on the time–space duality in chirped fiber gratings. *IEEE Journal of Quantum Electronics*, 36(5):517–526, 2000.

[148] K. Dolgaleva, A. Malacarne, P. Tannouri, L. A. Fernandes, J. R. Grenier, J. S. Aitchison, J. Azaña, R. Morandotti, P. R. Herman, P. V. S. Marques. Integrated optical temporal fourier transformer based on a chirped bragg grating waveguide. *Optics Letters*, 36(22):4416–4418, 2011.

[149] L. Froehly, and R. Leitgeb. Scan-free optical correlation techniques: history and applications to optical coherence tomography. *Journal of Optics*, 12:084001 (11 pp), 2010.

[150] L. Froehly, S. Iyer, and F. Vanholsbeeck. Dual-fibre stretcher and coma as tools for independent 2nd and 3rd order tunable dispersion compensation in a fibre-based 'scan-free' time domain optical coherence tomography system. *Optics Communications*, 284:4099–4106, 2011.

[151] M. Brezinski. *Optical Coherence Tomography, Principles and Applications*. Elsevier, 2011.

[152] M. Saruwatari. All-optical signal processing for terabit/second optical transmission. *IEEE Journal on Selected Topics in Quantum Electronics*, 6(6):1363–1374, 2000.

[153] A. M. Weiner. *Ultrafast Optics*. Hoboken, NJ, USA, John Wiley & Sons Inc., 2009.

[154] H. J. S. Dorren, M. T. Hill, Y. Liu, N. Calabretta, A. Srivatsa, F. M. Huijskens, H. de Waardt, and G. D. Khoe. Optical packet switching and buffering by using all-optical signal processing methods. *Journal of Lightwave Technology*, 21(1):1–12, 2003.

[155] J. Capmany, B. Ortega, D. Pastor, and S. Sales. Discrete-time optical processing of microwave signals. *Journal of Lightwave Technology*, 23(2):702–723, 2005.

[156] P. Ghelfi, F. Laghezza, F. Scotti, G. Serafino, A. Capria, S. Pinna, D. Onori, C. Porzi, M. Scaffardi, A. Malacarne, V. Vercesi, E. Lazzeri, F. Berizzi, and A. Bogoni. A fully photonics-based coherent radar system. *Nature*, 507:541–545, 2014.

[157] K. Goda, A. Ayazia, D. R. Gossett, J. Sadasivam, C. K. Lonappan, E. Sollier, A. M. Farda, S. C. Hur, J. Adam, C. Murray, C. Wang, N. Brackbill, D. Di Carlo, and B. Jalali. High-throughput single-microparticle imaging flow analyzer. *Proceedings of the National Academy of Sciences of the United States of America*, 109(29):11630–11635, 2012.

[158] D. B. Anderson, J. T. Boyd, M. C. Hamilton, and R. R. August. An integrated-optical approach to the fourier transform. *IEEE Journal of Quantuum Electronics*, 13(4):268–275, 1977.

[159] K. Takada, I. Yokohama, K. Chida, and J. Noda. New measurement system for fault location in optical waveguide devices based on an interferometric technique. *Applied Optics*, 26(9):1603–1606, 1987.

[160] L. Lepetit, G. Chériaux, and M. Joffre. Linear techniques of phase measurement by femtosecond spectral interferometry for applications in spectroscopy. *Journal of Optical Society of America*, 12(12):2467–2474, 1995.

[161] D. K. Gifford, B. J. Soller, M. S. Wolfe, and M. E. Froggatt. Optical vector network analyzer for single-scan measurements of loss, group delay, and polarization mode dispersion. *Applied Optics*, 44(34):7282–7286, 2005.

[162] W. Wieser, B. R. Biedermann, T. Klein, C. M. Eigenwillig, and R. Huber. Multi-megahertz oct: High quality 3d imaging at 20 million a-scans and 4.5 gvoxels per second. *Optics Express*, 18(14):14685–14704, 2010.

[163] Y. Park, T.-J. Ahn, J.-C. Kieffer, and J. Azaña. Optical frequency domain reflectometry based on real-time fourier transformation. *Optics Express*, 15(8):4597–4616, 2007.

[164] M. Siddiqui, and B. J. Vakoc. Optical-domain subsampling for data efficient depth ranging in fourier-domain optical coherence tomography. *Optics Express*, 20(16):17938–17951, 2012.

[165] S. Tozburun, M. Siddiqui, B. J. Vakoc. A rapid, dispersion-based wavelength-stepped and wavelength-swept laser for optical coherence tomography. *Optics Express*, 22(3):3414–3424, 2014.

[166] Y. Park, and J. Azaña. Optical signal processors based on a time-spectrum convolution. *Optics Letters*, 35(6):796–798, 2010.

[167] A. Malacarne, Y. Park, M. Li, S. LaRochelle, and J. Azaña. Real-time fourier transformation of lightwave spectra and application in optical reflectometry. *Optics Express*, 23(25):32516–32527, 2015.

[168] J. Kirkhorn. Introduction to iq-demodulation of rf data. *Trondheim, Norway : Norwegian University of Science and Technology*, 1999.